STUDY OF INNER CORE FINE-SCALE STRUCTURE USING SEISMIC ARRAYS

Felipe Orlando Leyton Flórez, M.S.

Advisor: Keith D. Koper, Ph.D.

An Abstract Presented to the Faculty of the Graduate School of Saint Louis University in Partial Fulfillment of the Requirements for the Degree of Doctor of Philosophy

2006

Abstract

The past 20 years has seen an incredible growth in our knowledge of the composition and structure of the inner core (IC), but its detailed 3D structure has remained elusive, leaving vital constraints of the inner core growth and geodynamo unknown. In the present work, I focus my attention on the region in the IC close to the outer core, using seismic arrays. In the first part, I look for seismic discontinuities suggested to exist within the IC by applying reflection seismology techniques that use precritical $PKiKP$ waveforms as empirical source pulses and perform resolution tests where we compare the data with synthetic waveform stacks. My results show that the inner core lacks a significant (impedance jump $> 3\%$), sharp (thickness $<$ 3-4 km), global discontinuity to depths of 800 km below the inner core boundary. Later, I focus on reports of scattered seismic energy coming from the IC by synthesizing the coda following $PKiKP$ and try to determine the location of the heterogeneities that produce this coda, using previously reported observations as a guide. Using a single-scattering approximation and ray theory, I generate synthetic $PKiKP$ coda envelopes from 6 distinctive places inside the Earth. I find that previously reported "spindle"-shaped or growing coda can only be produced from volumetric heterogeneities located in the shallowest 350 km of the inner core; however, strong trade-offs between the different parameters describing the volumetric heterogeneities preclude the determination of a unique model. Finally, I pursue the characterization of inner core scattering (ICS) by applying a methodology used in the study of scatterers in the crust and upper mantle that consists of curve fitting of the observed scattered energy with a standard model, along with a stripping technique to isolate the $PKiKP$ coda from the rest of the seismic energy. From the observed $PKiKP$ codas I found an average $Q_C \sim 500$ for the IC, reflecting a scattering attenuation at least comparable to the intrinsic attenuation. Also, I found a geographical dependence in the observations of $PKiKP$ coda that can be best explained by a quasi-hemispherical variation in the ICS.

STUDY OF INNER CORE FINE-SCALE STRUCTURE USING SEISMIC ARRAYS

Felipe Orlando Leyton Flórez, M.S.

Advisor: Keith D. Koper, Ph.D.

A Dissertation Presented to the Faculty of the Graduate School of Saint Louis University in Partial Fulfillment of the Requirements for the Degree of Doctor of Philosophy

2006

COMMITTEE IN CHARGE OF CANDIDACY:

Assistant Professor Keith D. Koper,
Chairperson and Advisor

Professor David J. Crossley

Assistant Professor Lupei Zhu

Dedication

"Los sismos son parte de la música de nuestro planeta y entenderlos es mi manera de cuidarlo."

In loving memory of

Robert Edgar Fromm Rhim (1974 - 2004)

Acknowledgments

First, I would like to thank my parents, Patricio and Maricarmen, for their continuous support and encouragement to make my dreams come true. I'm also grateful of my siblings Patricio, Maricarmen, and Fernanda, an incredible source of love and energy. Next, I would like to deeply thank my advisor Dr. Keith D. Koper for his essential support and stimulating discussions that led me to the completion of my research, something that sometimes seemed impossible to me. I would also like to thank Dr. Lupei Zhu, Dr. David J. Crossley, Dr. Robert B. Herrmann, and Dr. Brian J. Mitchell for their teachings, advice, and time invested in my research. I'm deeply thankful to Dr. John Encarnacion and Dr. David Kirschner for not only sharing their knowledge with me, but also a great friendship. I would like to send my gratitude to all the Earth and Atmospheric Sciences' staff and graduate students, for making these years one of the best times in my life. Special mention to past and present students, all very dear friends: Brian, Justin, Mark, Rose, Rachel, Teresa, Sam, Hongyi, Erkan, Boston, Ali, and Kathy, thank you for all your love and support.

Last but not least, I would like to acknowledge Carolina, my wife... words cannot express all what I feel for you and the deepest gratitude for your love, support, encouragement, kindness, caring.

Thank you, very much.

Table of Contents

List of Tables

List of Figures

Chapter 1

Introduction

> "Geologists have turned in despair from the [constitution of the Earth] leaving its center as a playground for mathematicians."
>
> Richard Dixon Oldham (1858 - 1936)

Early in the 1900s, R. D. Oldham recognized the existence of 3 main types of seismic waves: "preliminary tremors" (called primary or P-waves and secondary or S-waves) that travel through the interior of the Earth, and the "large waves", usually restricted to the surface (*Bolt*, 1982). By observing the seismic waves that traveled inside the Earth (the *preliminary tremors*), this pioneer of seismology initiated the study of the deep Earth; indeed, in 1906 he was able to discover the Earth's core (*Oldham*, 1906). Even more, his approach is still used nowadays in the study of the deep Earth (see *Bolt*, 1982). In 1914, Beno Gutenberg estimated the depth of the contact between the core and the mantle (or core mantle boundary, CMB) at 2900 km (2891.1 km according to PREM (*Dziewonski and Anderson*, 1981)). By the mid 1920s, using Earth tides and seismic observations, sir Harold Jeffreys showed that the core had a rigidity much smaller than the mantle suggesting it could even be liquid. Currently, the value of the viscosity of the outer is believed to be close to that of water, but estimations from geodetic and seismic observations span over 14 orders of magnitude (see *Secco*, 1995, for a review).

The discovery of the inner core came 6 years after Tombaugh's discovery of Pluto (the farthest planet in the solar system) when Inge Lehmann, a Danish seismologist, noticed that a particular P-wave arriving in the core shadow zone "can hardly be considered probable that it is due to diffraction" (*Lehmann*, 1936), but rather refracted

at a depth of 5000 km from some discontinuity inside the core. Within 2 years, Beno Gutenberg in the United States and Sir Harold Jeffreys in England had confirmed Lehmann's hypothesis, and only 10 years later, *Bullen* (1946) suggested that the inner core had to be rigid. Direct confirmation using seismic waves has remained elusive (*Julian et al.*, 1972; *Okal and Cansi*, 1998; *Deuss et al.*, 1998, 2000; *Cao and Romanowicz*, 2005); however, the best argument in favor of the rigidity of the inner core comes from the observations of free oscillations of the Earth (e.g *Dziewonski and Gilbert*, 1971).

Cosmochemical arguments favor iron as the major constituent of the core, based on the assumption that there should be relative homogeneity in the solar system, at least in its main elements. Under this assumption, the number of iron atoms should be similar to the number of silicon atoms (*Ganapathy and Anders*, 1976; *Wasson*, 1985); due to the fact that the Earth's mantle is depleted in iron relative to silicon, the core has to be greatly enriched in Fe. Given the much larger volume of the mantle, the core has to be mainly composed of iron in order to maintain the cosmic abundance ratio (*Anderson*, 2003). This conclusion has been greatly supported by mineral physics (e.g. *Birch*, 1964, 1972). Another key factor is that, in order to maintain a long-lived dynamo, a very conductive liquid is necessary in the outer core (e.g. *Merrill et al.*, 1998). Nevertheless, iron by itself cannot satisfy the observed seismic constraints for core, requiring the presence of small percentage of lighter elements (*Birch*, 1964; *Jeanloz*, 1979; *Brown and McQueen*, 1986). The identity and amount of the lighter elements is still uncertain but, considering cosmochemical arguments, *Pourier* (1994) proposed hydrogen, carbon, oxygen, magnesium, silicon, and sulfur, being oxygen and sulfur the most likely (*Steile-Neumann et al.*, 2003). Combining geophysical constraints and chemical arguments, *Alfè et al.* (2000a,b, 2002) found that a ternary or higher mixture of small amounts of S or Si with O is needed.

As the Earth cooled down after the formation of the core, the inner core started to grow through the solidification of iron from the center of the Earth (*Jacobs*, 1953). *Verhoogen* (1961) recognized that the solidification of the core resulted in the release of latent heat, an important source of energy of the geodynamo. Later on, *Braginsky*

(1963) suggested that the partitioning of iron alloy during the solidification of the core also provides a source of compositional buoyancy, contributing between 50% to 80% of the geodynamo's power (*Lister and Buffett*, 1995; *Stacey and Stacey*, 1999).

Our knowledge of the structure inner core lagged behind those on any other region in the Earth because of its remoteness from surface observations and still uncertain properties of the mantle and crust above it. Fortunately, the past 20 years have seen a great increase in our knowledge of the structure of the inner core (for a review, see *Song*, 2003). The observation of fast P-waves traveling parallel to the Earth's rotation axis (*Poupinet et al.*, 1983; *Morelli et al.*, 1986) and the anomalous splitting of core-sensitive eigenmodes (*Woodhouse et al.*, 1986) has led to the discovery of anisotropy inside the inner core (see *Creager*, 2000; *Tromp*, 2001). Differential travel times between PKP_{DF} and PKP_{BC} (*Creager*, 1992; *Song and Helmberger*, 1993) as well as a reanalysis of normal mode data (*Tromp*, 1993) determined that the inner core has a hexagonal pattern of anisotropy (the symmetry axes is sub-parallel to the Earth's rotation axes), with a magnitude of 3%-4% (*Vinnik et al.*, 1994; *Song*, 1996; *McSweeney et al.*, 1997). This observation has been related to lattice preferred orientation of the hexagonal closest packed (hcp) phase of iron (see *Anderson*, 2003, for a review), that has been proposed, based on both experimental and theoretical arguments, to be the most stable phase at core conditions (*Yoo et al.*, 1995; *Vocadlo et al.*, 1999). However, the elastic properties of iron composing the core remain mostly uncertain (*Stixrude and Cohen*, 1995; *Bergman*, 1998; *Mao et al.*, 1998; *Steile-Neumann et al.*, 2003).

There is growing evidence that anisotropy varies with depth below the ICB (*Su and Dziewonski*, 1995; *Ishii et al.*, 2002a,b; *Begheim and Trampert*, 2003); even more, some authors argue the presence of an isotropic layer overlaying an anisotropic bulk inner core (*Shearer*, 1994; *Song and Helmberger*, 1995, 1998; *Creager*, 2000; *Garcia and Souriau*, 2000; *Niu and Wen*, 2001; *Song and Xu*, 2002). The transition from isotropy into anisotropy is not well constrained (*Song*, 2003); in the present work, we make the first attempt to characterize this transition (see Chapter 2, page 7). Other possible causes for seismic boundaries within the inner core could be variations in the

fraction of partial melt (*Singh et al.*, 2000) or a solid-solid phase transition involving iron (*Lin et al.*, 2002). In Chapter 2, we searched for evidence of seismic discontinuities within the inner core with reflection seismology techniques (e.g. *Telford et al.*, 1976) that use precritical $PKiKP$ waveforms as empirical source pulses. Because any phase reflected from an inner core discontinuity will have a small amplitude (due to the strong attenuation inside the inner core (*Doornbos*, 1974; *Qamar and Eisenberg*, 1974; *Cormier*, 1981; *Doornbos*, 1983; *Niazi and Johnson*, 1992; *Bhattacharyya et al.*, 1993; *Li and Cormier*, 2002)), we developed a novel technique combining source and receiver stacks in the search. We performed resolution tests where we compare the data with synthetic waveform stacks created using generalized ray theory (see *Helmberger*, 1983, for a review) and appropriate attenuation operators (*Futterman*, 1962). Our results show that the inner core lacks a significant (impedance jump $>$ 3%), sharp (thickness $<$ 3-4 km), global discontinuity to depths of 800 km below the boundary with the outer core.

Despite its uniform composition, variations inside the inner core have been reported in different scales: from hemispherical differences (*Tanaka and Hamaguchi*, 1997; *Creager*, 1999; *Garcia and Souriau*, 2000; *Wen and Niu*, 2002), passing through scales of hundreds of kilometers (*Creager*, 1997; *Song*, 2000), down to a few kilometers (*Cormier et al.*, 1998; *Vidale and Earle*, 2000; *Koper et al.*, 2004). Indeed, previous studies have reported scattered seismic energy from the inner core (*Vidale and Earle*, 2000; *Vidale et al.*, 2000; *Koper et al.*, 2004; *Poupinet and Kennett*, 2004; *Zhang et al.*, 2005; *Vidale and Earle*, 2005; *Rost et al.*, 2005). Here we examine this issue by focusing on the synthesis of coda following precritical $PKiKP$ and try to determine the location of the heterogeneities that produce this coda, using previously reported observations as a guide (see Chapter 3, page 24). Using a single-scattering approximation and ray theory, we generated synthetic $PKiKP$ coda envelopes from 6 distinctive places inside the Earth: within the lower mantle on the source- and receiver-side, along the core mantle boundary on the source- and receiver-side, along the inner core boundary, and within the inner core. We used 2 approaches to generate synthetic codas from topography on a boundary surface (*Kennett*, 1972; *Doornbos*,

1978; *Haddon and Buchen*, 1981; *Kampfmann and Müller*, 1989), and 1 appropriate for volumetric scattering (*Wu and Aki*, 1985a,b). In our computations we calculated the arrival time, ray parameter, and amplitude of the seismic waves using ray theory (see *Červený*, 2001, for a complete treatment), and considered errors in the back-azimuth, as well as source and receiver effects. We found that previously reported "spindle" shaped or growing coda (*Vidale and Earle*, 2000; *Koper et al.*, 2004) can only be produced from volumetric heterogeneities located in the shallowest 350 km of the inner core; however, strong trade-offs between the different parameters describing the volumetric heterogeneities (i.e. characteristic wavelengths, rms velocity or impedance contrast, and total volume (*Battaille and Flatté*, 1988; *Battaille et al.*, 1990)) preclude the determination of a unique model. Additionally, we found that reasonable models of topography at the core mantle boundary can produce large variations on the $PKiKP$ amplitude due to focusing and defocusing effects. Therefore, complexity at the inner core boundary is not necessarily required to account for dramatic amplitude variations in the direct $PKiKP$ amplitudes (*Koper and Dombrovskaya*, 2005; *Krasnoshcenkov et al.*, 2005).

Finally, in Chapter 4 (page 65) we pursued the characterization of inner core scattering (ICS) using a data set of high frequency $PKiKP$ waveforms recorded at short-period, small-aperture seismic arrays. We applied a methodology used in the study of heterogeneities in the crust and upper mantle, which consists of curve fitting of the observed scattered energy with a standard model (for a review, see *Sato and Fehler*, 1998), along with a stripping technique to isolate the $PKiKP$ coda from the rest (e.g. P, PcP, and PP codas). The assumed model consists of an exponential decay in time, which depends upon the quality factor of coda waves (Q_C), the geometrical spreading of the scattering medium, and a parameter containing general properties of the medium. We found a hemispherical pattern in the observation of $PKiKP$ coda and an average $Q_C \sim 500$ for the inner core. This pattern of observation of $PKiKP$ coda could be related to differences in the vigorousness of convection in the outer core (*Wen and Niu*, 2002; *Yu et al.*, 2005) and solidification process of the inner core (*Bergman*, 1998; *Cormier and Li*, 2002).

Throughout this work, we use short-period, small-aperture, seismic arrays deployed and maintained by the International Monitoring System (IMS), that have successfully been used in similar types of studies (*Koper et al.*, 2003, 2004; *Poupinet and Kennett*, 2004; *Vidale and Earle*, 2005; *Tanaka*, 2005). Arrays consist of numerous seismometers placed in a well-defined configuration (*Husebye and Ruud*, 1989), and were originally built to detect and identify nuclear explosions, lowering the detection threshold of underground nuclear explosions to yields as low as 1 kt (*Douglas et al.*, 1999; *Douglas*, 2002). Using appropriate processing techniques, these seismological instruments allow the study of phases that normally cannot be seen in a seismogram, due to their small amplitude (for a recent review, see *Rost and Thomas*, 2002); they also allow the determination of the direction (or backazimuth) in which the wave front arrives at the stations (e.g. *Aki*, 1957; *Capon*, 1969; *Aki*, 1973; *Ohori et al.*, 2002). These characteristics have helped to resolve fine-scale structures, well below the resolution level of global seismic tomography (e.g. *Doornbos and Husebye*, 1972; *King et al.*, 1974; *Weber et al.*, 1996; *Vidale and Earle*, 2000; *Krüger et al.*, 2001; *Rost and Reveanugh*, 2001; *Rost et al.*, 2005).

This thesis is composed of 3 chapters, each one consisting of a different paper. Hence, the lay out of Chapters 2 to 4 is not the usual, containing each one the normal structure of a paper. At the time of publication of the thesis, Chapter 2 was published in Geophysical Journal International (see *Leyton et al.*, 2005) with the corresponding copyright permission shown in the Appendix; while Chapter 3 and Chapter 4 were in preparation. Before we immerse ourselves into the depths of the inner core, I feel the need to warn you, gracious reader, of the enterprise we are about to begin. From the book *A Journey to the Centre of the Earth*:

> "Now, there were many [scientific reasons] against this terrible journey. The very idea of going down to the center of the Earth was simply absurd. I determined therefore to argue the point after dinner."
>
> Jules Verne (1828 - 1905)

Chapter 2

On the Lack of Seismic Discontinuities Within the Inner Core

† Recent work has suggested that seismic discontinuities might exist within the inner core. Such boundaries could be caused by changes in the strength and orientation of anisotropy, by variations in the fraction of partial melt, or by a solid-solid phase transition involving iron. In this work we search for evidence of inner core discontinuities with reflection seismology techniques that use precritical $PKiKP$ waveforms as empirical source pulses. Because any phase reflected from an inner core discontinuity will have a small amplitude, we develop a novel technique combining source and receiver stacks in the search. We perform resolution tests where we compare the data with synthetic waveform stacks created using generalized ray theory and appropriate attenuation operators. Our results show that the inner core lacks a significant (impedance jump $> 3\%$), sharp (thickness $<$ 3-4 km), global discontinuity to depths of 800 km below the boundary with the outer core.

2.1 Introduction

Several recent studies have suggested the presence of seismic discontinuities within the solid inner core (IC). One scenario, based on the modeling of PKP waveforms at large epicentral distances, suggests a boundary at a radius of 900-1000 km separating an upper isotropic layer from the anisotropic bulk IC (*Shearer*, 1994; *Song and Helmberger*, 1995; *Creager*, 2000; *Niu and Wen*, 2001; *Ouzounis and Creager*, 2001). In this case the discontinuity could be considered as an isotropic velocity jump for

†This article has been published at *Geophys. J. Int., 162*, doi:10.1111/j.1365-146X.2005.02480.x.

seismic waves traveling with nearly polar paths (*Song and Helmberger*, 1998; *Song and Xu*, 2002). A second scenario, based on a combination of PKP travel times and normal mode data, suggests a boundary related to an abrupt change in the orientation of anisotropy in the IC at a radius near 300 km (*Ishii et al.*, 2002b; *Begheim and Trampert*, 2003). For this case we might expect reflections from waves traveling at a variety of angles with respect to Earth's rotation axis, with some waves sensing an apparent velocity increase and others an apparent velocity decrease.

There are also at least three plausible mechanisms for generating a purely isotropic radial discontinuity within the inner core. First, geodynamical modeling of IC growth predicts a thin crust-like region of low partial melt fraction at a depth of about 100 km beneath the inner core boundary (ICB) (*Sumita and Yoshida*, 2003). Second, it is possible that light elements within the IC induce a solid-solid phase change in iron (*Lin et al.*, 2002) which could lead to a seismic discontinuity at a fixed pressure (depth). Third, there is evidence from studies of PKP waves for an abrupt change in attenuation near a radius of 600 km, possibly related to a change in the scale-length of inner core heterogeneities (*Cormier and Li*, 2002).

In this work we search for evidence of inner core discontinuities using methods from reflection seismology (*Telford et al.*, 1976). Our technique is similar to that used in geophysical prospecting except that we use earthquake generated precritical $PKiKP$ waveforms as empirical source pulses. The methodology is basically a migration following the move-out curves of horizontal reflectors located below the ICB. The data have been recorded at the small-aperture array stations of the International Monitoring System (IMS), for which coherence based stacking methods can be used at high frequencies. At precritical distances most of the seismic energy incident upon the ICB is transmitted into the inner core, and the signature of any structure within the IC may best be sought in the $PKiKP$ coda (Figure 2.1). At these distances (with a corresponding ray parameter $\sim 3-9\times10^{-3}[km/s]$) and the properties of the upper IC (radius $\sim$ 1100 km) the reflection coefficient mainly depends on the P wave velocity and the density, in virtually equal amount (*Aki and Richards*, 2002). Hence, there might be an anomaly in P wave velocity balanced by an opposite change in density (as

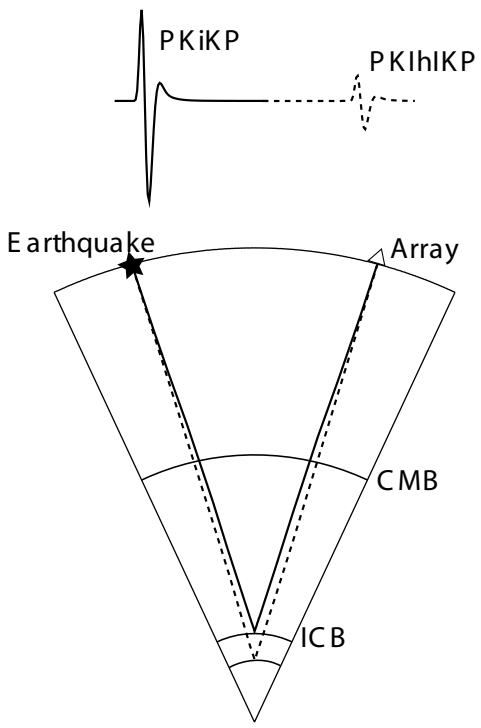

Figure 2.1: Schematic geometry of ray paths used in this study. $PKiKP$ is the direct reflection from the ICB, and $PKIhIKP$ refers to a phase reflected from a hypothetical discontinuity located h km below the ICB.

long as it is the same percentage) and go undetected by our technique, but we think this scenario is unlikely. Due to the expected small amplitude of waves reflected from a discontinuity below the ICB, we combine source and receiver stacks to enhance the post-$PKiKP$ energy. We also generate stacks of ray-based synthetic seismograms to assess the resolution of our procedure, including the effects of uncertainty in the attenuation inside the inner core.

2.2 Data

We selected 124 precritical $PKiKP$ waveforms from a previously developed set of approximately 300 data (*Koper et al.*, 2003; *Koper and Pyle*, 2004). The $PKiKP$ phases were originally identified based on time, slowness, frequency, and polarization characteristics. In this work, we chose the highest quality data requiring a signal to noise ratio of approximately 3:1 in linear receiver stacks. The geographical dis-

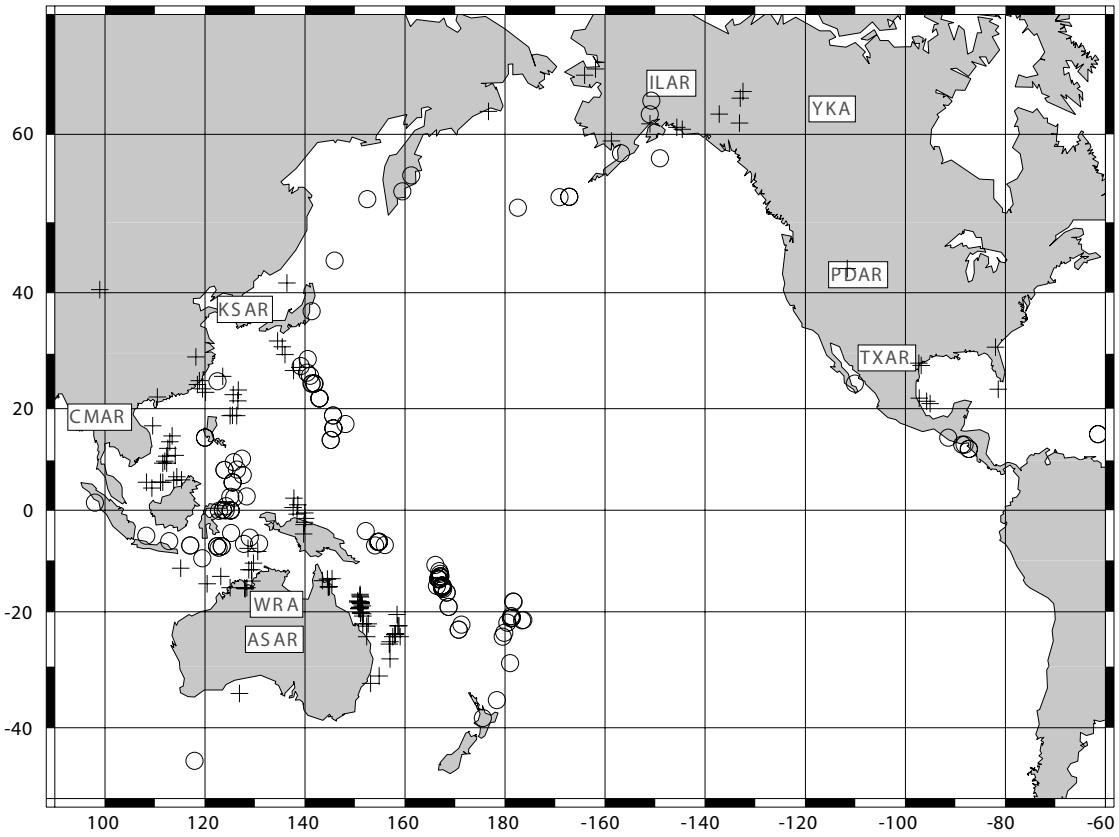

Figure 2.2: Location of IMS arrays and events used in this study. The crosses show the locations of the $PKiKP$ bounce points at the ICB, while the circles show the locations of the epicenters. All 8 of the arrays consist of short-period, vertical-component seismometers. The number of elements in each array varies from 9 to 20, and the array apertures vary from 5 to 25 km. All the earthquakes occurred during the IMS "open" period of 1/1/1995 through 2/20/2000.

tribution of the data is presented in Figure 2.2. Our data mainly sample the ICB between $110° - 160°E$ and $30°N - 30°S$ plus $130° - 180°W$ and $45° - 65°N$. The events were recorded at epicentral distances from 10° to 50° and the majority of the waveforms (67) came from the Australia array stations (ASAR and WRA). Most of the sources were small, deep earthquakes: 87 have depths greater than 50 km and 82 have magnitudes less than $M_w = 6.0$. These factors lead to relatively simple source pulses, helping in the isolation of Earth structure effects. The focal mechanisms of the events show a slight preference for steeply plunging P or T axes, which aids in the excitation of $PKiKP$.

2.3 Methodology

For each source-receiver combination we visually inspected the data and eliminated obviously bad traces. Next, we filtered each trace using a 2-pole Butterworth filter with corner frequencies of 1.0 Hz and 5.0 Hz. We then selected a time window of about 3 s that bracketed the $PKiKP$ arrival on all of the array elements, re-sampled the traces to a time interval of 0.01 s with linear interpolation, and realigned them using cross-correlation. Finally, we did a simple linear sum to create a receiver stack, because this method introduces the least amount of waveform distortion.

We used two procedures to reduce unwanted source effects in the receiver stack. In the first procedure we formed the envelope function, removing the zero crossings that could lead to destructive interference in the source stacks. In the second procedure, we used the array averaged $PKiKP$ waveform as an empirical source function and deconvolved it from the receiver stack. This was done using an iterative technique in the time domain (*Ligorria and Ammon*, 1999), with a Gaussian filter which preserved the frequency band previously selected. Note that this method will preserve the polarity of secondary phases, while the other will not.

An example of these methodologies is presented in Figure 2.3. In this case a depth phase ($pPKiKP$) with a reversed polarity can clearly be seen arriving at 17 s after the $PKiKP$. Even though $pPKiKP$ has a different slowness than $PKiKP$, it sums coherently in the receiver stack because the differential slowness is low and the array aperture is small. For the same reason, we can expect reflections coming from discontinuities within the inner core to interfere constructively in the receiver stacks without the use of intra-array move-out corrections.

The resulting signal-to-noise ratio in the receiver stacks was too small to constrain reasonable models of inner core structure. We decided to further increase this ratio by stacking the receiver stacks to create source stacks. For this purpose, we divided our data set into bins depending on the theoretical $PKiKP$ ray parameter of each event. In each bin we assigned the average ray parameter to all the traces included. Afterward, we calculated the move-out for each bin by computing the time difference

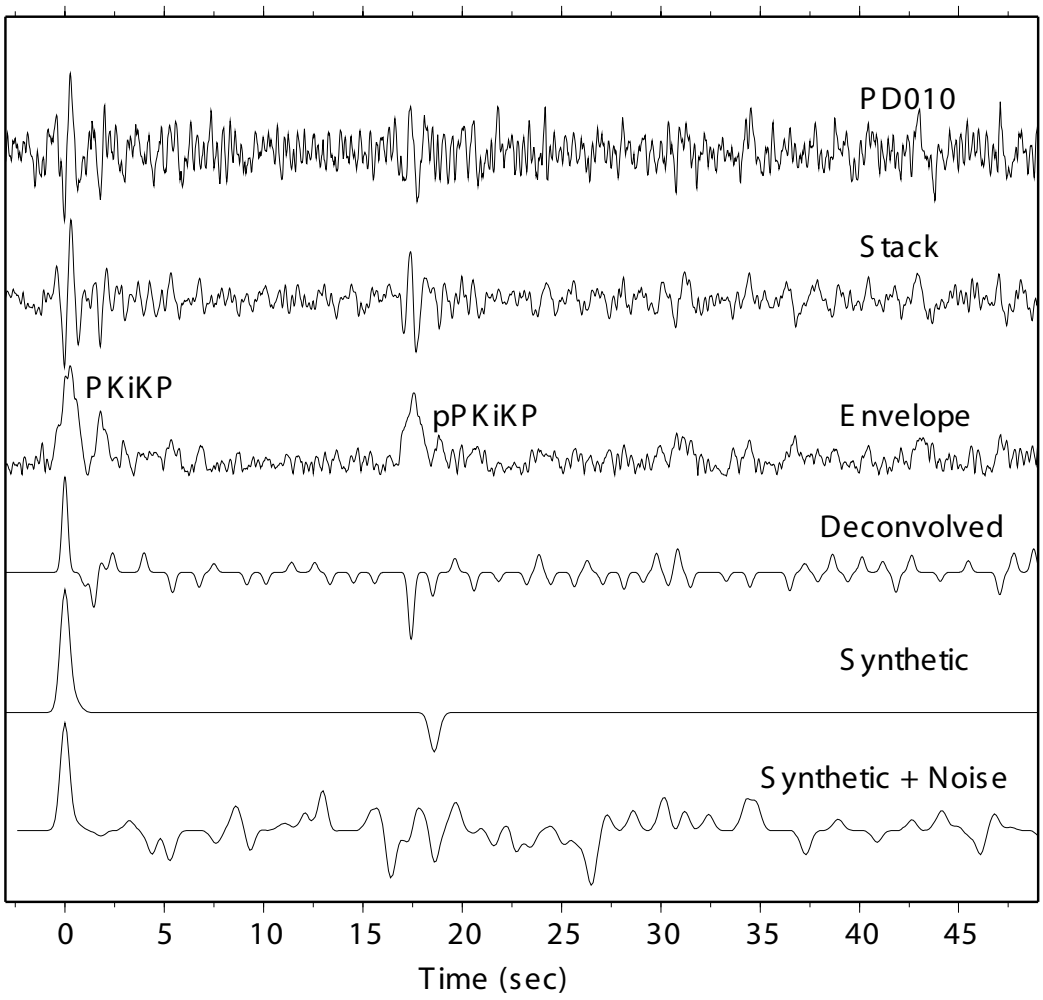

Figure 2.3: Data recorded at Pinedale, Wyoming (PDAR) from a 4.5 m_b event that occurred at 1998/06/21 08:03:57.0, with an epicenter of 13.1 N, 88.1 W. The source depth is 67 km and the source-receiver distance is 34°. The waveforms, from top to bottom, are: a single trace from the PDAR array, receiver stack using all the PDAR traces, envelope of the receiver stack, the deconvolved receiver stack, synthetic receiver stack for that event, and synthetic with random, Gaussian noise. Note the clear arrival after the $PKiKP$ phase at 17 s, which corresponds to $pPKiKP$. The polarity of this phase is lost in the envelope but is retained in the deconvolved trace.

between $PKiKP$ and a later phase ($PKIhIKP$) reflected from a hypothetical discontinuity located h km below the ICB. At the corresponding move-out, we computed the mean value of the receiver stack for a time window of 1 s (in case we missed the exact arrival time, we still have the possibility of getting energy from the later phase). We tried several different time windows for the averaging (from 0.5 to 2.0 s) and retained the one that reflected the frequency content of the receiver stacks. Finally, we averaged over all the traces (creating the source stack) and computed the standard deviation. This process was repeated for discontinuity depths ranging from the ICB to 1150 km beneath, using 5 km increments which corresponds to almost 1 s in time (see Figure 2.4). In general, the energy from any depth phase is reduced because they do not add coherently for the $PKIhIKP$ move-out. This follows from the wide variety of distances and depths among the sources.

2.4 Results

We considered several different inner core models for generating the source stacks, varying the depth of the hypothetical discontinuity from the ICB to 1150 km below in increments of 5 km. The stacks for the deconvolved traces are shown in Figure 2.4, while the stacks for the envelopes are shown in Figure 2.5. We used a conservative measure to assess the likelihood of a $PKIhIKP$ arrival: the stacked energy should be, at least, one time-averaged standard deviation over the zero level. In no case did we find significant energy present at the time appropriate for the candidate $PKIhIKP$ arrival for any case. This was true for source stacks created with both types of modified receiver stacks. We also tried different geographical subsets of source stacks to test for the possibility of a regional discontinuity within the inner core. We combined WRA with ASAR, ILAR with YKA, KSAR with CMAR, and PDAR with TXAR (Figure 2.6). No evidence for a $PKIhIKP$ arrival was found in any of the subsets. Finally we repeated the search using slightly different frequency bands, including lower frequencies, but we obtained the same results.

To quantify the resolving power of our method we performed the same source

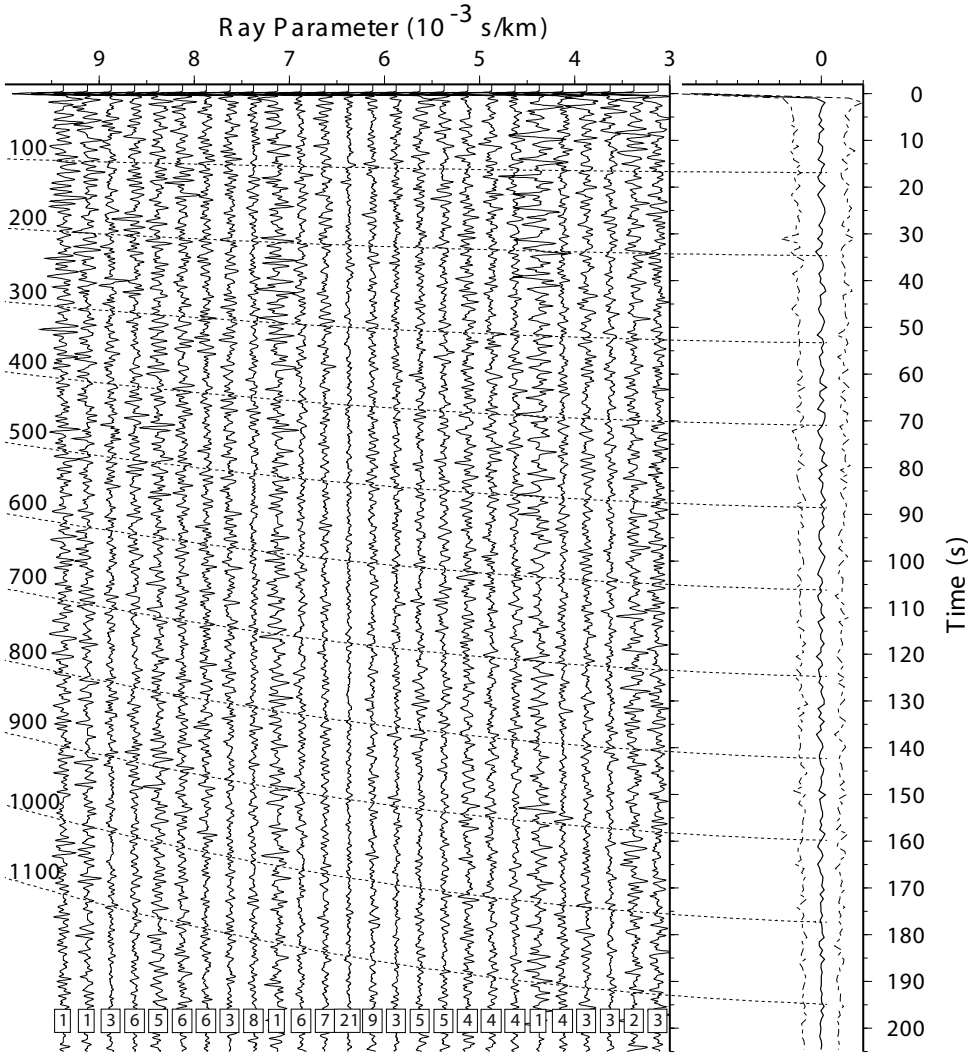

Figure 2.4: All deconvolved waveforms stacked into ray parameter bins. The number of events included in each bin is shown at the bottom, while the dashed lines indicate the move-out for a theoretical discontinuity at the depth below the ICB indicated at the left. In the figure at the right, it is shown the stack and the dashed traces represents the mean plus and minus one standard deviation.

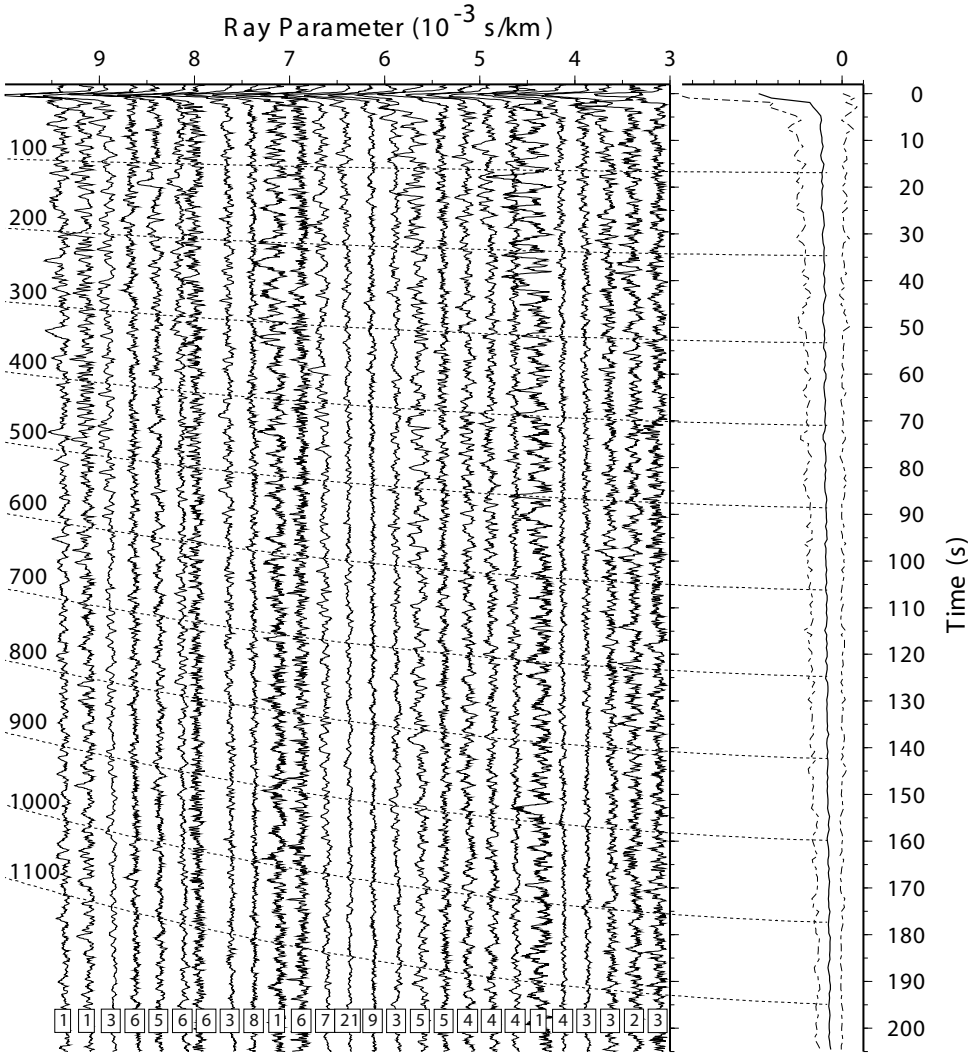

Figure 2.5: Envelopes of all waveforms arranged into ray parameter bins. The number of events included in each bin is shown at the bottom, while the dashed lines indicate the move-out for a theoretical discontinuity at the depth below the ICB indicated at the left. On the right is shown the final stack, with the dashed traces representing the mean plus and minus one standard deviation.

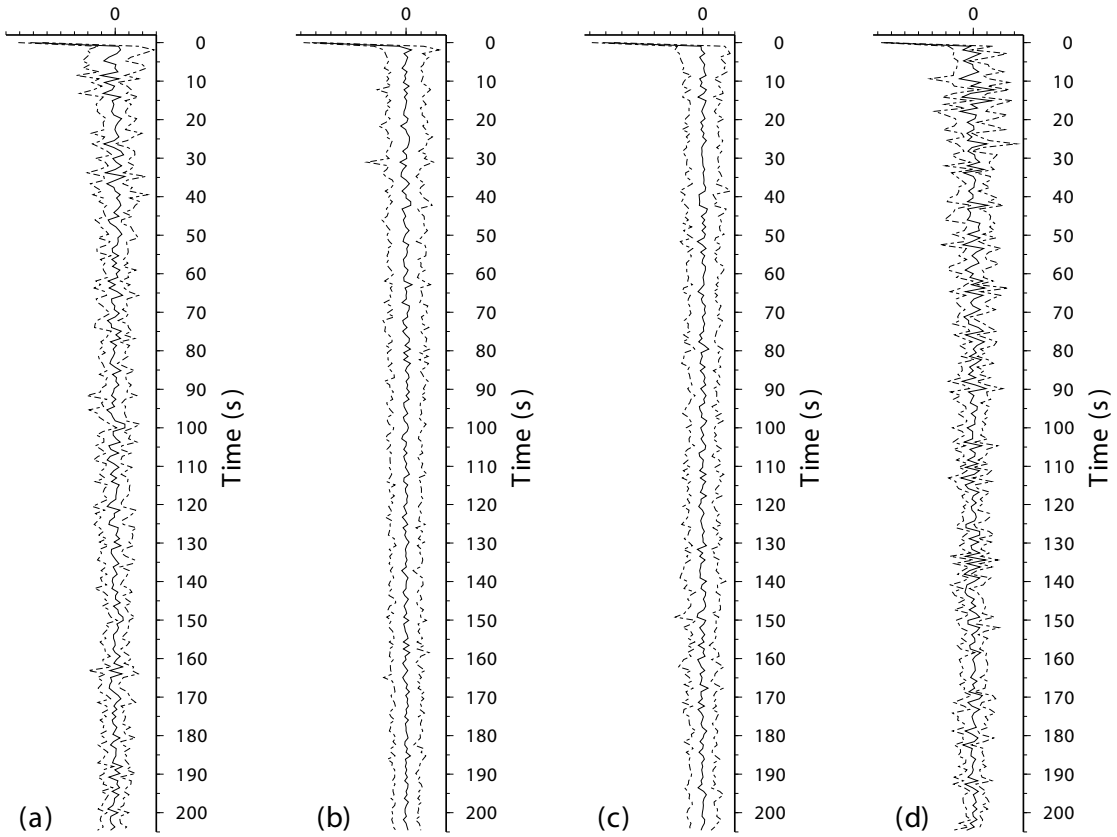

Figure 2.6: Geographical subsets of stacked deconvolved receiver stacks: (a) stations ILAR and YKA (12 events), (b) stations WRA and ASAR (67 events), (c) stations KSAR and CMAR (38 events), and (d) stations PDAR and TXAR (7 events). In all of them, the dashed traces represent the stack (mean) plus and minus one standard deviation.

stacking procedure on synthetic seismograms. We computed the synthetic receiver stacks for modified PREM models (*Dziewonski and Anderson*, 1981), using the generalized ray method (*Helmberger*, 1983) plus the source mechanism information published in the Harvard CMT catalog, and applied attenuation with appropriate time domain operators (*Futterman*, 1962). We also added random, Gaussian noise with the average signal to noise ratio presented in the receiver stacks (3:1) (Figure 2.3). Examples of synthetic source stacks are presented in Figures 2.7 for all the data and in Figure 2.8 for only the polar data. We systematically varied the impedance contrast of the hypothetical discontinuity, as well as Q in the inner core, to determine the maximum discontinuity depth that could generate an observable $PKIhIKP$ signal. Our Q_P values ranged from 450, taken from PREM (*Dziewonski and Anderson*, 1981), down to 225 similar to those reported in other studies (*Song and Helmberger*, 1995; *Li and Cormier*, 2002; *Niu and Wen*, 2001).

A summary of resolvable depths for a global discontinuity, and a discontinuity sensed only by polar data, is presented in Table 2.1. In this study we define as *polar* those ray paths making angles smaller than 35° with respect to the Earth's rotation axis. We considered the discontinuity to be resolvable if the amplitude of the stacked $PKIhIKP$ energy was outside of one time-averaged standard deviation from the zero level. Note that the maximum resolvable depth depends not only on the inner core model, but also on the number of events included in each stack. Therefore, a global discontinuity can be ruled out to a greater depth than regional discontinuities.

Our data were recorded by short-period instruments, therefore they are sensitive to reflections from seismic "discontinuities" with thicknesses less than 3 km. It is possible that more gradual variations might go undetected in the present study, but be visible at lower frequencies in other studies. We performed some computations to quantify the effect of a smooth transition (*Brekhovskikh*, 1960) instead of a sharp discontinuity. Using appropriate reflection coefficients (*Richards*, 1972) we find that any transition wider than 4 km will go undetected in our short-period data. It is also possible that reflections from layers close to the ICB may not be well separated from the main $PKiKP$ phase, and so could be missed by our analysis, even if the layer

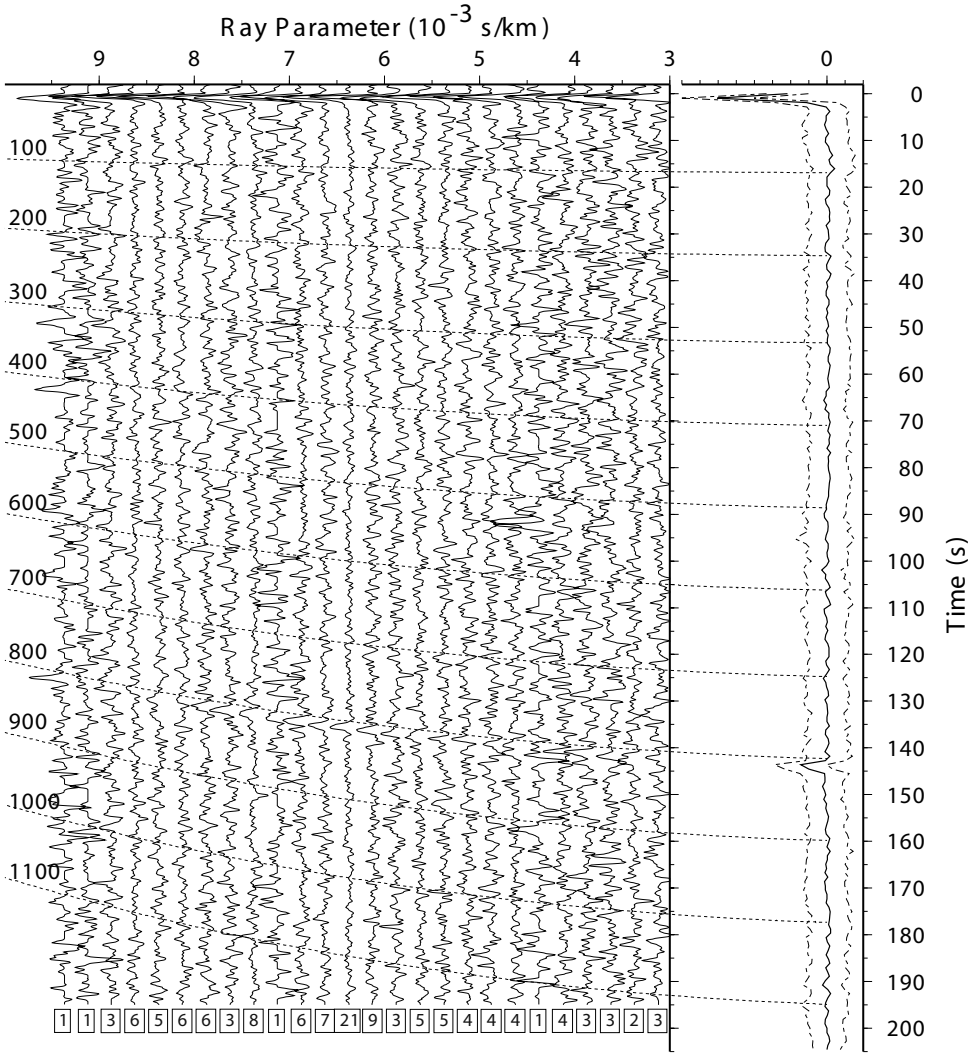

Figure 2.7: Synthetic waveforms with artificial noise for all data, arranged into ray parameter bins. The number of events included in each bin is shown at the bottom, while the dashed lines indicate the move-out for a theoretical discontinuity at the depth below the ICB indicated at the left. Synthetic waveforms were computed for the PREM model modified by an impedance contrast of 3% located at 800 km below the ICB. In the figure at the right, we show the stack (solid line) and the mean plus and minus one standard deviation (dashed lines). This is an example of the smallest signal resolvable at this depth, using our criterion of plus or minus one time-averaged standard deviation.

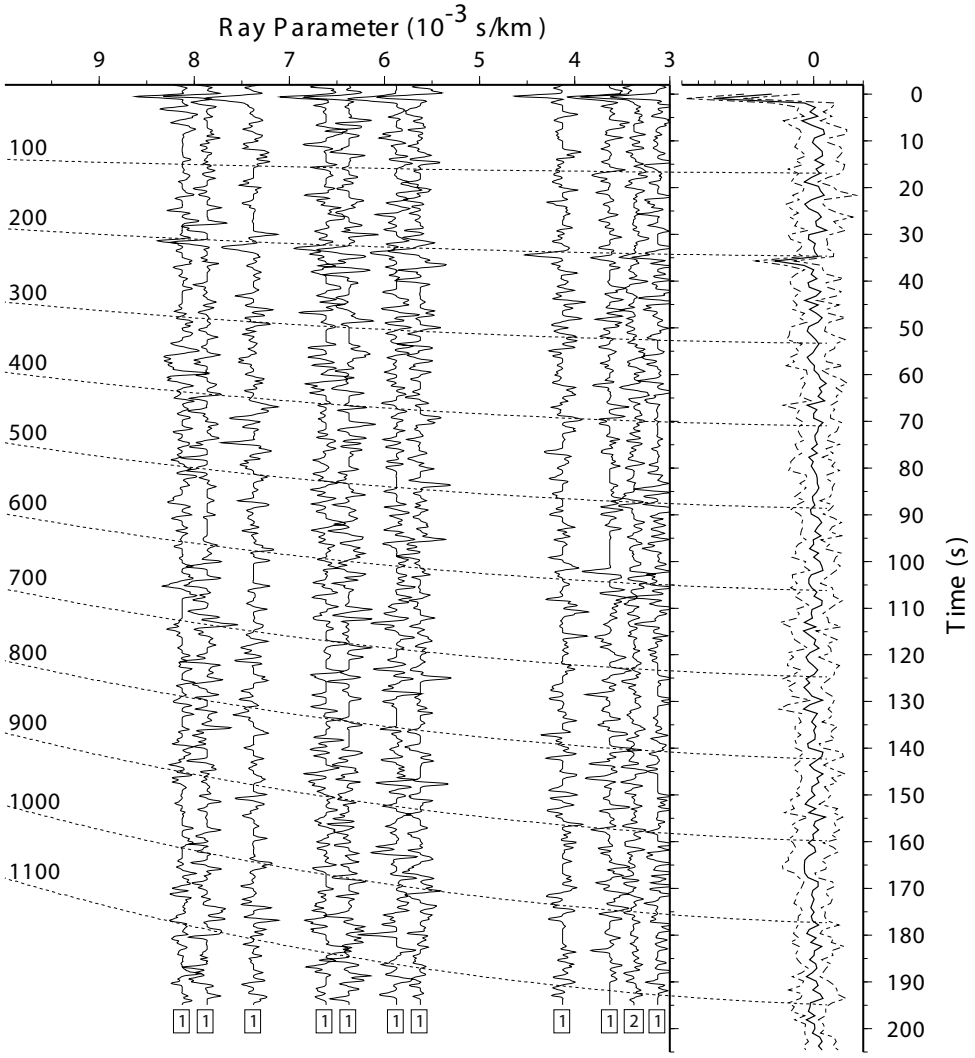

Figure 2.8: Synthetic waveforms (with artificial noise) for polar data, arranged into ray parameter bins. The number of events included in each bin is shown at the bottom, while the dashed lines indicate the move-out for a theoretical discontinuity at the depth below the ICB indicated at the left. Synthetic waveforms were computed for the PREM model modified by an impedance contrast of 2% located at 200 km below the ICB. On the right, we present the final stack in solid line and the mean plus and minus one standard deviation in dashed lines.

Table 2.1: Maximum depth resolvable for hypothetical inner core discontinuity

Data Set[a]	Number of Data	Impedance Jump	Q Relative to PREM	Maximum Depth[b], km
ALL	124	5%	100%	950
ALL	124	3%	100%	800
ALL	124	2%	100%	700
ALL	124	1%	100%	650
ALL	124	5%	50%	900
ALL	124	3%	50%	750
ALL	124	2%	50%	650
ALL	124	1%	50%	400
Polar	12	5%	100%	800
Polar	12	3%	100%	750
Polar	12	2%	100%	700
Polar	12	1%	100%	600
Polar	12	5%	50%	650
Polar	12	3%	50%	550
Polar	12	2%	50%	500
Polar	12	1%	50%	400

[a] Polar data includes sources recorded at ILAR and YKA only.
[b] Refers to depth below the ICB.

is quite sharp. We carried out tests on this issue and found that anything shallower than 50 km beneath the ICB might be missed in the current study.

2.5 Discussion

In the search conducted here, no coherent energy was found in the $PKiKP$ coda. Therefore, it seems probable that the high frequency scattered energy reported as coming from the inner core (e.g.. *Vidale and Earle* (2000) or *Koper et al.* (2004)) does not come from a preferred depth. This result can help us constraint proposed models for the structure in the deep interior of the Earth.

As mentioned earlier, *Sumita and Yoshida* (2003) proposed the presence of a crust-like region, followed by a low velocity zone, due to the changes in the partial melt fraction, process associated to the viscous compaction of a solid matrix. Our results

excludes the possibility of a sharp (less than 4 km) transition between the layers with different partial melt. This could be related to the viscosity in the IC and/or density change between the inner and outer core which strongly influence this phenomena (*Sumita et al.*, 1996).

Lin et al. (2002) speculate about the possibility of a phase transition inside the IC, probably associated to a fixed depth (fixed pressure). They argue that the bcc phase could be stable at inner core conditions if the percentage of lighter elements (e.g.. Si, S, or O) is larger than 5%. They also suggest the possibility of a mixture of Si-rich bcc phase and a Si-poor hcp phase in the IC. In either case, there should be a transition from bcc phase into bcc+hcp and/or bcc+hcp into hcp, in which the percentage of hcp will determine the level of anisotropy. According to our findings, the percentage of bcc should gradually decrease with pressure (depth) leaving only the anisotropic hcp phase for smaller radius.

Explaining the observed change in anisotropy, *Cormier and Li* (2002) envisioned a change in the scale length of heterogeneities in the inner core, going from few kilometers to tens of km. In case of having elongated structures, with their longest dimension aligned in a specific direction(forming a stratigraphic feature), this change would represent a sharp boundary. Our results exclude this possibility indicating either a random orientation or a more gradual transition.

Singh et al. (2000) proposed the presence of liquid in the inner core as a possible explanation of the seismic observations. In their model, they considered elongated inclusions aligned with the polar axis, which should be detectable by our polar data. The authors suggest that these inclusions would be restricted to the upper few kilometers of the IC. The transition from partially melt inner core to a pure solid, according to our results, would have to be broader than 5 km.

A special remark should be made with respect to the proposed transition from isotropy to anisotropy (*Shearer*, 1994; *Song and Helmberger*, 1995; *Creager*, 2000; *Niu and Wen*, 2001; *Ouzounis and Creager*, 2001) due to the large interest in the community. Considering the anisotropy models proposed by *Creager* (1999) and *Ishii et al.* (2002b), we computed the apparent P wave velocity increase sensed by our polar

data obtaining 1.21 and 1.96%, respectively. Even though this value is very small, is still within the range considered in our study, giving a depth of 600 km below the ICB in which we are able to resolve. Our findings confirm the previously speculated presence of a broader transition between isotropy and anisotropy (*Ouzounis and Creager*, 2001). Note that the maximum resolvable radius ($\sim$ 600 km) is not small enough to let us resolve the proposed change in anisotropy in the innermost inner core (*Ishii et al.*, 2002b).

2.6 Conclusions

Stacks of precritical $PKiKP$ waveforms show no evidence for a coherent later arriving phase created by a discontinuity within the inner core. Because of low Q in the inner core the resolving power of the data decreases with depth; however, based on tests involving synthetic waveforms, we can rule out the existence of a global discontinuity to a radius of 400 km. The negative results are less restrictive on the existence of regional discontinuities because fewer data are included in the regional substacks. For instance, only 12 data have the polar paths required to sense a discontinuity related to an isotropy/anisotropy boundary in the upper inner core. Nevertheless, in all the geographical regions sampled by our data we can rule out a significant discontinuity down to a radius of about 750 km.

Tentative evidence for a sharp seismic discontinuity within the inner core has previously been presented based on post-$PKiKP$ energy recorded at one of the array stations used in this study (*Souriau and Souriau*, 1989). However, a systematic search combining data from several events was not carried out, and we feel it is more likely that the observed energy was created by scattering from small wavelength heterogeneities within the inner core. Evidence for such structures has recently been presented based on the observation of unusually large and long $PKiKP$ coda (*Vidale and Earle*, 2000), and we have made similar observations ourselves (*Koper et al.*, 2004). We emphasize that the results presented here are not inconsistent with such observations, but rather are inconsistent with the idea of simple radial discontinuity,

such as the ICB itself, existing within the inner core.

Chapter 3

Using $PKiKP$ Coda to Determine Inner Core Structure. 1. Synthesis of Coda Envelope Using Single-Scattering Theories

Previous seismic studies have reported evidence of scattered seismic energy coming from the inner core (IC). This implies that the IC has lateral variations in structure or composition with a scale length of tens of kilometers. In the present study, we focus on synthesizing the coda following precritical $PKiKP$ and try to determine the location of the heterogeneities that produce this coda, using previously reported observations as a guide. Using a single-scattering approximation and ray theory, we generate synthetic $PKiKP$ coda envelopes from 6 distinctive places inside the Earth: within the lower mantle on the source- and receiver-side, along the core mantle boundary on the source- and receiver-side, along the inner core boundary, and within the inner core. We use two approaches to generate synthetic coda from topography on a boundary surface, and one that is appropriate for volumetric scattering. In our computations we calculate the arrival time, ray parameter, and amplitude of the seismic waves, and take into account errors in the backazimuth, as well as source and receiver effects. We find that the previously reported "spindle" shaped or growing coda can only be produced from volumetric heterogeneities located in the shallowest 350 km of the IC; however, strong trade-offs between the different parameters describing the volumetric heterogeneities (i.e. characteristic wavelengths, rms velocity or impedance contrast, and total volume) preclude the determination of a unique model. Additionally, we find that reasonable models of topography at the core mantle boundary can produce large variations of the $PKiKP$ amplitude due to focusing and defocusing effects. Therefore, complexity at the inner core boundary is not necessarily required to account for

dramatic amplitude variations in the direct $PKiKP$ amplitudes.

3.1 Introduction

Seismic wave travel-time tomography has been very successful at imaging lateral variations from an initial layered Earth model, mostly for P and S waves velocities (e.g. *Romanowicz*, 2003); however, its success is limited by the requirement that the scale-length of the heterogeneity must be much larger than the wavelength of the relevant seismic waves. In global mantle models, this leads to resolution of no better than hundreds of kilometers, even in the best sampled regions. To examine smaller scale heterogeneities in the Earth it is necessary to use scattered seismic energy, as found for example in the extended codas of seismic waves. Since the early work of *Aki* (1969), several authors have devoted their work to the characterization of coda, primarily to deduce the properties of crustal heterogeneities located near a seismograph station (e.g. *Aki*, 1973; *Berteussen et al.*, 1975; *Bannister et al.*, 1990; *Revenaugh*, 1995; *Nishigami*, 1997; *Snieder et al.*, 2002). A smaller number of studies have been focused on the characterization of coda created in the deep interior of the Earth, and these include studies of ScS and SKS coda (*Lee et al.*, 2003; *Rondenay and Fischer*, 2003), PKP coda (*Hedlin and Shearer*, 2002; *Vidale and Earle*, 2005; *Zhang et al.*, 2005), P_{diff} coda (*Earle and Shearer*, 2001), and $PKiKP$ coda (*Vidale and Earle*, 2000; *Vidale et al.*, 2000; *Koper et al.*, 2004; *Poupinet and Kennett*, 2004).

Many coda studies have relied on arrays of seismometers; indeed, the use of seismic arrays has proven to be crucial in the determination of the location of fine-scale heterogeneities well below the resolution level of global seismology (*Rost and Thomas*, 2002). Key advantages to using arrays include the improvement made in the signal to noise ratio and the determination of the direction in which the waves arrive at the stations. These features were successfully exploited in the interpretation of PKP precursors as P waves scattered at the core-mantle boundary (*Cleary and Haddon*, 1972; *Haddon and Cleary*, 1974; *Battaille and Flatté*, 1988), the definition of peculiar scattering regions in the lower mantle (*Kaneshima and Helffrich*, 1998; *Rondenay and*

Fischer, 2003; *Braña and Helffrich*, 2004), and the search for the root of the Hawaiian plume near the CMB in the early work of *Kanasewich et al.* (1973) (for a review, see *Weber et al.*, 1996). Other examples include the work of *Doornbos and Vlaar* (1973) that used data from NORSAR in their interpretation of PKP precursors, and *King et al.* (1974) who used WRA data to emphasize the idea that useful observations of precursors can best be made using seismic arrays.

Arrays have also been important in detecting the subtle coda waves of precritical reflections ($PKiKP$) from the inner core boundary (ICB) (e.g. *Vidale and Earle*, 2000; *Koper et al.*, 2004). The observations are characterized by high frequency, low slowness energy that lasts for up to 200 s after the direct arrival. For distances of about $50^\circ - 70^\circ$ many of the codas are emergent and initially grow with time, resulting in a spindle-shaped envelope function. At these distances the reflection coefficient at the ICB is quite small and the parent $PKiKP$ phase is often too small to be observed; therefore any ray having a slowness similar to that of $PKiKP$ (such as the ones generated after scattering on the source-side) will tend to have a small amplitude, thus limiting the possibility of being observed after traveling long distances. This has been taken to imply that the coda waves are created by heterogeneity deep within the Earth, and two basic models have been proposed for that heterogeneity: complexity at the inner core boundary or ICBS (*Poupinet and Kennett*, 2004), and heterogeneities inside the inner core, or ICS (*Vidale and Earle*, 2000; *Vidale et al.*, 2000; *Koper et al.*, 2004). *Poupinet and Kennett* (2004) suggested that a reverberative process as responsible for ICBS, while *Vidale and Earle* (2000) proposed that volumetric heterogeneities inside the inner core would produce ICS. Both could be caused by variations in the orientation of anisotropy, or the presence of pockets of partial melt, perhaps due to softening that occurs at homologous temperatures (just below the melting point) or the presence of impurities that modify the melting point.

However, there is still a debate on the origin of the $PKiKP$ coda waves, in particular whether the lower mantle, the core mantle boundary (both in source and receiver side), the inner core boundary, or the inner core can produce the characteristics in the $PKiKP$ coda. In general, the coda of any seismic wave is formed by the combined

scattering that occur throughout its entire path. The observed $PKiKP$ coda waves arrive almost vertically (*Vidale and Earle*, 2000; *Koper et al.*, 2004), so the contribution of scattering in the crust and upper mantle from the receiver-side should be very small. Indeed, if most of the energy comes from scattering in the receiver-side at the crust and upper mantle, the anomalies in slowness will be too large at the appropriate time-lags ($\sim$ 100 s) and should produce large anomalies in backazimuth, which are not observed in the data. Furthermore, if the observed $PKiKP$ coda is the product of near-receiver scattering with steep angles (from multiple reverberations in the crust), the shape of the coda for the other phases with similar slownesses (PcP and ScP) should present the same decay rate as does the $PKiKP$, but this also is not seen in the data (*Koper et al.*, 2004). The same argument can be used to eliminate the possibility of the coda being generated by reverberations on the source-side. The most plausible place to generate $PKiKP$ coda, outside of the inner core, is the lowermost mantle. In this region, there have been clear observations of small-scale heterogeneities that produce precursors to $PKP + PKKP$ phases. One particularly interesting aspect of this type of scattering is that PKP precursor energy grows with time (*Hedlin et al.*, 1997; *Shearer et al.*, 1998; *Hedlin and Shearer*, 2002) in the same way that $PKiKP$ codas increase at the distance range between $50^\circ - 70^\circ$ (*Vidale and Earle*, 2000; *Koper et al.*, 2004).

In the present work, we construct synthetic envelopes of $PKiKP$ coda waves in order to quantify and compare the effects of the various types of scattering. We consider four potential sources for precritical $PKiKP$ coda waves: (1) volumetric heterogeneity in the lowermost mantle, (2) topography on the CMB, (3) topography on the ICB, and (4) volumetric heterogeneity within the inner core. Mainly, we propagate plane waves from the source to the deep Earth, let them interact with the heterogeneous region (through the use of an "equivalent" reflection coefficient), and then propagate them back to the surface. Because of the many trade-offs relating to the absolute amplitude of the coda waves, we focus mainly on the shape and decay rate of the synthetic codas to discriminate among the four hypothetical types of scattering.

3.2 Synthesis of *PKiKP* Coda Envelopes

3.2.1 Preliminary Considerations

Throughout this paper we focus on the effect of single scattering, i.e. a seismic wave interacts with one and only one heterogeneity before reaching the receiver. This assumption is valid in cases of topographical scattering with low amplitude-to-wavelength ratio topography (*Doornbos*, 1988; *Kampfmann and Müller*, 1989), and for volumetric scattering from heterogeneities with velocity contrast smaller than a few percent in rms (*Margerin and Nolet*, 2003a). This assumption has often been made in studies of deep Earth heterogeneity, with the notable exceptions of *Margerin and Nolet* (2003a,b) who developed a radiative transfer theory, *Shearer and Earle* (2005) who developed a stochastic particle based approach, and *Wen and Helmberger* (1998a,b) who coupled finite-difference simulations with generalized ray synthetics.

In generating coda waves we consider potential point scatterers in a region (either a surface or a volume), propagate a pre-scattering plane wave from the source to each scatterer, and then propagate a post-scattering plane wave from the scatterer to the receiver. We use seismic ray theory (*Červený*, 2001) to compute the travel time, amplitude, and slowness of the plane waves for spherically symmetric Earth models. Generally, the ray parameter of the pre- and post-scattering ray segments differ, being determined by the relative location of the scattering point with respect to the source and receiver. The numerical integration is done by sampling the spherical Earth model and considering the medium properties (P-velocity, density, and Q) constant in each layer, using a thickness of 0.1 km that represents the integration step in a linear summation scheme. The change in amplitude due to the scattering is given by an "equivalent" reflection coefficient, obtained by considering the nature of the scattering, and is discussed in the following sections. Finally, we project the displacement of the resulting up-going wave into the vertical, adding the surface effect.

Examples of synthetic $PKiKP$ envelopes are shown in Figure 3.1 for the epicentral distances of 60° (left) and 80° (right), under the assumption of isotropic surface scattering at the core mantle boundary; in other words, assuming there is no change

in amplitude during the scattering process, similar to the methodology described by *Scott and Helmberger* (1983), later modified for a point source by *Kampfmann and Müller* (1989), and used by *Battaille and Flatté* (1988) to generate PKP precursors from topography at the CMB. All values presented here (arrival time, amplitude, and slowness) are shown relative to the corresponding values of the direct $PKiKP$ wave. Colors represent different branches of scattered waves: green for $P.KP_{CD}$, red for $P.KP_{BC}$, and blue for $P.KP_{DF}$. Note that for epicentral distances larger than 45°, we have 2 branches for $P.KP_{CD}$: a prograde branch arriving with a ray parameter higher than $PKiKP$, and a retrograde branch arriving with a ray parameter smaller than $PKiKP$. The way of combining these different branches into the final envelope depends on the way they sample the scattering region: for topography (this case), each ray samples a particular area of the surface, different from all the others, hence each contribution should be summed. This also follows from the theoretical development, as shown later.

From Figure 3.1 we can see that, in general, the amplitude of the $PKiKP$ coda envelope depends on the background radial Earth model. For example, for the distance of 80° (right panels) we see a spike in amplitude around a lapse time of 110 s for $P.KP_{CD}$. This sudden increase in amplitude is produced by rays that hit the ICB near the critical angle, resulting in a large value for the corresponding reflection coefficient. Another interesting feature are the "sinks" in amplitude shown for the $P.KP_{CD}$ branch. These rays have a very small reflection coefficient at the ICB, that even crosses 0 twice in the distance range from 74° and 90° according to PREM (*Dziewonski and Anderson*, 1981). Other models for the ICB will produce a different result, as presented in the third row of Figure 3.1. Here we show same computations but with the ICB model proposed by *Koper and Dombrovskaya* (2005). In this case we do not have the "sinks" in the $P.KP_{CD}$ branch, resulting in an envelope with a smoother decay. Note that this effect is produced by the infinite frequency assumption present in ray theory; hence, in the real Earth, the amplitude variation around "sinks" and "peaks" will be smoother due to the finite frequency effect.

In our calculations, the amplitude at zero lapse time represents the amplitude of

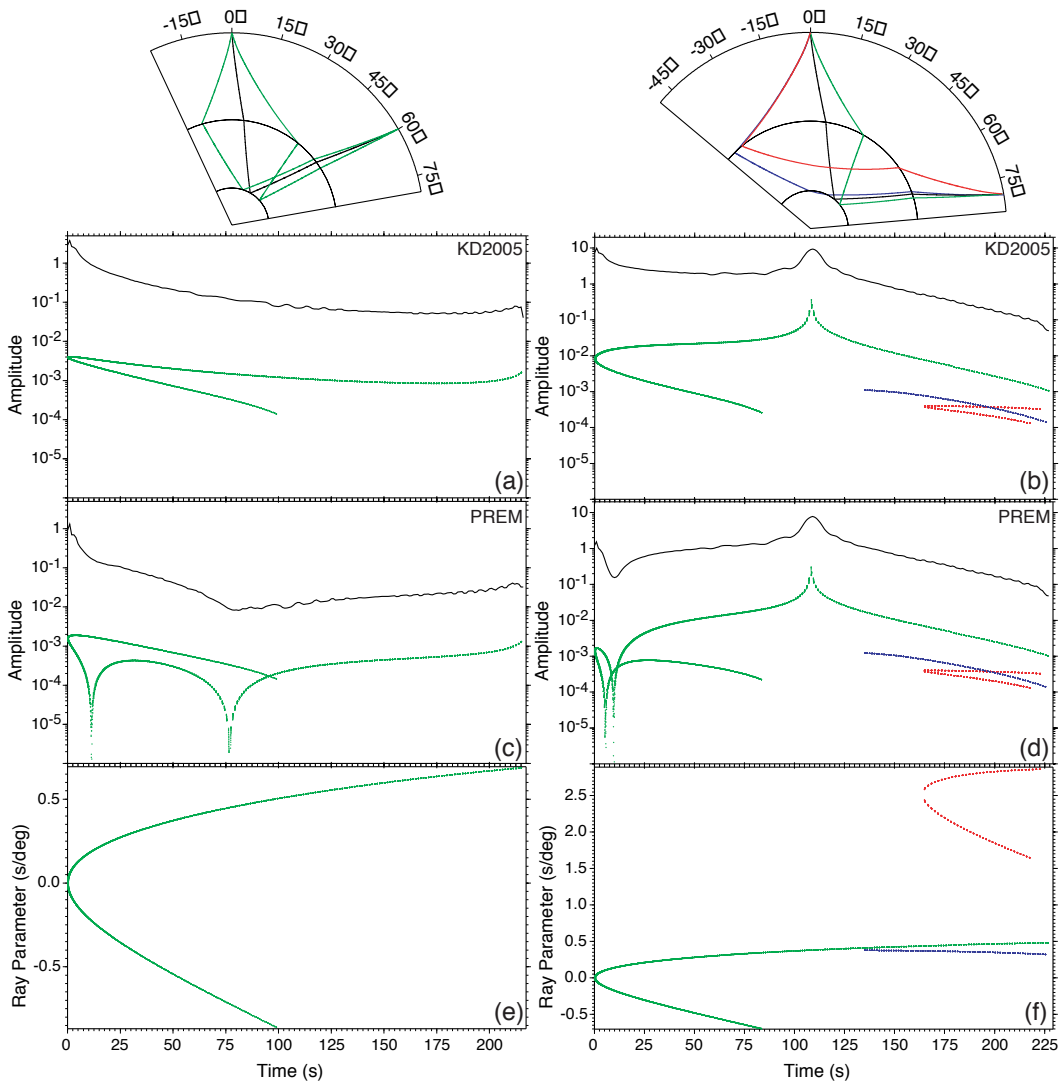

Figure 3.1: Synthetic envelopes of $PKiKP$ coda due to isotropic scattering from the core mantle boundary, source-side, at epicentral distances of 60° (left) and 80° (right). The lower panels ((e) and (f)) show the variation of the ray parameter with time, while the upper panels ((a) to (d)) present the corresponding amplitude for each point. The second row (panels (c) and (d)) was computed using PREM (*Dziewonski and Anderson*, 1981), while the first row (panels (a) and (b)) was computed using the model for the inner core boundary proposed by *Koper and Dombrovskaya* (2005) (KD2005). This model was obtained from $PKiKP/P$ amplitude ratios and predicts a density jump of 0.52 ($kg \cdot m^{-3}$) and an S-wave velocity contrast of 2.82 ($km \cdot s^{-1}$) (the PREM model has values of 0.60 ($kg \cdot m^{-3}$) and 3.50 ($km \cdot s^{-1}$), respectively). The colors represent different branches, with $P.KP_{CD}$ in green, $P.KP_{BC}$ in red, $P.KP_{DF}$ in blue, and the direct arrival in black. The $PKiKP$ envelopes are computed by summing along the different branches, and are shown by the black curves in the middle rows. All values (time, ray parameter, and amplitude) are plotted with respect to those of the direct $PKiKP$. The top figures show some example of ray paths for both epicentral distances; the colors are the same as in the lower panels.

$PKiKP$ computed using the Kirchhoff migration, as done in similar studies (*Scott and Helmberger*, 1983; *Frazer and Sen*, 1985; *Kampfmann and Müller*, 1989). Later we show that this amplitude is a function of the total scattering area considered and of the characteristics of the topography (due to focusing and defocusing effects).

3.2.2 Scattering From Surface Topography

Long Wavelengths

Scattering over a surface can be modeled using Kirchhoff migration (*Haddon and Buchen*, 1981; *Scott and Helmberger*, 1983; *Frazer and Sen*, 1985) applied to a point source (*Kampfmann and Müller*, 1989). This can always be done if the surface is smooth; in other words, if the wavelengths of the topography are larger than the characteristic wavelength of the seismic wave (*Battaille and Flatté*, 1988). Based on Huygens' principle, we consider all the possible points at the scattering surface by tracing all the possible pre-scattering rays starting from the source to the scattering region. Then we compute the interaction with the surface, a function of the pre-scattering ray parameter, the geometry of the surface, and the impedance contrast across the surface. Finally, using Green's functions, we propagate the effect of each point on the surface to the receiver. The final result is the convolution of the time derivative of the source time function (in our case, a 2 s step function) with all the point-scatterer responses previously computed; this results in a summation of the contribution of each single ray.

In our computations we consider the incident plane wave to be traveling in the x-z plane, with a ray parameter p in the direction $\hat{t} = \left\{\sin\theta, 0, \pm\cos\theta\right\}^T$ ((+) when propagating downwards and (-) propagating upwards), where $\sin\theta = p\alpha/r$, α is the P-wave velocity at a radius r, and θ is the incident angle, measured with respect to the vertical. From *Frazer and Sen* (1985) we can write the displacement ($\underline{u}^P$) and the corresponding stress tensor ($\underline{\underline{\tau}}^P$) as:

$$\underline{u}^P = A\hat{t}^P \exp\left(\frac{i\omega}{\alpha}(\hat{t}^P \cdot \underline{x})\right), \tag{3.1}$$

and

$$\underline{\underline{\tau}}^P = \frac{i\omega}{\alpha}[\lambda(\underline{u}^P \cdot \hat{t}^P)\underline{\underline{I}} + 2\mu\underline{u}^P\hat{t}^P], \tag{3.2}$$

where $\underline{\underline{I}}$ is the identity matrix, A represents the amplitude of the plane wave, ω is the main frequency, α represents the P-wave velocity, and λ and μ are the Lamè constants of the medium. For our purposes, we only consider P-waves for the computations, hence we can drop the superscript. Throughout this paper, we use double bars to indicate tensors, single bars to indicate vectors, and hats to indicate unit vectors.

Starting with equations (5) and (9a) of *Frazer and Sen* (1985) (for the case of P-waves) and using Green's Theorem, we can represent the amplitude of the displacement in the receiver by considering the displacement and stresses over the scattering surface, projected into the normal,

$$||\underline{u}(x_r)|| \equiv A_r = \int_\Sigma \hat{\mathrm{n}} \cdot \left(\underline{\underline{\tau}}_1 \cdot \underline{u}_2 - \underline{\underline{\tau}}_2 \cdot \underline{u}_1\right) d\Sigma = \int_\Sigma \underline{u}_1^P \cdot \underline{\underline{R}}_{12}^{PP} \cdot \underline{u}_2^P d\Sigma, \tag{3.3}$$

with (equation (9b) from *Frazer and Sen* (1985))

$$\underline{\underline{R}}_{12}^{PP} = \hat{t}_1^P \grave{P}\acute{P}\frac{i\omega}{\alpha}\hat{t}_1^{PP} \cdot \left\{\lambda_2(\hat{t}_1^{PP}\hat{\mathrm{n}} - \hat{\mathrm{n}}\hat{t}_2^P) + 2\mu_2(\hat{\mathrm{n}}\hat{t}_1^{PP} - \hat{t}_2^P\hat{\mathrm{n}})\right\}, \tag{3.4}$$

where $\underline{u}_1$ the displacement due to a P-wave coming from the source towards the scattering surface (pre-scattering ray), and $\underline{u}_2$ the displacement due to a P-wave traveling from the scattering surface to the receiver (post-scattering ray). Note that λ_2 and μ_2 are the properties of the medium in which $\underline{u}_2$ starts its journey. Ignoring the time dependence, we can write $\underline{u}_1 = A_1\hat{t}_1$ and $\underline{u}_2 = A_2\hat{t}_2$ and substitute into the previous equations, yielding the following expression for the integrand of equation (3.3):

$$\begin{aligned}
\hat{t}_1^P \cdot \underline{\underline{R}}_{12}^{PP} \cdot \hat{t}_2^P &= \hat{t}_1^P \cdot \hat{t}_1^P \grave{P}\acute{P}\frac{i\omega}{\alpha}\hat{t}_1^{PP} \cdot \left\{\lambda(\hat{t}_1^{PP}\hat{\mathrm{n}} - \hat{\mathrm{n}}\hat{t}_2^P) + 2\mu(\hat{\mathrm{n}}\hat{t}_1^{PP} - \hat{t}_2^P\hat{\mathrm{n}})\right\} \cdot \hat{t}_2^P \\
&= (\hat{t}_1^P \cdot \hat{t}_1^P)\left(\grave{P}\acute{P}\frac{i\omega}{\alpha}\right)\left\{\lambda\left[(\hat{t}_1^{PP} \cdot \hat{t}_1^{PP})(\hat{\mathrm{n}} \cdot \hat{t}_2^P) - (\hat{t}_1^{PP} \cdot \hat{\mathrm{n}})(\hat{t}_2^P \cdot \hat{t}_2^P)\right]\right. \\
&\quad \left. +2\mu\left[(\hat{t}_1^{PP} \cdot \hat{\mathrm{n}})(\hat{t}_1^{PP} \cdot \hat{t}_2^P) - (\hat{t}_1^{PP} \cdot \hat{t}_2^P)(\hat{\mathrm{n}} \cdot \hat{t}_2^P)\right]\right\}.
\end{aligned} \tag{3.5}$$

Writing $\hat{t}_1^{PP} = \hat{t}_1^P \cdot \left(\underline{\underline{I}} - 2\hat{\mathrm{n}}\hat{\mathrm{n}}\right)$ (*Aki and Richards*, 2002), and defining $\eta_i \equiv \hat{\mathrm{n}} \cdot \hat{t}_i^P$ and $tt \equiv \hat{t}_1^P \cdot \hat{t}_2^P$, we obtain

$$\hat{t}_1^{PP} \cdot \hat{\mathrm{n}} = \hat{t}_1^P \cdot (\hat{\mathrm{n}} - 2\hat{\mathrm{n}}) = -\left(\hat{t}_1^P \cdot \hat{\mathrm{n}}\right) = -\eta_1, \tag{3.6}$$

and

$$\hat{t}_1^{PP} \cdot \hat{t}_2^P = \hat{t}_1^P \cdot \left(\hat{t}_2^P - 2\hat{\mathrm{n}}(\hat{\mathrm{n}} \cdot \hat{t}_2^P)\right) = \hat{t}_1^P \cdot \hat{t}_2^P - 2(\hat{t}_1^P \cdot \hat{\mathrm{n}})\eta_2 = tt - 2\eta_1\eta_2. \tag{3.7}$$

Substituting equations (3.6) and (3.7) into equation (3.5), we have

$$\begin{aligned} \hat{t}_1^P \cdot \underline{\underline{R}}_{12}^{PP} \cdot \hat{t}_2^P &= \left(\grave{P}\acute{P}\frac{i\omega}{\alpha}\right)\{\lambda\left[\eta_2 + \eta_1\right] + 2\mu\left[-\eta_1(tt - 2\eta_1\eta_2) - \eta_2(tt - 2\eta_1\eta_2)\right]\} \\ &= \left(\grave{P}\acute{P}\frac{i\omega}{\alpha}\right)(\eta_2 + \eta_1)\left\{\lambda - 2\mu(tt - 2\eta_1\eta_2)\right\}. \end{aligned} \tag{3.8}$$

If we define $\sigma \equiv \beta/\alpha$, this becomes

$$\begin{aligned} \hat{t}_1^P \cdot \underline{\underline{R}}_{12}^{PP} \cdot \hat{t}_2^P &= \left(\grave{P}\acute{P}i\omega\right)(\eta_2 + \eta_1)\left\{(\rho\alpha - 2\rho\sigma\beta) - 2\sigma\beta(tt - 2\eta_1\eta_2)\right\} \\ &= \left(\grave{P}\acute{P}i\omega\right)(\eta_2 + \eta_1)\left\{\rho\alpha - 2\rho\sigma\beta(1 + tt - 2\eta_1\eta_2)\right\}. \end{aligned} \tag{3.9}$$

Substituting this expression for the integrand of equation (3.3), we obtain

$$A_r = \int_\Sigma A_1 A_2 \mathcal{R}(\underline{x}_\Sigma, \hat{t}_1, \hat{t}_2) d\Sigma, \tag{3.10}$$

with

$$\mathcal{R}(\underline{x}_\Sigma, \hat{t}_1, \hat{t}_2) = \left(\grave{P}\acute{P}i\omega\right)(\eta_1 + \eta_2)\left\{1 - 2\sigma^2(1 + tt - 2\eta_1\eta_2)\right\}, \tag{3.11}$$

as an apparent reflection coefficient due to the presence of topography. Note that in equation (3.10) we have a summation over all the area, which in turn involves all the possible rays that sample that area. Hence, we see that in this case, all the different branches need to be summed to generate the final envelope. In the case of small or

null topography, we have

$$\left\{1 - 2\sigma^2(1 + tt - 2\eta_1\eta_2)\right\} \approx 1, \tag{3.12}$$

and

$$\mathcal{R}(\underline{x}_\Sigma, \hat{t}_1, \hat{t}_2) \approx \left(\grave{P}\acute{P}i\omega\right)(\eta_1 + \eta_2), \tag{3.13}$$

which is equivalent to equation (4) of *Kampfmann and Müller* (1989).

Small Topography

Another approach to this problem was given by *Kennett* (1972) for the 1D case, and extended by *Doornbos* (1978) to the 2D, where small amplitude topography is taken as perturbations from a planar surface. By considering continuity of displacements and stresses over the surface of the topography, we get a representation of the scattered wavefield as a distribution of sources over this surface (*Battaille and Flatté*, 1988; *Battaille et al.*, 1990). A similar approach was previously taken by *Gilbert and Knopoff* (1960), but limited to topography on a free surface. Following *Doornbos* (1978), equation (19) for a solid-solid interface or (20) for a solid-liquid interface, we can write the displacement at the receiver as

$$\underline{u}_r = \underline{u}(\underline{x}_r, t) = \int_\Sigma \underline{\underline{H}}_G(\underline{x}_r, \underline{x}')[\underline{B}(\underline{x}')]_1^2 d\Sigma, \tag{3.14}$$

where $\underline{\underline{H}}_G(\underline{x}_r, \underline{x}')$ is a matrix composed by Green's Functions for displacement and stresses, and $[\underline{B}(\underline{x}')]_1^2 = \{\underline{u}_{\text{out}}, \underline{\tau}_{\text{out}}\}^T$ is the discontinuity of the displacement-stress vector between mediums 1 and 2, which are divided by the topography. This can be rewritten in a more usual form as:

$$\underline{u}_r = \int_\Sigma (\underline{\underline{\tau}}_G \underline{u}_{\text{out}} - \underline{\underline{\tau}}_{\text{out}} \underline{u}_G) d\Sigma. \tag{3.15}$$

From equation (18) of *Doornbos* (1978) we can express the discontinuity in the

displacement-stress vector as

$$[\underline{B}(\underline{x}')]_1^2 = \int F(\underline{k}-\underline{\kappa})\underline{\underline{L}}(\underline{k},\underline{\kappa})\underline{B}_0 \exp(-i\underline{\kappa}\cdot\underline{x}')d\underline{\kappa} \tag{3.16}$$

where $F(\underline{k})$ is the Fourier transform (in spatial domain) of the topography, $\underline{\kappa}$ corresponds to the 2 D wavenumber of the incident plane wave, $\underline{\underline{L}}$ is shown in equations (17) and (21) of *Doornbos* (1978) and depends upon the physical properties of both mediums (i.e. the Lame constants λ and μ), and $\underline{B}_0$ represents the incident displacement-stress vector. Defining the displacement produced by the wavefield leaving the scattering surface,

$$\underline{u}_{\text{out}} = F\underline{\underline{L}}^U\underline{B}_0 = FA_{\text{out}}\hat{t}_{\text{out}} \tag{3.17}$$

and its corresponding stress as

$$\underline{\tau}_{\text{out}} = F\underline{\underline{L}}^D\underline{B}_0 = FA_{\text{tou}}\hat{t}_{\text{tou}} \tag{3.18}$$

where $\underline{\underline{L}}^{U/D}$ represents the upper/lower part of the matrix $\underline{\underline{L}}$. Translating $\underline{\tau}_{\text{out}}$ into matrix notation, we have $\underline{\underline{\tau}}_{\text{out}} = [\underline{\tau}_{\text{out}}\hat{\text{k}}] + [\hat{\text{k}}\underline{\tau}_{\text{out}}]$.

Next we consider the Greens Functions that link the scattering surface with the receiver. Note that these functions are composed of several rays, in particular we consider the post-scattering ray $\underline{u}_2$ with the corresponding stresses $\underline{\underline{\tau}}_2$ (a plane wave with direction $\hat{t}_2$ and amplitude A_2, see equations (3.1) and (3.2)). In order to compute the amplitude, we project the displacement on the direction of propagation, in this case $\hat{t}_2$:

$$\begin{aligned}
\underline{u}_r\cdot\hat{t}_2 &\equiv A_r \\
&= \int_\Sigma F\hat{t}_2\cdot\left\{\left(\tfrac{i\omega}{\alpha_2}\right)A_2(\lambda_2\underline{\underline{I}}+2\mu_2[\hat{t}_2\hat{t}_2])\right\}\cdot\underline{u}_{\text{out}} - \hat{t}_2\cdot\{[\underline{\tau}_{\text{out}}\hat{\text{k}}]+[\hat{\text{k}}\underline{\tau}_{\text{out}}]\}\cdot A_2\hat{t}_2 d\Sigma \\
&= \int_\Sigma A_2F\left\{\left(\frac{i\omega}{\alpha_2}\right)(\lambda_2+2\mu_2)(\hat{t}_2\cdot\underline{u}_{\text{out}}) - 2(\hat{t}_2\cdot\underline{\tau}_{\text{out}})(\hat{\text{k}}\cdot\hat{t}_2)\right\}d\Sigma \\
&= \int_\Sigma A_2F\left\{(i\omega\alpha_2\rho_2)(\hat{t}_2\cdot\underline{u}_{\text{out}}) - 2(\hat{t}_2\cdot\underline{\tau}_{\text{out}})(\hat{\text{k}}\cdot\hat{t}_2)\right\}d\Sigma
\end{aligned} \tag{3.19}$$

We see that the resulting amplitude is the product of the propagation of the post-scattering ray from the surface to the receiver, the projection of the out-going displacement (due to the topography) and stress into the ray that connects the scattering surface and the receiver (post-scattering). Note that the pre-scattering ray affects the out-going displacement and stresses through the displacement-stress vector ($\underline{B}_0$), as can be seen in equation (3.20).

In the liquid-solid case, we have that $\underline{B}_0 = \{u^1_{x0}, u^2_{x0}, u^1_{y0}, u^2_{y0}, u_{z0}, \tau_{zz0}\}^T$ (from equation (7) of *Doornbos* (1978)). The subindex 0 represents the plane wave solution without topography; the superscript stands for evaluating the quantity in the solid (1) or in the liquid (2). For an incoming plane wave in the solid (pre-scattering), this displacement-stress vector will be (see Figure 3.2 for reference):

$$\underline{B}_0 = A_1 \begin{Bmatrix} (1 + \grave{P}\acute{P})(\hat{t_1} \cdot \hat{\imath}) \\ \grave{P}\grave{P}(\hat{t_1} \cdot \hat{\imath}) \\ (1 + \grave{P}\acute{P})(\hat{t_1} \cdot \hat{\jmath}) \\ \grave{P}\grave{P}(\hat{t_1} \cdot \hat{\jmath}) \\ (1 - \grave{P}\acute{P})(\hat{t_1} \cdot \hat{\mathrm{k}}) \\ (i\omega/\alpha_1)\left(\lambda_1 + 2\mu_1(\hat{t_1} \cdot \hat{\mathrm{k}})^2\right) \end{Bmatrix}. \tag{3.20}$$

Since we are only considering a plane wave polarized in the x-z axis $\hat{t_1} \cdot \hat{\jmath} = 0$. Here, we follow the notation given by *Kennett* (2001), defining $\nu_i \equiv 4\rho_i\beta_i^2(1 - 2\sigma_i^2)$ and $\sigma_i \equiv \beta_i/\alpha_i$. To compute the resulting displacement ($\underline{u}_{\text{out}}$) we consider equation

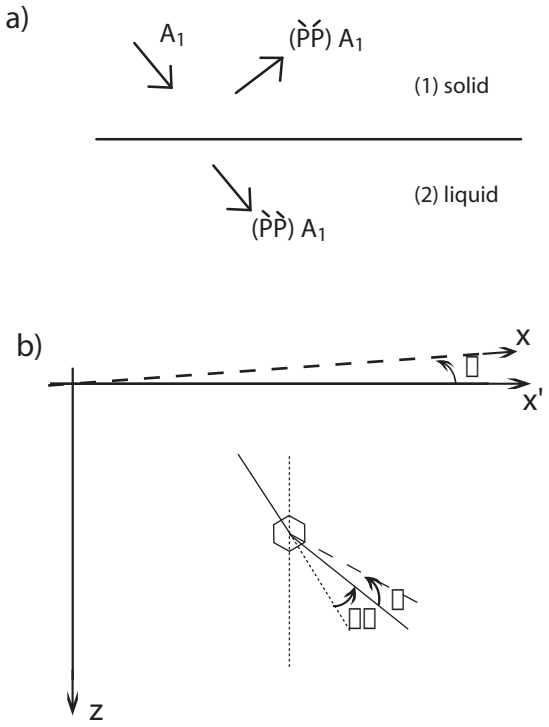

Figure 3.2: a) Schematic diagram of amplitudes produced by an incident plane wave with amplitude A_1 from the medium (1) (solid). $(\acute{P}\grave{P})$ and $(\grave{P}\grave{P})$ represent the reflection and transmission coefficient at the interface, respectively. b) Schematic representation of the change in coordinates due to a rotation γ around the z-axis. Also is shown the change in angle due to the scattering ($\Delta\theta$) produce by a heterogeneity (hexagon).

(3.17) and the upper part of the $\underline{\underline{L}}$ matrix, as follows

$$\begin{aligned}
\underline{u}_{\text{out}} &= F\underline{\underline{L^U}} \cdot \underline{B}_0 \\
&= F(\underline{k}-\underline{\kappa})\left[i(2\kappa_x\sigma_1^2-k_x),\quad ik_x,\quad -ik_y,\quad ik_y,\quad 0,\quad -\Delta(\lambda+2\mu)^{-1}\right]\cdot\underline{B}_0 \\
&= A_1F(\underline{k}-\underline{\kappa})\Big\{i(2\kappa_x\sigma_1^2-k_x)(1+\grave{P}\acute{P})(\hat{t}_1\cdot\hat{\imath})+ik_x\grave{P}\acute{P}(\hat{t}_1\cdot\hat{\imath}) \\
&\qquad +\frac{\Delta\lambda+2\Delta\mu}{(\lambda_1+2\mu_1)(\lambda_2+2\mu_2)}(i\omega/\alpha_2)\left(\lambda_1+2\mu_1(\hat{t}_1\cdot\hat{\mathrm{k}})^2\right)\Big\}\hat{\mathrm{k}} \\
&= A_1f(\underline{x})(i\omega/\alpha_1)\Big\{(2\sigma_1^2-1)(1+\grave{P}\acute{P})(\hat{t}_1\cdot\hat{\imath})+\grave{P}\acute{P}(\hat{t}_1\cdot\hat{\imath}) \\
&\qquad +\frac{\Delta\lambda+2\Delta\mu}{(\lambda_1+2\mu_1)(\lambda_2+2\mu_2)}\left(\lambda_1+2\mu_1(\hat{t}_1\cdot\hat{\mathrm{k}})^2\right)\Big\}\hat{\mathrm{k}} \\
&= A_1F(\underline{x})\left(\frac{i\omega}{\alpha_1}\right)\underline{\mathrm{t}}_u, \qquad (3.21)
\end{aligned}$$

where we have used $\kappa_x = \omega/\alpha_1(\hat{t}_1\cdot\hat{\imath})$, and that the inverse Laplace transform of a multiplication by $k_x\underline{u}_1$ is $-i\partial\underline{u}_1/\partial x$. Considering a plane wave, $\partial\underline{u}_1/\partial x = (i\omega/\alpha_1)(\hat{t}_1\cdot\hat{\imath})\underline{u}_1$ then by taking the inverse Fourier transform, we get $k_x \to (\omega/\alpha_1)(\hat{t}_1\cdot\hat{\imath})$. Similarly, if we consider equation (3.18) and the lower part of matrix $\underline{\underline{L}}$,

$$\begin{aligned}
\underline{\tau}_{\text{out}} &= F\underline{\underline{L^D}} \cdot \underline{B}_0 \\
&= F(\underline{k}-\underline{\kappa})\begin{bmatrix} \omega^2\rho_1-k_x\kappa_x\nu_1, & 0, & -k_y\kappa_x\mu_1, & 0, & 0, & i(2k_x\sigma_1^2-\kappa_x) \\ -2k_y\kappa_x\lambda_1\sigma_1^2, & 0, & \omega^2\rho_1-k_x\kappa_x\mu_1, & 0, & 0, & 2ik_y\sigma_1^2 \\ 0, & 0, & 0, & 0, & \omega^2\Delta\rho, & 0 \end{bmatrix}\cdot\underline{B}_0 \\
&= A_1F(\underline{k}-\underline{\kappa})\begin{Bmatrix} (\omega^2\rho_1-k_x\kappa_x\nu_1)(1+\grave{P}\acute{P})(\hat{t}_1\cdot\hat{\imath})-(i^2\omega/\alpha_1)\left(\lambda_1+2\mu_1(\hat{t}_1\cdot\hat{\mathrm{k}})^2\right)(2k_x\sigma_1^2-\kappa_x) \\ (-2k_y\kappa_x\lambda_1\sigma_1^2)(1+\grave{P}\acute{P})(\hat{t}_1\cdot\hat{\imath})+2(i^2\omega/\alpha_1)k_y\sigma_1^2\left(\lambda_1+2\mu_1(\hat{t}_1\cdot\hat{\mathrm{k}})^2\right) \\ (\omega^2\Delta\rho)(1-\grave{P}\acute{P})(\hat{t}_1\cdot\hat{\mathrm{k}}) \end{Bmatrix} \\
&= A_1f(\underline{x})\left(\frac{\omega}{\alpha_1}\right)^2\begin{Bmatrix} \left(\alpha_1^2\rho_1-(\hat{t}_1\cdot\hat{\imath})^2\nu_1\right)(1+\grave{P}\acute{P})(\hat{t}_1\cdot\hat{\imath})+\left(\lambda_1+2\mu_1(\hat{t}_1\cdot\hat{\mathrm{k}})^2\right)(2\sigma_1^2-1) \\ 0 \\ \Delta\rho\alpha_1^2(1-\grave{P}\acute{P})(\hat{t}_1\cdot\hat{\mathrm{k}}) \end{Bmatrix} \\
&= A_1f(\underline{x})\left(\frac{\omega}{\alpha_1}\right)^2\underline{\mathrm{t}}_\tau, \qquad (3.22)
\end{aligned}$$

noting that $k_y \to -(\omega/\alpha_1)(\hat{t}_1\cdot\hat{\mathrm{j}}) = 0$. Substituting back into equation (3.19) we can

write

$$\begin{aligned} A_r &= \int_\Sigma A_1 A_2 \left(\frac{i\omega}{\alpha_1}\right)^2 f(\underline{x}) \left\{(\alpha_2^2\rho_2)(\hat{t}_2 \cdot \underline{\mathrm{t}}_u) + (\hat{t}_2 \cdot \underline{\mathrm{t}}_\tau)(\hat{\mathrm{k}} \cdot \hat{t}_2)\right\} d\Sigma \\ &= \int_\Sigma A_1 A_2 \mathcal{R}(\underline{x}, \hat{t}_1, \hat{t}_2) d\Sigma, \end{aligned} \tag{3.23}$$

with the apparent reflection coefficient ($\mathcal{R}$) given as

$$\mathcal{R}(\underline{x}, \hat{t}_1, \hat{t}_2) = (i\omega/\alpha_1)^2 f(\underline{x}) \left\{(\alpha_2^2\rho_2)(\hat{t}_2 \cdot \underline{\mathrm{t}}_u) + (\hat{t}_2 \cdot \underline{\mathrm{t}}_\tau)(\hat{\mathrm{k}} \cdot \hat{t}_2)\right\}. \tag{3.24}$$

Again, in equation (3.23) we have an integral over the scattering area of all the possible rays that sample this area. Therefore, to compute the resulting envelope we need to sum all the contributions of individual rays.

Descriptions of Surface Topography

Previous studies of scattering from surface topography have usually either assumed a specific autocorrelation function (ACF) to describe the nature of the topography and then computed the average response of the medium (*Chernov*, 1960; *Wu and Aki*, 1985a,b; *Frankel and Clayton*, 1986; *Battaille and Flatté*, 1988; *Sato and Fehler*, 1998), or have used a thin layer of volumetric heterogeneities as a proxy for topography (*Hedlin et al.*, 1997). In this work, we follow the same procedure as *Kampfmann and Müller* (1989) and *Shearer et al.* (1998), by computing particular realizations of random topography with a given ACF, and then taking an average over the ensemble of corresponding synthetic codas.

Considering a sphere with radius r_{ref} (radius of the layer in which the topography is located, in our case, the core-mantle boundary or the inner core boundary) we superimpose a topographic undulation. We considered several possibilities for the ACF of the topography, as done in previous studies (*Frankel and Clayton*, 1986; *Kampfmann and Müller*, 1989; *Sato and Fehler*, 1998). In general, for a function $f(\underline{x})$ with the corresponding Fourier transform $F(\underline{m})$ in the wavenumber domain, the

ACF can be computed as

$$N(\underline{x}) = \langle f(\underline{x}+\underline{\xi})f(\underline{\xi})\rangle = \frac{1}{A}\int_A f(\underline{x}+\underline{\xi})f(\underline{\xi})dA_\xi, \tag{3.25}$$

where A is a surface (range of $f(\underline{x})$). The corresponding Fourier transform is known as the power spectral density function (PSDF) (*Sato and Fehler*, 1998),

$$\mathcal{F}\left[N(\underline{x})\right] \equiv P(\underline{m}) = \frac{1}{A}F^*(\underline{m})F(\underline{m}) = \frac{1}{A}||F(\underline{m})||^2 \tag{3.26}$$

where $F^*(\underline{m})$ is the complex conjugate of $F(\underline{m})$. Using relation (3.26) we can obtain the Fourier coefficients for a particular power spectral density, for example,

$$\begin{aligned} C_{ij} &= s\cdot a/4\cdot\exp(-m_{ij}^2a^2/8) \qquad \text{(Gaussian)} \\ C_{ij} &= s\cdot a/(1+m_{ij}^2a^2)^{3/4} \qquad \text{(Exponential)} \\ C_{ij} &= s\cdot\delta(m_0-m_{ij}) \qquad \text{(Delta)} \end{aligned} \tag{3.27}$$

where $\delta(m)$ is the Kronecker delta function. In these expressions we have considered that a represents the correlation distance with the corresponding wavenumber m_a, $m_{ij} = ||\underline{m}_{ij}|| = \sqrt{(m_i^x)^2+(m_j^y)^2}$ (we assume isotropic media), and the factor s is for the normalization. We compute these normalization factors following *Frankel and Clayton* (1986), who have taken into account the discretization in the space domain, leading to a maximum (Nyquist) wavenumber. For a discrete representation of the function $f(\underline{x})$ the standard deviation can be computed from:

$$\sigma^2 = \int_0^{m_N} m\cdot P(m)dm \tag{3.28}$$

with m_N being the Nyquist wavenumber. For the ACFs presented above, we have:

$$\begin{aligned} \sigma^2 &= 1-\exp(-m_N^2a^2/4) \quad \text{(Gaussian)} \\ \sigma^2 &= 1-(1+m_N^2a^2)^{-1/2} \quad \text{(Exponential)} \\ \sigma^2 &= m_0 \quad \text{(Delta)} \end{aligned} \tag{3.29}$$

where the first two expressions are the same as equations B4 and B7 from *Frankel and Clayton* (1986). In order to obtain a particular root-mean-square (rms) for our model representation, we define the parameter s as

$$s = \frac{rms}{\sigma} \tag{3.30}$$

and compute σ as previously showed, depending on the case. For simplicity, we assume that the scattering region is a square with side L, and the same sampling interval in x and y axis (dL), leading to:

$$\begin{aligned} dm_x &= dm_y = \frac{2\pi}{L} \\ m_i^x &= m_j^y \quad \text{if} \quad i = j \\ m_N^x &= m_N^y = \frac{\pi}{dL} \\ M_x &= M_y = M \end{aligned} \tag{3.31}$$

As discussed in *Sato and Fehler* (1998), the main difference between the Gaussian and Exponential autocorrelation functions is the power at high-frequencies: the second representation has more energy in the small wavelengths. Hence, special attention should be given to the sampling of the heterogeneous region in order to allow the proper representation of the power spectrum beyond the characteristic wavenumber. We found that, in general, the Nyquist wavenumber should be $m_N \geq 5m_a$. To have the full representation in the Fourier wavenumber domain, we need to define the phase spectrum, which depends upon the relative position of the source, receiver, and the scattering surface. In order to generate different surfaces with the same power spectrum, we assign random numbers for the phases and then compute a particular realization of the topography by taking the inverse Fourier Transform. We present sample realizations of CMB topography for various ACFs in Figure 3.3.

The outward normal to the topography at any point can be found given the angles

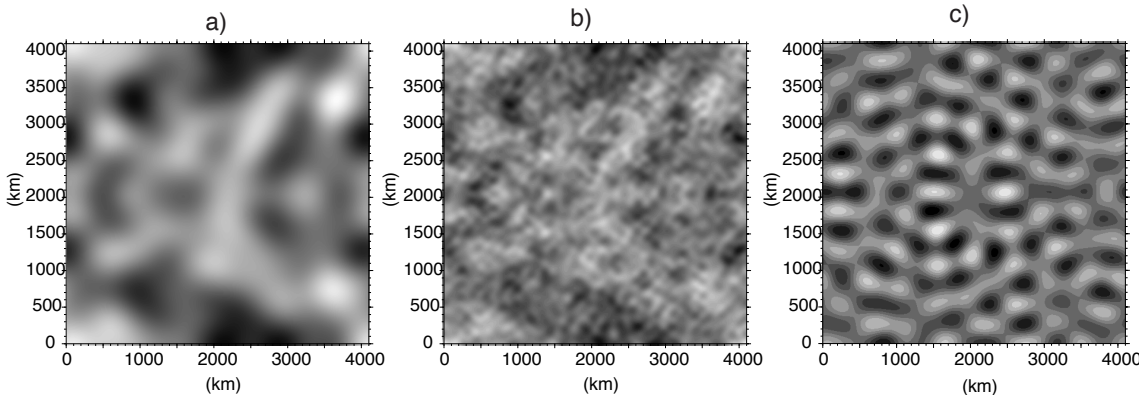

Figure 3.3: Different realizations done with a characteristic wavelength of 250 km for topography at the core mantle boundary. The different cases are: a) Gaussian autocorrelation function (ACF), b) Exponential ACF, and c) Delta in power spectrum. All of them have the same rms amplitude.

$\phi_x = \tan^{-1}(\delta f/\delta x)$ and $\phi_y = \tan^{-1}(\delta f/\delta y)$, as follows:

$$\hat{\mathrm{n}} = \frac{1}{||\underline{\mathrm{n}}||} \begin{Bmatrix} -\sin\phi_x \\ -\sin\phi_y \\ -\cos\phi_x \cos\phi_y \end{Bmatrix} \approx \begin{Bmatrix} -\delta f/\delta x \\ -\delta f/\delta y \\ -1 \end{Bmatrix} \tag{3.32}$$

where we have assumed that $(\delta f/\delta x)^2 \approx 0$ and $(\delta f/\delta y)^2 \approx 0$. This assumption is made in both methods involving topography used here (*Frazer and Sen*, 1985; *Kennett*, 1972).

Here we have used Cartesian coordinates to represent the topography at the reference radius r_{ref} as departures from the usual sphere. The deformation of this surface into spherical coordinates is done in the ray tracing: by using a radial model, the computation of the pre- or post-scattering ray only requires the epicentral distance. For two points with the same value on the y-axis, the difference in the x-axis will lead to different epicentral distances and azimuths. Only the first affects the computations on the ray tracing, while the second is relevant in computing the change in direction, as shown later on. The sampling on the y-axis is done at a fixed value and the x-axis is adequately changed in order to have the same distance in both directions. We solve this issue by considering a fixed epicentral distance (same angle) from the source,

then we explore all the possible azimuths and search for those ones that result in an appropriate backazimuth (considering a deviation from the theoretical value) at the receiver. Note that for the same epicentral distance but different backazimuth at the station, the second ray (from the scattering region to the receiver, post-scattering ray) will be different. After we cover all the possible angles (from 0° to 90°) we move to a different epicentral distance from the source.

In the synthesis of P_{diff} coda, *Earle and Shearer* (2001) considered all the possible locations of scatterers in the heterogeneous region, in contrast to our work where we define the scattering region on the basis of the backazimuth and the anomaly. This is due to the fact that we work with arrays, while previous work (*Earle and Shearer*, 2001) only considered single stations, precluding the precise determination of the backazimuth. In section 2.4.1, we discuss the methodology used to consider the backazimuth anomalies in the computation of $PKiKP$ coda envelopes.

3.2.3 Volumetric Scattering

Scattering over a volume can be obtained by considering the propagation of elastic waves through a random, inhomogeneous medium (*Chernov*, 1960; *Knopoff and Hudson*, 1964, 1967; *Haddon and Cleary*, 1974; *Wu and Aki*, 1985a,b), as done in similar studies (*Battaille and Flatté*, 1988; *Battaille et al.*, 1990; *Hedlin et al.*, 1997; *Shearer et al.*, 1998; *Hedlin and Shearer*, 2002; *Braña and Helffrich*, 2004). The interaction between the seismic waves and the heterogeneous medium can be modeled by an "equivalent" reflection coefficient that depends upon the scattering angle (change in angle of propagation due to the scattering) and the properties of the medium. Considering equation (23) from *Wu and Aki* (1985b), we can express the displacement due to scattering from an inhomogeneous medium as

$$u_i(\underline{x}) = \int Q_j(\underline{\xi}) * G_{ij}(\underline{x}, \underline{\xi}) dV, \tag{3.33}$$

where G_{ij} is the elastodynamic Green's function and Q_j is the equivalent body forces due to the presence of heterogeneities in the volume V, obtained using the Born

approximation (*Wu and Aki*, 1985b). From the results obtained by *Wu and Aki* (1985a,b) and taking the mean square of (3.33) only for the P to P component, we obtain

$$\left\langle |u(\underline{x})|^2 \right\rangle = \frac{m^4 V}{(4\pi)^2} R(\Theta) \int \frac{1}{G^2(\underline{\xi}, \underline{x})} N(\underline{\xi} - \underline{\eta}) \exp\left(im(\hat{x}_1 - \hat{x}) \cdot (\underline{\xi} - \underline{\eta})\right) dV, \quad (3.34)$$

where m is the wavenumber, $G(\underline{\xi}, \underline{x})$ the geometrical spreading from the point over the volume $\underline{\xi}$ to receiver at $\underline{x}$, $R(\Theta)$ is the direction factor for the Rayleigh elastic wave scattering by a unit volume, Θ is the scattering angle (given by the change in direction due to the scattering process), and $N(\underline{x})$ the autocorrelation function of the random parameters in the medium. Note that the result presented here is an average over the whole scattering volume and not from a single heterogeneity; hence, the final coda should be computed by averaging over all the rays that sample similar regions in the scattering volume. We follow the method used by *Shearer et al.* (1998) and model the volumetric heterogeneity as composed by spherical shells with constant radius, and calculate the response for each one separately. Later, the total effect can be obtained by summing in power the response kernels.

Previous studies have usually considered a Poisson solidus (*Wu and Aki*, 1985a,b; *Sato and Fehler*, 1998), an assumption not valid for the inner core. If we consider equation (13) of *Wu and Aki* (1985a), the direction factor for the Rayleigh elastic wave scattering by a unit volume can be written as

$$R(\Theta) = \left\langle \left(\frac{\delta\rho}{\rho_0} \cos\Theta - \frac{\delta\lambda}{\lambda_0 + 2\mu_0} - 2\frac{\delta\mu}{\lambda_0 + 2\mu_0} \cos^2\Theta \right)^2 \right\rangle, \quad (3.35)$$

where we have assumed that $\delta\rho$, $\delta\lambda$, and $\delta\mu$ are totally uncorrelated, ρ_0 is the density, λ_0 and μ_0 are the Lamé constants of the medium, and Θ is the scattering angle. If we consider $\lambda_0 = C\mu_0$, then $\lambda_0 + 2\mu_0 = \begin{cases} \lambda_0(1 + 2/C) \\ \mu_0(C + 2) \end{cases}$. Substituting into the previous

equation:

$$R(\Theta) = \left\langle \left(\frac{\delta\rho}{\rho_0}\cos\Theta - \frac{\delta\lambda}{\lambda_0(1+2/C)} - 2\frac{\delta\mu}{\mu_0(C+2)}\cos^2\Theta \right)^2 \right\rangle . \tag{3.36}$$

Introducing the P-wave impedance perturbation ($\delta Z_\alpha/Z_\alpha$) and the P-wave velocity perturbation ($\delta\alpha/\alpha_0$) (as in *Wu and Aki*, 1985a,b), we obtain:

$$\begin{aligned} R(\Theta) &= \left\langle \left(\frac{\delta Z_\alpha}{Z_\alpha}\right)^2 \right\rangle \left(\cos\Theta - \frac{C}{C+2} - \frac{2}{C+2}\cos^2\Theta \right)^2 \\ &+ \left\langle \left(\frac{\delta\alpha}{\alpha_0}\right)^2 \right\rangle \left(\cos\Theta + \frac{C}{C+2} + \frac{2}{C+2}\cos^2\Theta \right)^2 \\ &- 2\left\langle \left(\frac{\delta Z_\alpha}{Z_\alpha}\frac{\delta\alpha}{\alpha_0}\right) \right\rangle \left(\cos^2\Theta - \left(\frac{C}{C+2} + \frac{2}{C+2}\cos^2\Theta \right)^2 \right) \end{aligned} \tag{3.37}$$

Note that if $C = 1$ (i.e. $\lambda_0 = \mu_0$) we fall into equation (20) from *Wu and Aki* (1985a). In general, $C = (\alpha_0/\beta_0)^2 - 2$, which just below the inner core boundary has a value of $C = 7.9$, much larger than 1. In Figure 3.4 we present the effect of a non-Poisson solid in the direction factor for the Rayleigh elastic wave scattering by unit volume ($R(\Theta)$). In this Figure, red is for forward scattering and blue for backward, while dashed lines were computed considering a Poissonian solid ($C = 1.0$) and continuous lines for a non-Poissonian, inner core case ($C = 7.9$). In general, volumetric heterogeneities located at the lower mantle will mainly produce forward scattering, sensitive to the P-wave velocity perturbation ($\delta\alpha/\alpha_0$), while volumetric heterogeneities inside the IC will produce mainly backward scattering, sensitive to the P-wave impedance perturbation ($\delta Z_\alpha/Z_\alpha$). Also note that for the inner core rheology we obtain more side scattering.

In analogy with equations (3.11) and (3.24) for topographic scattering, an apparent reflection coefficient can be obtained from equation (12) from *Wu and Aki* (1985a) (there is a minor typographical error) or by conveniently treating equation

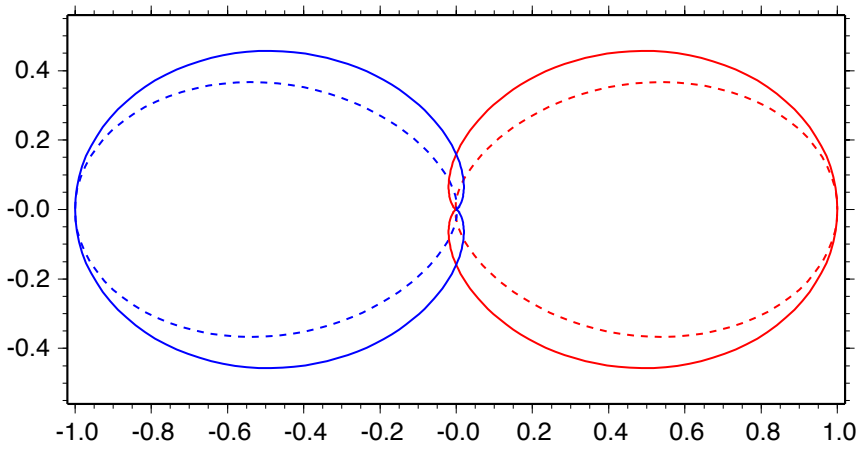

Figure 3.4: Amplitude of the direction factor for the Rayleigh elastic wave scattering by unit volume ($R(\Theta)$) for a Poisson solid ($C = 1.0$) (dashed lines) and a non-Poissonian solid, inner core case ($C = 7.9$) (continuous lines). Red is for forward scattering and only has a P-wave velocity change; blue is back-scattering and only has a P-wave impedance contrast change. The values have been normalized to the corresponding maxima.

(3.34) (see *Wu and Aki*, 1985a,b) as

$$\mathcal{R}^2(m,\Theta) = \frac{V}{4\pi}\left(\frac{\omega}{\alpha_1}\right)^4 R(\Theta)P(2m\sin\Theta/2), \tag{3.38}$$

where V represents the volume of the heterogeneous region and $P(m)$ is the Fourier Transform (in the space domain) of the autocorrelation function $N(\underline{x})$, that corresponds to scalar wave scattering function (see equation (11) from *Wu and Aki* (1985a)). This corresponds to the power spectral density function ($P(m)$, being $m = \omega/\alpha_0$ the wavenumber), but evaluated in the exchange slowness $2m\sin\Theta/2$, due to change in direction produced by the scattering process (*Wu and Aki*, 1985a). Note that this value has already considered the description of the medium (through the consideration of the ACF) and it have already been averaged over the heterogeneous medium, meaning that the final answer is an ensemble over different realizations. For this reason, when computing the result given by the scattering due to a heterogeneous medium through the use of this "apparent" reflection coefficient, the resulting amplitudes for the different rays should be averaged and not summed, as done in the topography case.

The choice of the ACF remains open: some authors (*Knopoff and Hudson*, 1964, 1967; *Haddon and Cleary*, 1974; *Doornbos*, 1976) have used a Gaussian autocorrelation function, while others (*Wu and Aki*, 1985a,b) have selected an Exponential ACF. Here we consider a third choice, the delta function in power spectrum. For each of these cases, we have

- Gaussian ACF:

$$\mathcal{R}^2(m,\Theta) = Vs^2\sqrt{\pi}a^3m^4R(\Theta)\exp\left(-\left(\frac{ma\sin\Theta}{2}\right)^2\right) \tag{3.39}$$

- Exponential ACF:

$$\mathcal{R}^2(m,\Theta) = Vs^2m^4R(\Theta)\frac{2a^3}{\{1+(2ma\sin\Theta/2)^2\}^2} \tag{3.40}$$

- Delta in power spectrum:

$$\mathcal{R}^2(m,\Theta) = Vs^2m^4R(\Theta)\delta(m_a - 2m\sin\Theta/2) \tag{3.41}$$

here, a stands for the characteristic wavelength of the scatterers (or correlation distance for the ACF) with the corresponding wavenumber $m_a = 2\pi/a$, and s is the rms of the heterogeneity. In general, we have a trade-off between the volume of the heterogeneous region, the rms perturbation in P-wave impedance, P-wave velocity, or both, and the scale-length of the heterogeneities.

As we have seen, as the time lapse from the $PKiKP$ arrival increases, the difference in ray parameter, and in scattering angle, changes dramatically. Hence, for the delta in power spectrum we only have a response for a very defined point in time, the one that satisfies the relation $m = m_a/(2\sin\Theta/2)$. We can conclude that if there is a primary wavelength in the distribution of heterogeneities over a volume, the effect is not a usual coda, but a concentrated spike in time. This phenomenon has not been observed in the data, so we do not consider this particular representation in our experiments.

3.2.4 Other Considerations

Backazimuth Anomalies

Haddon and Cleary (1974) determined the location of scatterers at the CMB, even outside the sagittal plane, by studying the anomalies in the backazimuth from the theoretical value. Because we use ray theory, the computations are always done in the plane that contains the great-circle path, with no anomalies in the backazimuth. In general, anomalies in the value of the backazimuth will influence the shape of the coda because it increases the size of the scattering region, as shown in Figure 3.5, on the left. In the same Figure, on the right, we present $PKiKP$ codas at 60° from heterogeneities at the core mantle boundary (source-side) assuming isotropic scattering. We can see that the effect of a larger scattering area is to produce a stronger $PKiKP$ arrival (amplitude at 0 lapse time). The reason is that, for small backazimuth anomalies (less than 5°), we are unable to cover the Fresnel zone for $PKiKP$ at the CMB. For larger backazimuth anomalies, the $PKiKP$ amplitude might grow a little, but the main effect is over the decaying rate of the coda in the first 50 s, that tends to flatten, while the rest of the coda has the same decaying rate as before. In our computations of topography we have used a backazimuth anomaly of 5°, which covers the whole Fresnel zone for $PKiKP$ at the core mantle boundary, source-side.

To account for this error, we assume that the propagation of the plane wave from the source to the scattering region is restricted to the x'-z plane, with the x-axis pointing from the source to the receiver. Letting the angle between x and x' be γ (see Figure 3.2), we can write the change of coordinates, after a rotation γ, as:

$$\begin{Bmatrix} x \\ y \\ z \end{Bmatrix} = \begin{bmatrix} \cos\gamma & -\sin\gamma & 0 \\ \sin\gamma & \cos\gamma & 0 \\ 0 & 0 & 1 \end{bmatrix} \begin{Bmatrix} x' \\ y' \\ z' \end{Bmatrix}. \tag{3.42}$$

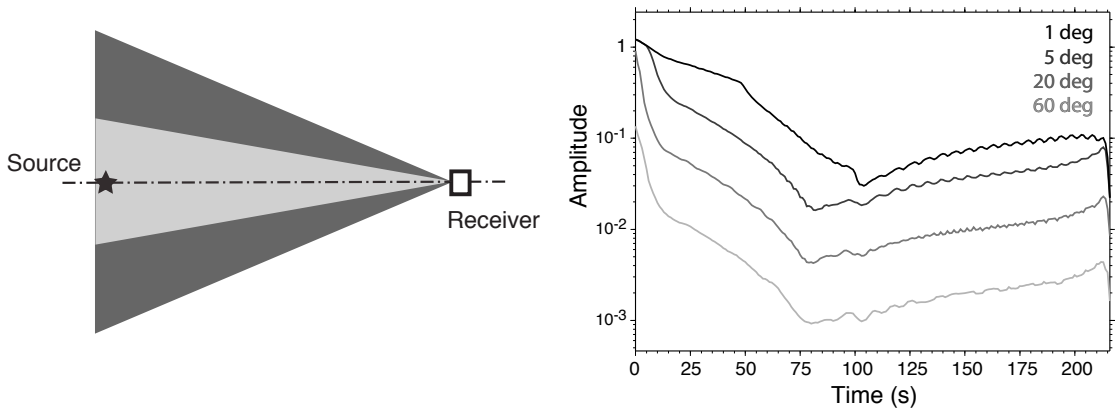

Figure 3.5: The relation between the size of the scattering region and the backazimuth anomalies is shown on the left, note that increasing one increases the other. The corresponding $PKiKP$ coda envelopes due to isotropic scattering in the CMB, source-side, are shown on the right. Each shade of gray represents a different backazimuth anomaly considered, as shown in the upper right corner. Here the amplitude and arrival time are shown with respect to the theoretical $PKiKP$.

The differentiation in this new coordinate system is given by

$$\frac{\partial f}{\partial x'} = \frac{\partial f}{\partial x}\cos\gamma - \frac{\partial f}{\partial y}\sin\gamma \quad \& \quad \frac{\partial f}{\partial y'} = \frac{\partial f}{\partial x}\sin\gamma + \frac{\partial f}{\partial y}\cos\gamma. \tag{3.43}$$

Hence, if the plane wave travels in a direction different from the great-circle-path, the derivatives needed to compute the apparent reflection coefficient will depend on the derivatives in x and y axis. Note that, if the scattering outside the great-circle path, we need to perform one change of coordinates, compute the reflection coefficient in this new coordinate system, and then project the result into the direction that links the location of the scatterer and the receiver. This last projection has been done for the above computations by considering the plane wave that connects the scattering region with the receiver (named post-scattering ray).

Another instance in which the change in backazimuth plays an important role is in the computation of the scattering angle (Θ). As we know, the change in ray parameter due to scattering will change the direction of propagation of the plane wave, because changes in the backazimuth will force the propagation of the plane wave outside the previous x'-z plane into the x-z, the scattering angle will change.

This can be computed by taking the dot product between two unit vectors with the changes in angle:

$$\cos\Theta = \Delta\hat{t} \cdot \hat{g} \tag{3.44}$$

where $\Delta\hat{t}$ represents the change in slowness and $\hat{g}$ the change in backazimuth. Note that

$$\Delta\hat{t} = \begin{Bmatrix} \sin\Delta\theta \\ 0 \\ \cos\Delta\theta \end{Bmatrix} \quad \& \quad \hat{g} = \begin{Bmatrix} \cos\gamma \\ \sin\gamma \\ 0 \end{Bmatrix} \tag{3.45}$$

with $\Delta\theta = \theta_2 - \theta_1$ and $\sin\theta_i = pr_i/\alpha_i$ the change in the propagation angle, and γ the change in backazimuth, as used before. Then

$$\cos\Theta = \sin\Delta\theta \cdot \cos\gamma = (\sin\theta_2\cos\theta_1 - \cos\theta_2\sin\theta_1)\cos\gamma \tag{3.46}$$

Source and Receiver Effects

Haddon and Cleary (1974) noted that several rays may arrive at the station with a wide range of azimuth and slownesses; hence, the observed trace was an "average" of all the phases incoming at a certain time. Seismic arrays enable us the identification of single waves arriving at the same time by means of the beamforming process. For a specific array, this process is completely described by the array response function (ARF) (*Rost and Thomas*, 2002). *Haddon and Cleary* (1974) included the effect of the ARF in the observations made by *Doornbos and Vlaar* (1973) and determined, based on the slowness content, the location of the heterogeneities at the CMB, either source- or receiver-side. We took into account the filtering effect produced by the ARF in our computations as follows.

Following *Rost and Thomas* (2002), we apply the array response function with respect to a main phase arrival. In the present study, we perform our computations with respect of the time, amplitude, and slowness of the direct $PKiKP$; therefore, we just have to look for the relative amplitude with respect to the central peak, for a particular 2D slowness vector. We work with the magnitude of the slowness

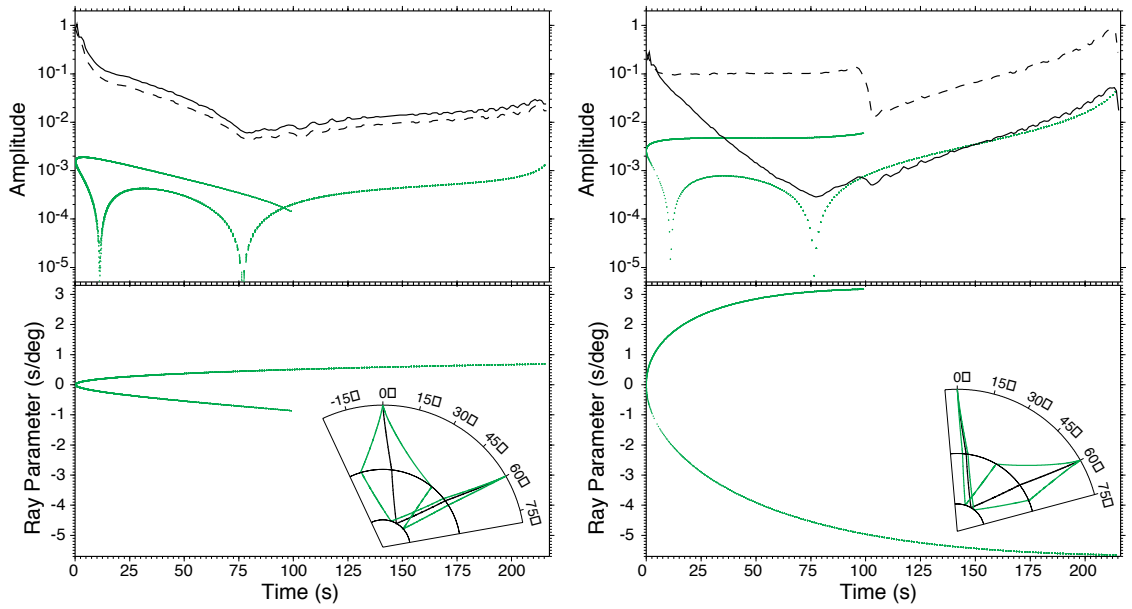

Figure 3.6: Effect of the array response function (ARF) on the $PKiKP$ coda envelope. These computations were made considering isotropic scattering at the core mantle boundary, on the source (left) and receiver-side (right). The bottom panels show the variation in time of the ray parameter, while the top panels show the value of the amplitude for each point in time. All values are relative to the $PKiKP$ arrival. The dashed lines represent the coda envelope without the application of the array response function and the solid lines after applying the ARF corresponding to ILAR (*Rost and Thomas*, 2002). The inserts in the lower panels present the ray paths of the direct $PKiKP$ (in solid black) and examples for the scattering waves, either $P.KiKP$ on the left and $PKiK.P$ on the right (in green). Note how most of the energy for the receiver-side scattering is filtered out by the ARF when beamforming at the theoretical $PKiKP$ slowness vector.

vector, and include the backazimuth information from the theoretical values plus the deviation in case of having scattering outside the great-circle path. In general, the sampling of the ARF is discrete, which will have an effect in the general shape of the envelope. An example is presented in Figure 3.6 for isotropic scattering at the core mantle boundary (see Figure caption for details).

We can see from Figure 3.6 that the amplitudes produced by scattering from heterogeneities at the core mantle boundary, before the application of the array response function (dashed lines) are quite similar for the source and receiver-side case; but this similarity is broken after considering the ARF, falling almost 3 orders of magnitude for the receiver-side case. This is due to the corresponding ray parameters: as

we can see, for the source-side case, the relative ray parameter ranges from -1.0 to 1.0 s/deg, while for the receiver-side case it goes from 3.2 to -5.6 s/deg. Then, after the application of the ARF, the resulting coda envelope is strongly reduced. Note that this effect is independent of the type of scattering (surface or volumetric) and the particular representation of the medium. Therefore, we discard the receiver-side of core mantle boundary as the possible location of the heterogeneities that produce $PKiKP$ coda.

Another important aspect that we investigated in this work was the effect of the focal mechanism on the shape of the coda. In general, the rays that compose the coda will have different ray parameters than that of the corresponding direct wave. Indeed, the longer the time after the body wave arrival, the larger the difference in ray parameter. In certain cases, this will have a large effect in the shape of the coda, and so should be accounted for when modeling specific data.

3.3 Results

In the present work, we focus our attention mainly on the shape of the coda; the determination of absolute values of the amplitudes is outside the scope of this study because it involves too many trade-offs that are not resolvable with the available observations. We generate $PKiKP$ coda envelopes from 4 regions: the lower mantle on the source-side, the core mantle boundary on the source-side, the inner core boundary, and within the inner core, as discussed in earlier sections. A key feature we search for is the coda that grows in time after the main phase arrival ("spindle-shaped" coda, as in *Vidale and Earle*, 2000; *Koper et al.*, 2004), as observed in the distance range from 50° to 70°. In our computations we consider a constant frequency of 1 Hz (similar to observations) and use a rms topography amplitude of 300 m, appropriate for the core mantle boundary (*Doornbos*, 1978; *Battaille and Flatté*, 1988; *Shearer et al.*, 1998) and the inner core boundary (*Forte and Peltier*, 1991).

3.3.1 Topography on the Core Mantle Boundary

Examples of $PKiKP$ coda produced by a single realization of topography at the core mantle boundary, on the source-side, are presented in Figure 3.7 (see Figure caption for details). From this Figure, we can see that the general shape of all the resulting codas (continuous lines in panels (b) and (c)) are very similar, but show distinct undulations related to the characteristic wavelength. However, the amplitude for each particular point (representing a particular ray that samples the scattering region) shows a clear increase in dispersion when using short wavelengths (upper panels in Figure 3.7(c)): compare how in panel (b) (isotropic scattering) the points form a clear line, but the top panels in (c) show a cloud of points. When using a large correlation lengths (such as 1500 km, shown in lower panels in (c)), the corresponding amplitudes for each ray tend to form one line that clearly resembles the shape of the topography at the core mantle boundary. This dispersion effect for short wavelengths is enhanced when using the Exponential autocorrelation function. Hence, the presence of energy in large wavenumber produces an increase in the dispersion of the particular amplitudes for each ray. To remove the dispersion effects of a single realization and get a representative shape of the coda, we compute several realizations for a particular model and characteristic wavelength and take the average over the whole ensemble.

Using trial-and-error we found that after 30 realizations we obtained a robust estimation of the average for a particular wavelength, based on the values of the standard deviation. Figure 3.8 presents the result for the Delta in power spectrum, considering a characteristic wavelength of 500 km (left) and 2000 km (right), the thin lines are a single realizations and the thick red lines represent the average (continuous line) plus/minus 1 standard deviation (dashed line). Note the difference between every single realization, especially when comparing different characteristic wavelengths; however, the resulting averages over the various ensembles prove to be quite similar. As mentioned earlier, the amplitude of the coda at zero time lapse is the amplitude of the direct $PKiKP$, that for this particular case takes into account the effect of focusing and defocusing due to the topography on the core mantle boundary. This

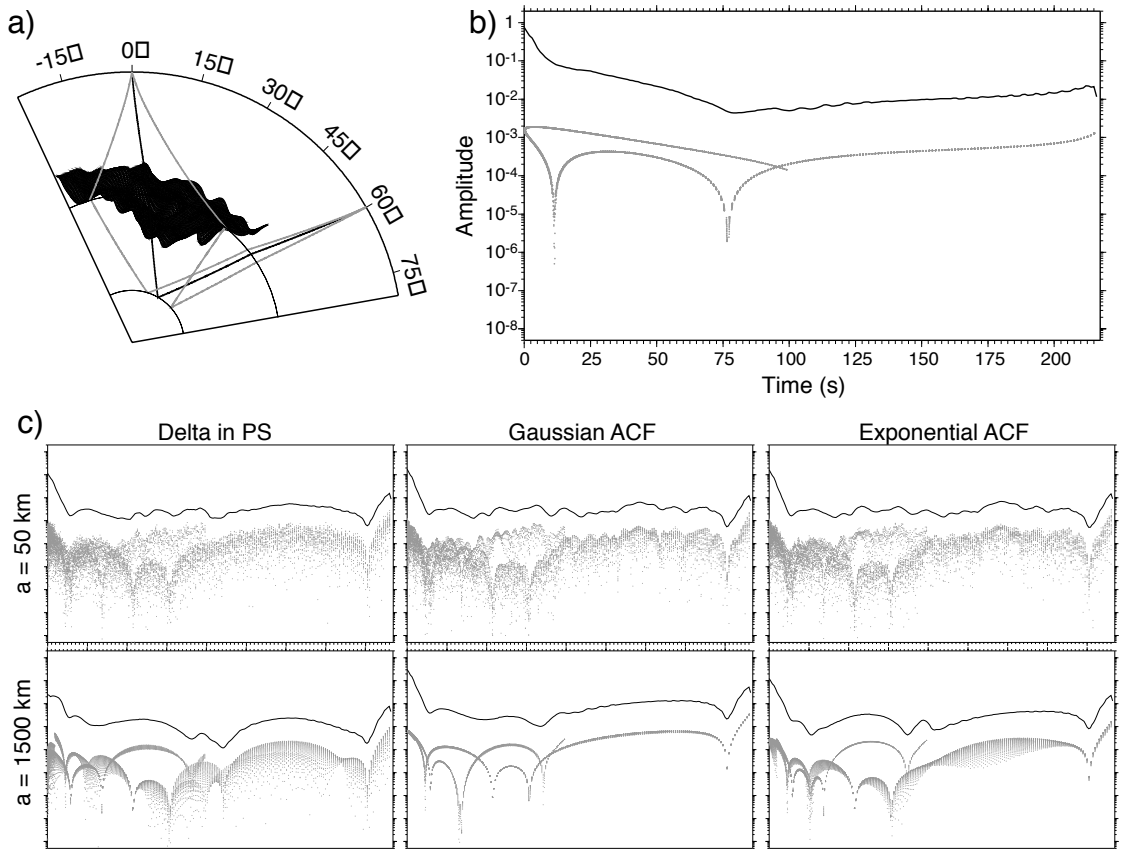

Figure 3.7: Example of $PKiKP$ coda generated due to scattering from topography at the core mantle boundary, on the source-side. We show: (a) a schematic representation of this case, including some ray paths, (b) the computations with isotropic scattering (time and amplitude are shown relative to $PKiKP$), and (c) the amplitude corresponding to different realizations: the first column was computed using a Delta in the power spectrum, the second has a Gaussian autocorrelation function, and the third an Exponential ACF; the characteristic wavelengths are 50 km for the upper and 1500 km for the lower panels. All the panels have the same scales in time and amplitude as (b), and were computed using the "small topography" approximation and a rms amplitude of the topography of 300 m.

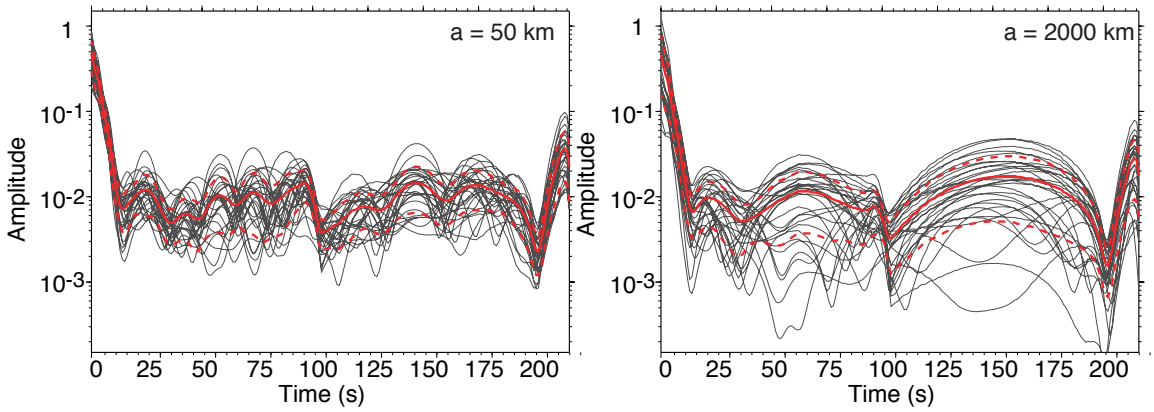

Figure 3.8: $PKiKP$ synthetic codas considering topography at the core mantle boundary, source-side, for an epicentral distance of 60°. We present 30 different realizations of topography (thin lines) using a Delta in power spectrum, with characteristic wavelengths of 500 km (left) and 2000 km (right); while in thick red lines we show the average (continuous) and the plus/minus 1 standard deviation (dashed).

value can vary up to one order of magnitude for long wavelengths (2000 km, shown in the right); a similar result was reported by *Kampfmann and Müller* (1989) on the study of PcP theoretical amplitudes. However, the average over the whole ensemble remains stable, showing a variation no larger than a factor of 2 for all the different models and wavelengths. We can conclude that focusing and defocusing produced by topography at the core mantle boundary produces a large variation on $PKiKP$ amplitudes, but after averaging over different observations, this effect is muted.

We found that all the resulting average codas, for different characteristics wavelengths, are almost the same, even when we consider different wavelengths and ACFs to describe the topography. In Figure 3.9 we present the results for epicentral distances of 60° (left) and 80° (right), for topography in the CMB, source-side. Results in continuous lines were computed using the "small topography" approximation (section 2.2.2); while the answer using the "long wavelengths" (section 2.2.1) is shown in dashed line. For the "long wavelengths" approximation, there is no substantial variation in the resulting answer when considering different model or characteristic wavelengths. In general we found a good agreement in the results of both methods.

From Figure 3.9 we can see that the coda produced by topography at the core mantle boundary generally decays after a clear $PKiKP$ arrival. For the 80° epicentral

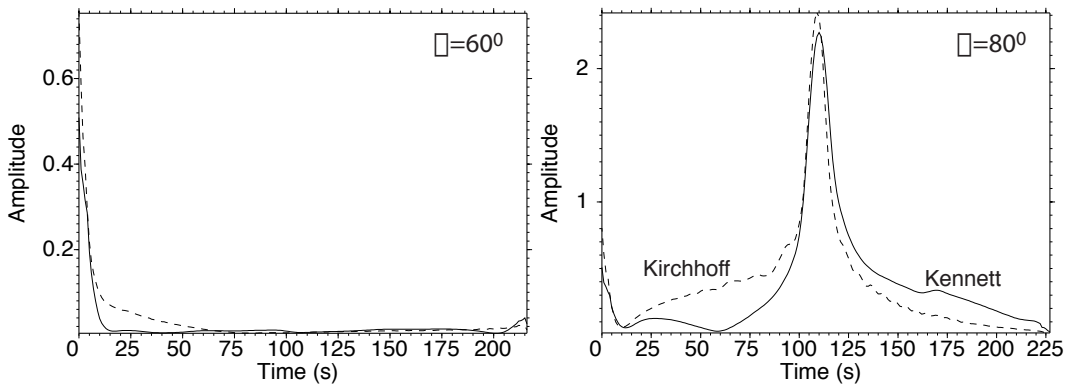

Figure 3.9: Average $PKiKP$ synthetic codas considering topography at the core mantle boundary, source-side, for the epicentral distance of 60° (left) and 80° (right). The continuous line were computed using the "small topography" approximation (Kennett method), while the dashed line considered the "long wavelengths" (Kirchhoff method).

distance, we see a strong secondary arrival ($\sim$ 100 s after the $PKiKP$) due to the increase of the reflection coefficient at the inner core boundary near post-critical distances. This increase in amplitude is significant (larger than a factor of 2); however, this is unlike previous observations.

3.3.2 Topography on the Inner Core Boundary

Figure 3.10 presents $PKiKP$ coda envelopes from 30 different realizations of topography at the inner core boundary (thin lines). Here, we used Delta in power spectrum, considering a characteristic wavelength of 500 km (left) and 2000 km (right), to represent the medium. Thick red lines represent the average (continuous line) plus/minus 1 standard deviation (dashed line). Again, the average of several realizations is quite similar even when considering different models (Gaussian autocorrelation function, Exponential ACF, and Delta in power spectrum) and different characteristic wavelengths. The final results obtained for this case are shown in Figure 3.11, for epicentral distances of 60° (left) and 80° (right). In this case, the result obtained using Kirchhoff method ("long wavelength" approximation) is closer to the one from Kennett ("small amplitude" approximation). The resulting $PKiKP$ codas are quite distinct compared to the case of CMB topography: in general the amplitude

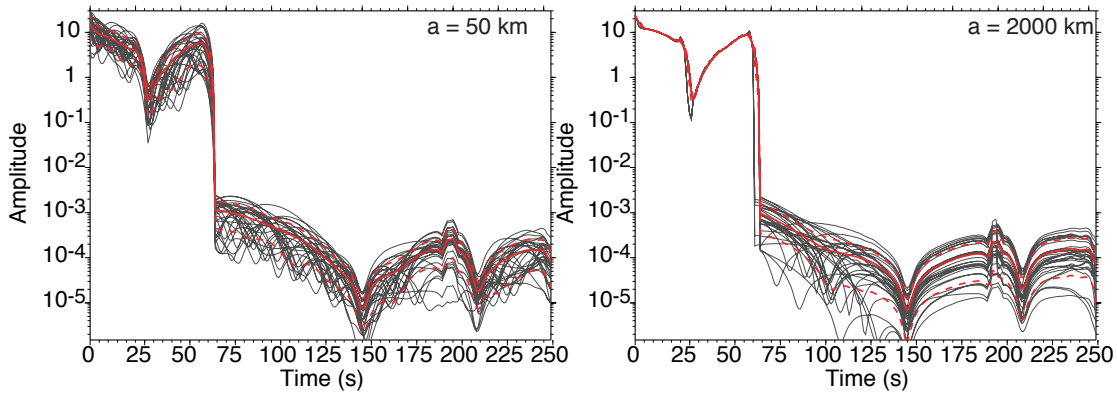

Figure 3.10: $PKiKP$ synthetic codas considering topography at the inner core boundary for an epicentral distance of 60°. We present 30 different realizations of topography (thin lines) using a Delta in power spectrum, with characteristic wavelengths of 500 km (left) and 2000 km (right); while in thick red lines we show the average (continuous) and the plus/minus 1 standard deviation (dashed).

remains stable for 75 s (at 60°) or 30 s (at 80°), to strongly drop (almost 4 orders of magnitude) in a very short period of time. This drop is caused by the loss in amplitude from the $P.KP_{CD}$ branch to the $P.KP_{DF}$ branch, due to the strong attenuation inside the inner core. However, there is no gradual growth in the $PKiKP$ coda envelope, as seen in the data. We investigated other epicentral distances from 50° to 90° with similar results.

3.3.3 Volumetric Scattering in the Lowermost Mantle

In Figure 3.12 we present the resulting $PKiKP$ coda envelopes caused by volumetric scattering in the lower mantle, near the core mantle boundary, at epicentral distances of 60° and 80°. For the computation we used several layers with a constant thickness of 50 km, up to 350 km above the CMB (radius of 3780 km). Smaller thickness and a larger number of layers (resulting in the same total thickness) does not significantly affect the results. For the epicentral distance of 60° we obtain a normal decaying coda, that lasts up to 125 s, and then we see a strong growth. This growing behavior can also be seen in the results for 80°, in a way that resembles more a later phase arrival than a growing coda. This growing is different from the gradual, smooth growth seen in the data; especially that its beginning is delayed with respect to the

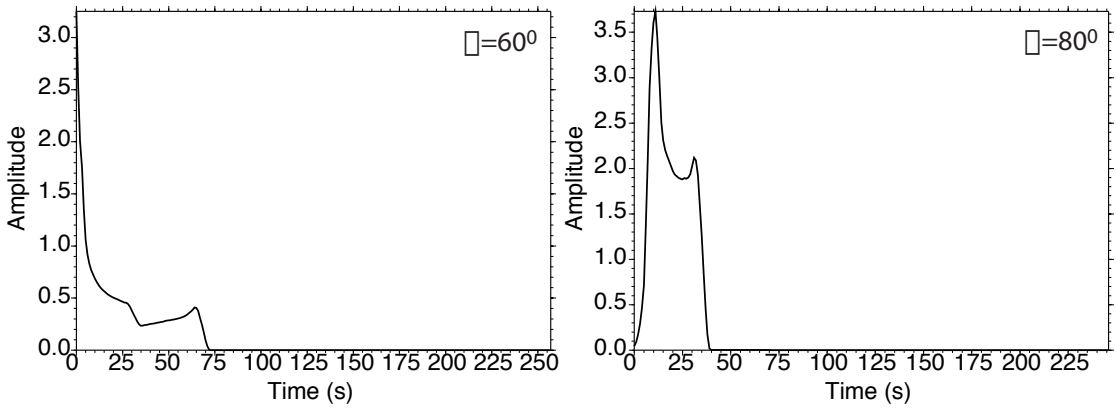

Figure 3.11: Average $PKiKP$ synthetic coda envelopes considering topography at the inner core boundary, for the epicentral distances of 60° (left) and 80° (right). All values are presented relative to $PKiKP$.

direct $PKiKP$ arrival, being a function of the epicentral distance. Note that the duration of the secondary arrival is directly proportional to the total volume of the scattering region at the core mantle boundary; while the amplitude is a function not only of this parameter, but also of the rms P-wave velocity contrast and characteristic scale length of the heterogeneities. The dashed thick lines presents the results considering the model proposed by *Koper and Dombrovskaya* (2005) for the inner core boundary. The main difference is that the predicted $PKiKP$ amplitude (amplitude at zero lapse time), is larger (compared to the later arrival) for the second model, specially at smaller epicentral distances.

3.3.4 Volumetric Scattering in the Inner Core

Figure 3.13 presents the results of volumetric scattering inside the inner core, for epicentral distances of 60° (left) and 80° (right). These were computed using layers within the inner core (each one with a thickness of 50 km adding up to 400 km below the ICB) all with an Exponential autocorrelation function, with a correlation length of 10 km. We see that the effect of the final layer is very small, meaning that our resolution is limited to this depth (radius $\sim$ 822 km), similar to the one reported by *Vidale and Earle* (2000). In general, these codas grow for $\sim$ 50 s (at 60°) or $\sim$ 25 s (at 80°) and then smoothly decay for 50 s, much like previous observations (*Vidale*

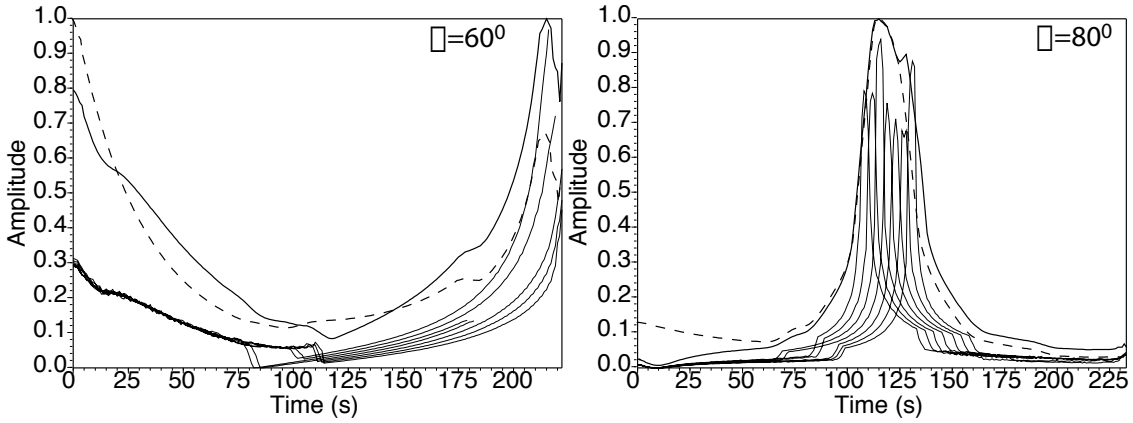

Figure 3.12: Synthetic envelopes for $PKiKP$ from volumetric heterogeneities located at the lower mantle, source-side, for epicentral distances of 60° (left) and 80° (right). The volumetric scattering was computed considering layers of 50 km thickness up to 350 km above the CMB; the thin lines are the contribution for each layer while the thick line is the sum (in power). We have used an Exponential autocorrelation function with a correlation length of 8 km, as proposed for this region by *Shearer et al.* (1998). The dashed thick lines represent the results with the same parameters, but using the ICB model proposed by *Koper and Dombrovskaya* (2005). The amplitude has been normalized to the maximum and the time is shown relative to $PKiKP$.

and Earle, 2000; *Koper et al.*, 2004). We also tested the effect the model for the inner core boundary proposed by *Koper and Dombrovskaya* (2005) (shown in thick dash lines in the same Figure) without a significant effect in the resulting coda envelopes.

Figure 3.14 presents $PKiKP$ coda envelopes considering volumetric scattering inside the inner core for an epicentral distances of 60°. We described the medium using a Gaussian (dashed lines) and Exponential autocorrelation functions (continuous lines), while the color represent different characteristic wavelengths used. Note that, independent of the model used to describe the heterogeneities (Exponential or Gaussian) for a larger correlation length, the resulting coda envelope has a larger amplitude. Additionally, if we fix the correlation length, the Gaussian ACF produces a larger amplitude than the Exponential. Recall that, for volumetric scattering, there is a strong trade-off between the volume, rms difference (in P-wave velocity or P-wave impedance contrast, or both) between the medium and the heterogeneities, and the characteristic wavelength; hence, considering the same volume and characteristic wavelength, the Gaussian ACF requires a smaller rms compared to the Exponen-

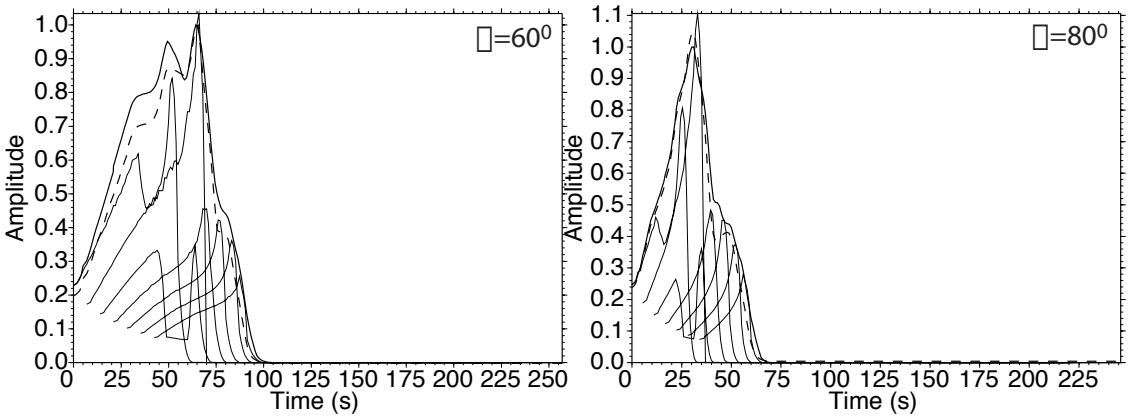

Figure 3.13: Synthetic envelopes for $PKiKP$ from volumetric heterogeneities located within the inner core for epicentral distances of 60° (left) and 80° (right). The volumetric scattering was computed considering layers of 50 km thickness down to 400 km below the inner core boundary; the thin lines are the contribution for each layer while the thick line is the sum (in power). We have used a Exponential autocorrelation function with a correlation length of 10 km. The thick dashed lines represent the results with the same parameters, but using the ICB model proposed by *Koper and Dombrovskaya* (2005). The amplitude has been normalized to the maximum and the time is shown relative to $PKiKP$.

tial, as reported by *Shearer et al.* (1998). On the bottom panel we have only used the Exponential autocorrelation function, but 2 characteristic wavelengths, and have normalized each curve to its corresponding maximum. Note the strong effect of the characteristic length in the rise from zero lapse time: since both curves have been normalized, they both reach to 1.0, but the coda envelope with larger characteristic length (10 km) starts from 0.23 while the one with smaller characteristic length (1 km) starts from 0.45; this feature may enable the determination of the scale length of heterogeneities in the inner core form $PKiKP$ coda envelopes. On the other hand, we do not find any effect on the growing time (50 s) and duration of the coda (100 s). The effect of different correlation lengths in the Gaussian ACF on rise, growing time, and duration of the coda was negligible.

We found that the growing time of the $PKiKP$ coda envelopes is a smooth function of the epicentral distance (Figure 3.15). Here we can see that for larger epicentral distances the growing time decreases, being only 20 s at 90°; this could lead to confusing a "spindle"-shaped coda with a regular body wave arrival. For example,

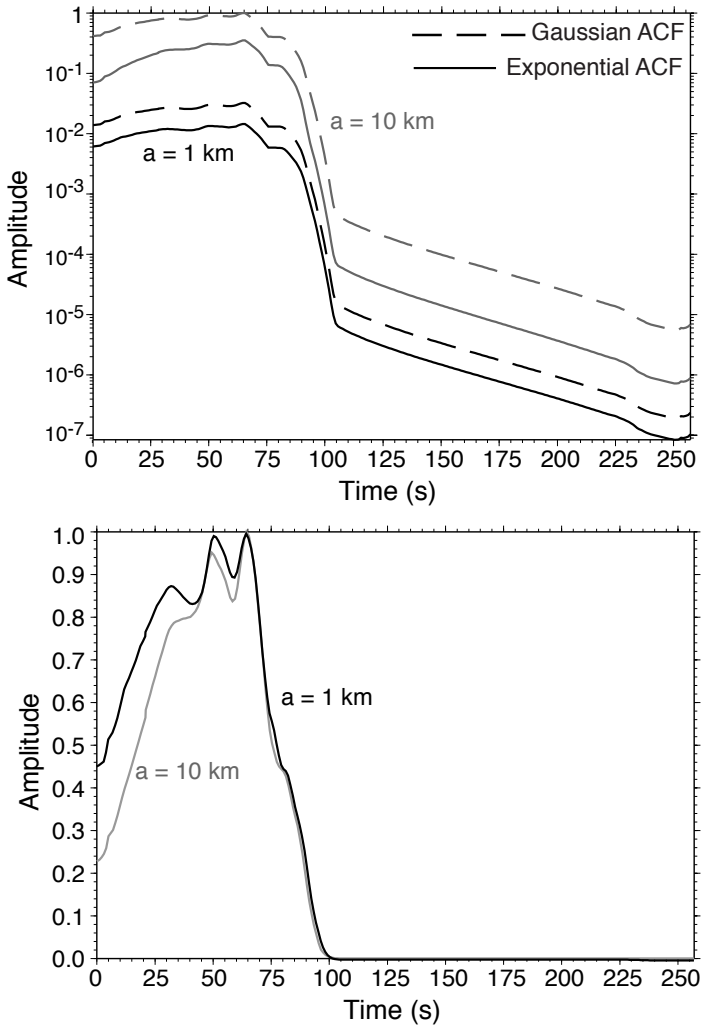

Figure 3.14: Synthetic envelopes for $PKiKP$ from volumetric heterogeneities located inside the inner core for an epicentral distance of 60°. Top panel shows the results considering a Gaussian autocorrelation function (dashed lines) and an Exponential ACF (continuous lines) with 2 different correlation lengths: 1 km (black) and 10 km (gray). On the bottom panel we have used the Exponential ACF for volumetric heterogeneities inside the inner core, computed using different layer (50 km thick) up to 400 km below the ICB. Again, the color represents different characteristic wavelengths: 1 km in black and 10 km in gray. The amplitude has been normalized to the maximum and the time is shown relative to $PKiKP$.

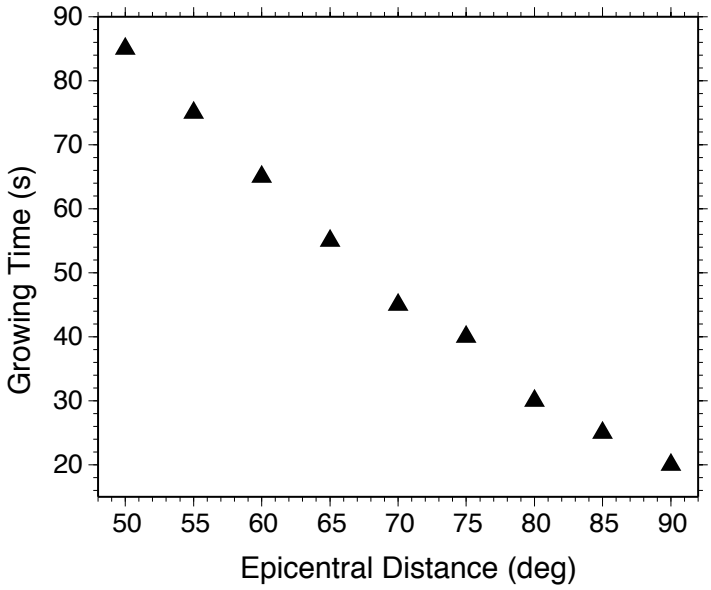

Figure 3.15: Variation of the growing time of "spindle" shaped $PKiKP$ coda envelopes with respect to the epicentral distance. Here we have considered volumetric scattering inside the inner core, from the inner core boundary down to a radius of 822 km, using shells with thickness of 50 km.

in case of an earthquake with a long or complicated source time function, the growing part in the coda would be mixed inside the source time function (for an earthquake with magnitude $Mw \approx 7.0$, the source time function is ~ 20 s). Note that these results agree with the observations made by *Vidale and Earle* (2000): at a distance range of $58^\circ - 73^\circ$ they found a growing time of 50 s in actual observations, while we get a mean value of 55 s. Even more, observations made by *Koper et al.* (2004) found a shorter growing time for slightly larger epicentral distances, as predicted here.

3.4 Conclusions

In the present work we calculated synthetic $PKiKP$ coda envelopes in the distance range of $50^\circ - 90^\circ$ to determine if an initially growing coda could be created by various types of deep Earth heterogeneity. Using classical, single-scattering theory we examined the possibility of $PKiKP$ coda wave generation from four possibilities: the lower mantle on the source-side, the core mantle boundary on the source-side,

the inner core boundary, and within the inner core. From all these, only the last was able to produce the observed gradual growing or "spindle"-shaped coda. Topography at the ICB can generate a coda with an initial increase in amplitude, but only by considering different layers within the inner core is that we can have a smooth growth and decay that matches the observations. Our previous work (*Leyton et al.*, 2005) precludes the possibility of having layering inside the inner core, each one with topography. Even more, we found that placing heterogeneities in the inner core gives a stronger side-scattering compared to the lower mantle, due to the differences in rheology. Therefore, our results support the presence of small-scale heterogeneities in the upper 350 km of the inner core, with scale lengths ranging from 1 to 10 km.

As has been shown, volumetric scattering has a strong trade-off between the model used to describe the medium (autocorrelation function), the characteristic wavelength, total volume, and P-wave impedance contrast of the scatterers precluding the determination of useful properties of the heterogeneities inside the inner core. However, the shape of the $PKiKP$ coda can give some insights, showing a stronger growth when considering smaller wavelengths compared to the case with only large wavelengths; hence, by studying the relative growth of the coda from the $PKiKP$ arrival to its maximum, we could estimate the amount of energy in for the large wavenumbers. The growing time and total duration of the coda depends only on the epicentral distance, and not on the wavelengths of the heterogeneities or the models used to describe them. An important limitation of this study is the assumption of single scattering; however, these techniques are valid for the hypotheses tested here: smooth, small amplitude topography (*Kennett*, 1972; *Frazer and Sen*, 1985; *Doornbos*, 1988) and volumetric heterogeneities with a few percent rms contrast (*Wu and Aki*, 1985a,b; *Margerin and Nolet*, 2003a). The next step is to explore the effect of multiple scattering with methods such as radiative transfer theory (*Margerin and Nolet*, 2003a,b), the phonon method (*Shearer and Earle*, 2005), or hybrid methods combining generalized ray theory and finite differences (*Wen and Helmberger*, 1998b).

Finally, we have found that placing reasonable topography at the core mantle boundary can affect the amplitude of the direct $PKiKP$ wave up to 1 order of

magnitude due to effects of focusing and defocusing, similar to the results obtained by *Kampfmann and Müller* (1989) for PcP. Such variation in $PKiKP$ amplitudes has been observed previously, and taken to imply a complex inner core boundary (*Koper et al.*, 2004; *Krasnoshcenkov et al.*, 2005). We believe that there is complexity in the ICB (*Stroujkova and Cormier*, 2004), but not all of the anomaly observed in the $PKiKP$ amplitudes can be assigned to this phenomenon.

Chapter 4

Using $PKiKP$ Coda to Determine Inner Core Structure. 2. Determination of Q_C

It is thought that the Earth's inner core is mainly composed of iron, with only a few percent of light elements. Despite this uniform composition, several authors have reported evidence of scattered seismic energy coming from the inner core (IC). This implies that the IC has lateral variations in structure or composition with a scale length from one to tens of kilometers. These seismic scatterers could be caused by changes in crystal grain size, variations in the orientation of anisotropy, or the presence of partial melt and/or impurities. This work pursues the characterization of inner core scattering (ICS) using a global data set of high frequency $PKiKP$ waveforms recorded at short-period, small-aperture seismic arrays. We apply a methodology used in the study of heterogeneities in the crust and upper mantle that consists of curve fitting of the observed scattered energy with a standard model, along with a stripping technique to isolate the $PKiKP$ coda from the rest (e.g. P, PcP, and PP codas). From the observed $PKiKP$ codas we found an average $Q_C \sim 500$ for the inner core, reflecting a scattering attenuation at least comparable to the intrinsic attenuation. We found a geographical dependence in the observations of $PKiKP$ coda, with most of them coming from the Pacific Ocean and Asia, and relatively few observations coming from the Atlantic Ocean. The simplest explanation is that the ICS has a quasi-hemispherical variation, similar to other properties such as P wave velocity jump at the inner core boundary, attenuation in the upper IC, strength of anisotropy and/or thickness of an overlaying isotropic layer. This phenomenon is probably related to the solidification texturing of iron crystals, showing hemispherical differences in the growth of the inner core.

4.1 Introduction

The Earth's inner core is mainly composed of iron with a small percentage of lighter elements (e.g. *Bergman*, 2003; *Steile-Neumann et al.*, 2003), yet its detailed structure is not well defined (*Song*, 2003). Despite its rather uniform composition, lateral heterogeneities inside the inner core have been reported at a variety of scale-lengths, from global scales (*Kaneshima*, 1996; *Tanaka and Hamaguchi*, 1997; *Niu and Wen*, 2001; *Wen and Niu*, 2002) to regional scales (*Creager*, 1997; *Bréger et al.*, 1999; *Niu and Wen*, 2001; *Cormier and Li*, 2002) to local scales of a few or tens of kilometers (*Vidale and Earle*, 2000; *Koper et al.*, 2004; *Poupinet and Kennett*, 2004). There is growing evidence of a dramatic change between a quasi-western hemisphere and a quasi-eastern hemisphere, usually defined from 40° E to 180° E (*Niu and Wen*, 2001; *Wen and Niu*, 2002; *Cao and Romanowicz*, 2004), although there has been some variation (*Creager*, 1999; *Oreshin and Vinnik*, 2004). Differences between the two quasi-hemispheres have been reported in the strength of anisotropy (*Tanaka and Hamaguchi*, 1997; *Creager*, 1999), the thickness of an isotropic layer at the top of the inner core (*Tanaka and Hamaguchi*, 1997; *Song and Helmberger*, 1998; *Creager*, 1999; *Garcia and Souriau*, 2000; *Niu and Wen*, 2002), the jump in velocity at the inner core boundary (*Niu and Wen*, 2001; *Wen and Niu*, 2002; *Garcia*, 2002), and in attenuation (*Wen and Niu*, 2002; *Cao and Romanowicz*, 2004; *Oreshin and Vinnik*, 2004). It has been suggested that the hemispherical difference may be related to a differential cooling process between the "eastern" and "western" hemispheres (*Wen and Niu*, 2002) of the fluid outer core, driven by a thermal coupling with the heterogeneous lower mantle (*Sumita and Olson*, 1999).

At the smallest scale-lengths, evidence for lateral heterogeneity in the inner core comes mainly from scattered energy appearing in the coda of body waves (*PKiKP*) reflected from the inner core boundary (*Vidale and Earle*, 2000; *Koper et al.*, 2004; *Poupinet and Kennett*, 2004; *Vidale and Earle*, 2005). This inner core scattering (ICS) has been related to crystal grain size and growth (*Cormier et al.*, 1998; *Bergman*, 2003), variations in the orientation of anisotropy and attenuation (*Cormier*

and Li, 2002), the presence of partial melts (*Singh et al.*, 2000) and/or impurities, such as sulfur (*Jephcoat and Olson*, 1987) or silicon (*Lin et al.*, 2002). Recent work has shown that the $PKiKP$ coda does not come from a preferred depth inside the inner core (*Leyton et al.*, 2005) and that a large fraction of the $PKiKP$ coda waves can indeed be attributed to volumetric heterogeneities inside the inner core, as opposed to scattering from irregularities in the inner core boundary and/or the core mantle boundary, or volumetric scattering in the lower mantle (Chapter 3). The detection of $PKiKP$ coda at precritical distances has been rare and, up to this point, little work has been done to quantify it or map out any geographical variation.

The work presented here investigates the largest data set ever assembled of ICS observations, focusing on the outermost inner core (near or at the ICB) where the presence of small-scale scatterers has been detected. We pursue the quantification of regional variability of $PKiKP$ coda in terms of the quality factor Q_C, as previously done in studies of heterogeneities in the crust (for reviews, see *Sato and Fehler*, 1998; *Mitchell*, 1995). This dimensionless quantity is inversely proportional to the decay rate of the coda energy in time, and several studies have successfully related crustal Q_C observations with the scattering strength (Q_S) and anelastic attenuation (Q_I) in a particular region (e.g. *Aki and Chouet*, 1975; *Singh and Herrmann*, 1983; *Fehler et al.*, 1988; *Dainty*, 1990). In the crust, low values of Q_C (~ 100) are associated with tectonically active regions (*Singh and Herrmann*, 1983; *Jin and Aki*, 1988; *Mitchell*, 1995), and in the continental US, Q_C is the largest ($\sim$ 1000 - 1300) where rocks are the oldest (*Singh and Herrmann*, 1983). Large Q_C values were also reported near active volcanoes (*Matsumoto and Hasegawa*, 1989), and even more, changes in Q_C before and after the Mt. St. Helens volcanic eruption have been observed and related to inflation-induced crack density changes (*Fehler et al.*, 1988).

Likewise, a detailed study of Q_C from $PKiKP$ coda could lead us to improve the current knowledge of the structure in the inner core, especially at the smaller scales. A particularly important aspect of this study is to identify, isolate, and properly model the $PKiKP$ coda energy, which is in general much smaller in amplitude than codas of crustal phases such as Lg, and is influenced by the codas of earlier arriving

mantle waves such as P, PcP, and PP. Therefore, we use array-based techniques to identify and amplify each phase, and, along with a "stripping" technique, we isolate the $PKiKP$ coda energy from the rest of the seismogram. Using a least squares approach, we find appropriate models to fit the data and obtain robust estimates of $PKiKP$ Q_C for a variety of geographical patches and source-receiver distances.

4.2 Data

Our data set comes from the International Monitoring System (IMS) seismic archive, in which the waveforms could previously be retrieved through an **autodrm** managed by the prototype International Data Center (pIDC). The data corresponds to small-aperture arrays of short-period, vertical component seismometers located throughout the world (boxes in Figure 4.1). This enables us to use standard array techniques, a key point in the observations made here. We selected a set of earthquakes located at an epicentral distance from 50° to 90° from an IMS array station. At this distance range, the travel paths of mantle phases (such as P, PcP, and PP) differ significantly from the path of $PKiKP$, precluding the use of these phases as proxies of the effect of scattering in the mantle (see Figure 4.1, insert). On the other hand, at this distance range the reflection coefficient at the inner core boundary tends to zero, reducing the influence of crustal and mantle scattering on $PKiKP$ coda (*Koper et al.*, 2004).

The selected events come from a data set of 1,393 source-array combinations, in which the only criteria was to have a moment magnitude over 5.6, disregarding the depth and focal mechanism constraints adopted in a previous study (*Koper et al.*, 2004). The rejection of traces was made solely on the signal to noise ratio and quality of the data. We divided our data set into three categories (each category being a subset of the previous one):

1. Good signal-to-noise ratio: after visual inspection and elimination of noisy traces, the resulting set is composed by high signal-to-noise ratio for mantle phases.

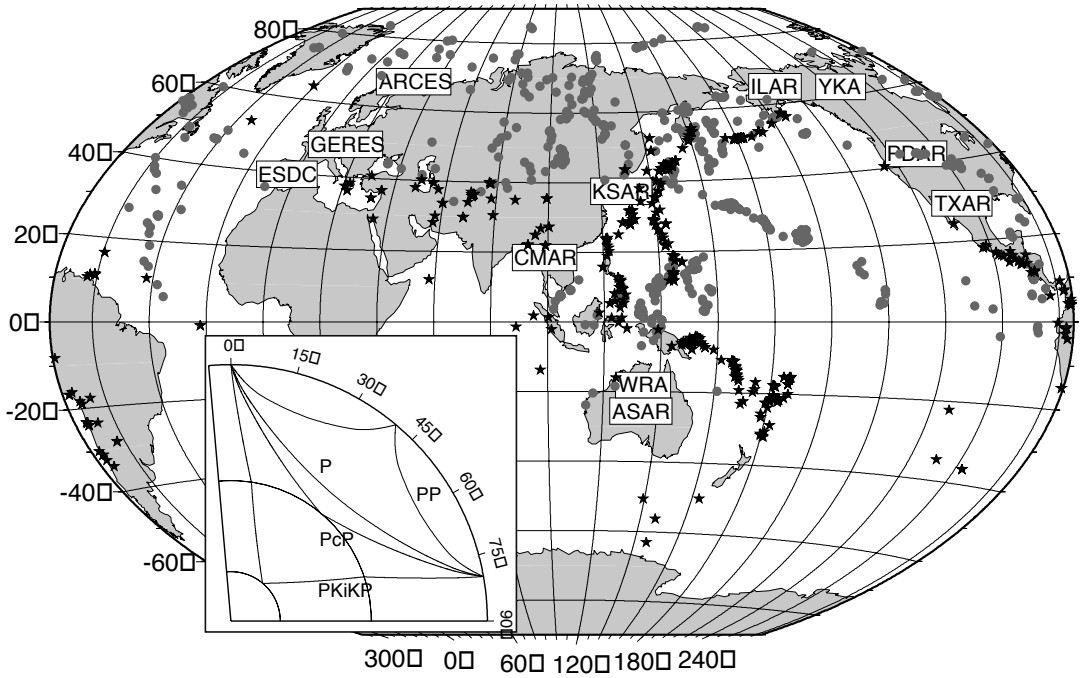

Figure 4.1: Location of IMS arrays (boxes) and events (black stars) in category 2 (clear identification of $PKiKP$) used in this study; the bounce points at the inner core boundary are shown with grey circles. All of arrays are short-period, vertical component seismometers. The events occurred during the IMS "open" period of 1/1/1995 through 2/20/2000. The insert shows the travel path of the main phases at an epicentral distance of 80° used in this study: P, PcP, PP, and $PKiKP$.

2. Clear identification of $PKiKP$, considering arrival time and slowness observations in the five frequency bands defined (see Methodology section).

3. Clear identification of coda energy arriving at the appropriate time, slowness, and back-azimuth expected for $PKiKP$. The coda energy generally lasts from 100 s to more than 200 s and stands out over the preceding codas after beamforming at the theoretical $PKiKP$ slowness.

Table 4.1 has the number of observations made in each category, as well as some properties of each of the arrays used. In Figure 4.1 we show the location of those events that fall into category 2 (stars), and their corresponding piercing point in the inner core (gray circles). Note that our sampling is mostly restricted to the northern hemisphere where 9 out of the 11 arrays are located. In Figure 4.2 we present the ratio of those events that fall into category 3 over those that fall into category 2, and

we can see that the western Pacific presents more $PKiKP$ observations and, from those observations, a larger percentage have observable $PKiKP$ coda. We believe that this is related to the structure inside the Earth, almost certainly in the inner core, and not due to the properties of individual arrays, as discussed in detail in the Results section.

Table 4.1: IMS stations used and some properties

Array Station	Lat °N	Lon °E	Number of Elements	Aperture[a] km	Aspect Ratio[b]	Events Cat 1	Events Cat 2	Events Cat 3
ARCES	69.535	25.506	23	3.7	0.0224	157	107	19
ASAR	-23.665	133.951	19	9.8	0.0108	99	41	6
CMAR	18.420	98.959	18	11.0	0.0060	157	34	16
ESDC	39.671	-3.946	19	9.4	0.0064	108	32	2
GERES	48.837	13.702	25	4.1	0.0482	75	9	1
ILAR	64.772	-146.886	19	10.5	0.0345	261	114	40
KSAR	37.447	127.894	19	10.8	0.0274	73	27	7
PDAR	42.777	-109.583	13	3.4	0.0450	139	39	2
TXAR	29.334	-103.667	9	4.5	0.0192	98	15	3
WRA	-19.767	134.393	20	23.9	0.0017	74	16	5
YKA	62.606	-114.605	18	24.2	0.0020	152	47	9

[a] We use the definition from *Koper et al.* (2003) as the diameter of the circle that has the same area as the smallest rectangle that includes all the elements.
[b] We use the definition from *Koper et al.* (2003) as the change in elevation between the highest and lowest elements, divided by the aperture.

After selection, the data set in category 3 consists of 110 events (Table 4.1), of which 56% are deeper than 50 km, 41% have a radiation pattern coefficient larger that 0.7 for $PKiKP$, 86% have an epicentral distance larger that 70°, and only 13% have magnitude M_W larger than 7.0. The locations of these events are shown later on (Figure 4.9, page 83), along with the resulting Q_C values. Note that we imposed less constraints in the selection of the data, leading to twice as many $PKiKP$ coda observations as previously reported in *Koper et al.* (2004). However, there are cases where events selected by *Koper et al.* (2004) were not used in this study, due to the fact that we required that the energy of the $PKiKP$ beam at the appropriate time,

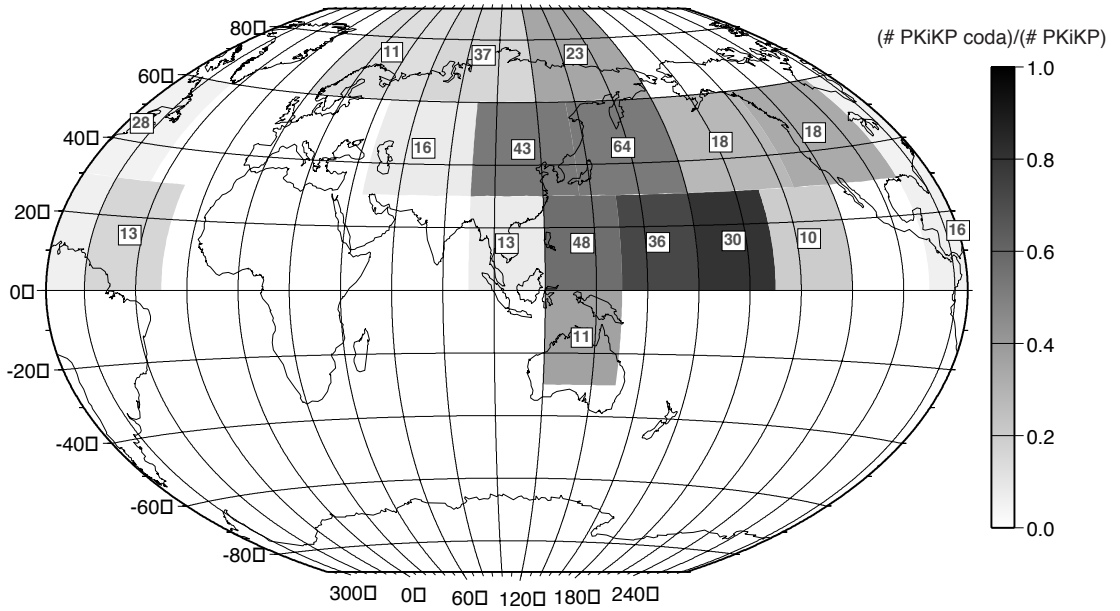

Figure 4.2: Ratio of events in category 3 (with $PKiKP$ coda) over events in category 2 (only $PKiKP$ itself) shown in gray scale. Here, darker regions represent places were most of the observed $PKiKP$ phases are accompanied by a coda; while lighter regions, represent places with positive observation of $PKiKP$ but not coda. The squares show the total number of observations in category 2 found. We defined a threshold of 10 events to plot the squares. The squares were defined trying to keep a constant area; hence, at larger latitudes, the longitude distances are larger.

should stand out over the rest of the seismogram, enabling it to be modeled.

4.3 Methodology

For each category 3 event we inspected the data and removed the traces with small signal-to-noise ratio, glitches, and lack of data. Then, we filtered them using a 3-pole Butterworth bandpass filter, with one octave width, centered on either 1, 2, 3, 4, or 5 Hz, as commonly done in the determination of Q_C (*Tsujiura*, 1978). The corresponding corner frequencies are 0.67-1.33 Hz, 1.33-2.67 Hz, 2.0-4.0 Hz, 2.67-5.33, and 3.33-6.67 Hz, respectively. These bands are limited by the instrument response (near 1 s), the Nyquist frequency (given by the sampling used), and the noise coherency for the arrays used here (see Figure 4.3). We computed the coherency of the seismic noise between the different stations for each array using the same procedure as the data analysis (see below). Depending on the properties of the site in which each seismic arrays is located, the noise will be coherent at different frequencies and due to the fact that we are using waves with very low signal-to-noise ratio, coherent noise will lead to difficulties in the analysis of the results.

After filtering, we performed a sliding window slowness analysis from 100 s before the first arrival (either P or $P + PcP$) until 600 s later, usually from 500 s to 1200 s after the origin time. We used a time window of 1 s, with a 50% overlap, and computed the 2D slowness vector with the highest beam power using a grid search over the two horizontal components of the slowness vector. We defined beam power as the root mean square amplitude over the selected time window. In this time window, we also computed the coherency of the signal with methods previously developed (*Schimmel and Paulssen*, 1997) and successfully used in these kind of studies (*Koper et al.*, 2004). An example of this procedure is shown in Figure 4.4, where we present the raw traces of an event (panel (a)) and the sliding window analysis for 2 Hz (panel (b) to (e)) and 5 Hz (panels (f) to (i)).

This slowness analysis is useful in defining time windows in which the seismic energy can be considered as mostly from a single phase and its corresponding coda.

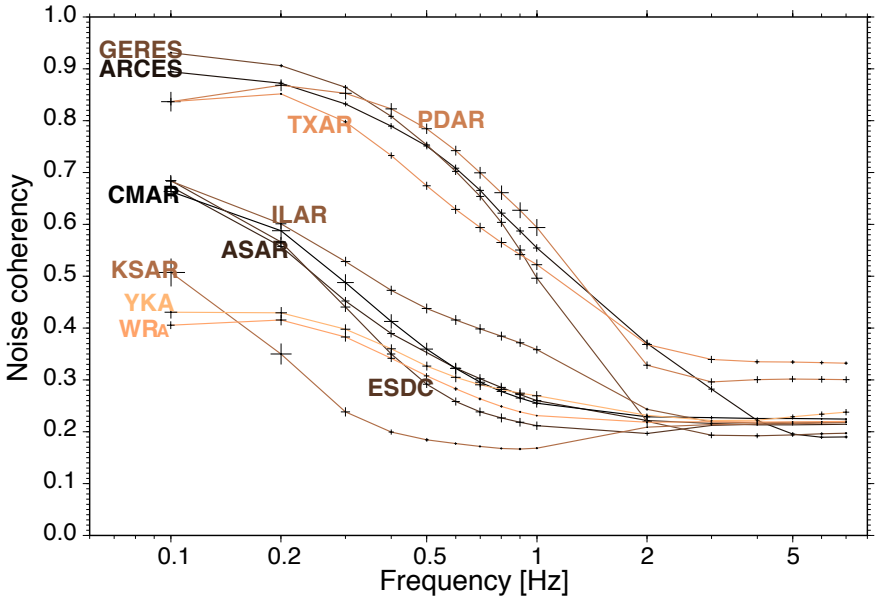

Figure 4.3: Noise coherency computed for all the arrays used in this study. We computed the coherency for several time windows at different time during the "open" period (1/1/1995 through 2/20/2000) and then averaged to get a robust estimation. The crosses represent the double standard deviation for each value. The coherency is computed using the the instantaneous phase (*Schimmel and Paulssen*, 1997) as done in similar studies (*Koper et al.*, 2004).

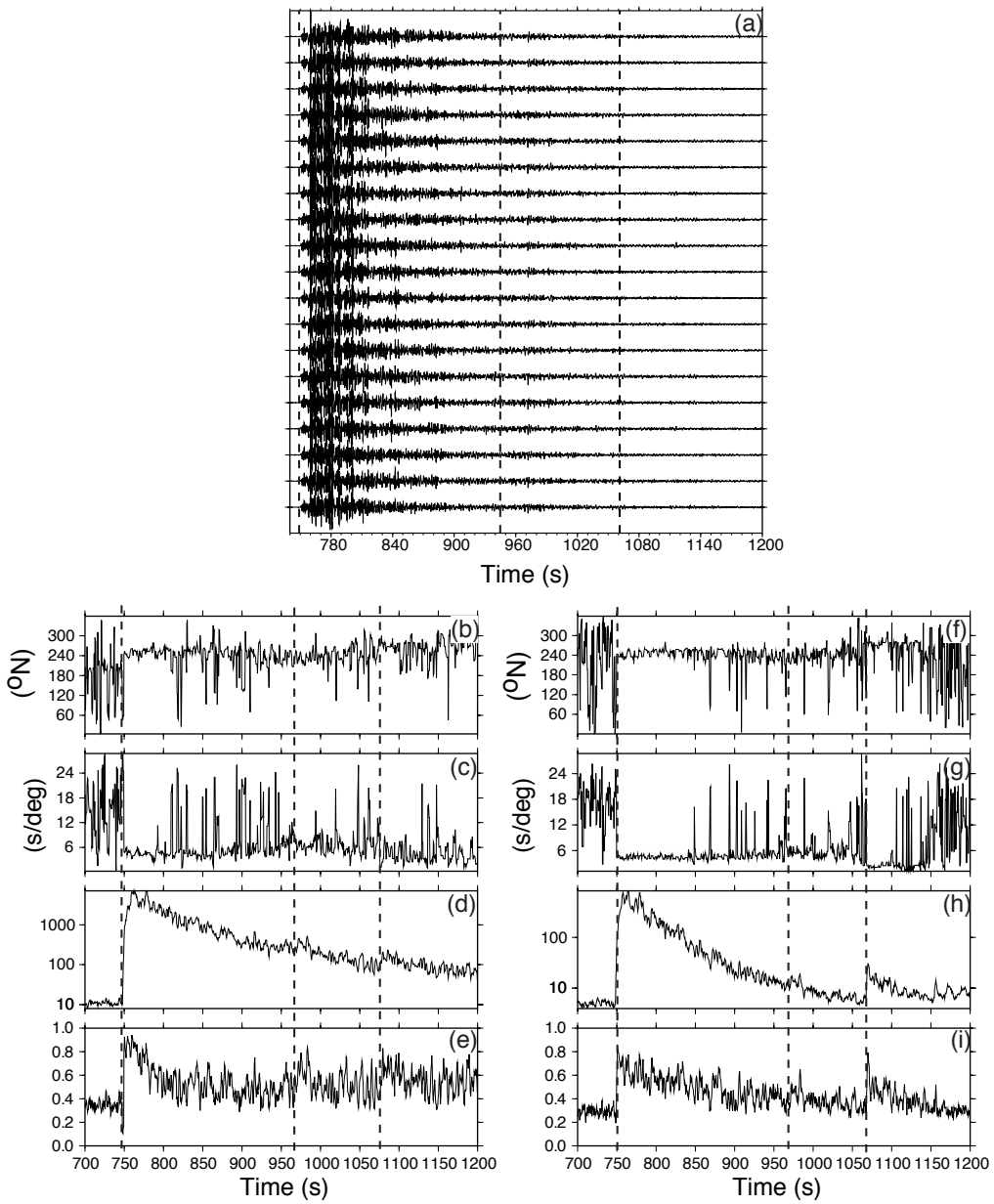

Figure 4.4: (a) Traces recorded at ILAR for the event of August 2, 1996 (161.5°E, 10.8°S, and depth of 33 km), with an epicentral distance of 84.7° and magnitude $M_W = 6.9$. On the bottom (panels (b) to (i)) we present the results of the sliding window process, for the frequency bands centered around 2 ((b) to (e)) and 5 Hz (panels (f) to (i)). From top to bottom, we present the backazimuth (panels (b) and (f)) [230.71°], slowness (panels (c) and (g)) [4.387 (s/deg) for PcP, 8.130 (s/deg) for PP, and 1.618 (s/deg) for $PKiKP$], the beam power (panels (d) and (h)), and coherency (panels (e) and (i)). Note the clear frequency dependence for the $PKiKP$. The vertical dashed lines present the theoretical arrival times for P [749.4 s], PP [945.4 s], and $PKiKP$ [1061.2 s]; time is relative to the origin time. The theoretical values, according to PREM (*Dziewonski and Anderson*, 1981), are shown in squared parentheses.

We compared the theoretical values of the travel time, slowness, and backazimuth with the observed ones, along with the coherency, to define the longest possible time window where the energy seemed to come from one direction, coherent with the main phase. In this work we consistently identify codas for two mantle phases ($P + PcP$ and PP), and one core phase ($PKiKP$). No other significant phase and coda pairs were detected in our data set.

Once we selected the phase-coda pairs and their corresponding time windows, we constructed beams with linear summation using the appropriate move-outs for the theoretical $PKiKP$ slowness for the PREM model (*Dziewonski and Anderson*, 1981). This kind of beamforming produces the least distortion to the waveforms, allowing them to be used in amplitude related studies. As done in similar studies (*Vidale et al.*, 2000; *Vidale and Earle*, 2000; *Koper et al.*, 2004), we computed the envelope of the beam because it gives a smooth function proportional to the energy flux.

The next step is to fit each one of the defined coda envelopes with a specific model. We assume a general model, usual in coda studies (*Sato and Fehler*, 1998), considering the velocity ($v(t)$) as a function of time (t), and take the logarithm of both sides:

$$\begin{aligned} v^2(t) &= A \cdot \frac{1}{t^{2n}} \cdot \exp(-2\pi Q_C^{-1} f t) \\ 2\ln(v(t)) &= \ln(A) - 2n\ln(t) - 2\pi Q_C^{-1} f t \\ \ln(v(t)) &= C - n\ln(t) - \pi Q_C^{-1} f t, \end{aligned} \tag{4.1}$$

where $C \equiv \frac{1}{2}\ln(A)$ is a constant proportional to the source excitation, site effect, and medium properties. The other two parameters, n and Q_C, represent the geometrical spreading and coda quality factor, respectively. This model is based on the single-scattering approximation, but has empirically proven to be appropriate in more general cases (*Sato and Fehler*, 1998). This problem is linear in the model parameters C, n, and Q_C^{-1}, but only if a single seismic wave is present in the signal $v(t)$. In this case it can be solved using a least squares technique (e.g *Menke*, 1989); however, in our case we commonly have the effect of pre-existing codas (such as $P + PcP$ or PP)

transforming the problem into a non-linear one.

Our first approach was to use a global search method, the Neighbourhood Algorithm, to search for the optimum values within a range. This method has been used in previous geophysical problems (*Sambridge*, 1999a,b; *Yoshizawa and Kennett*, 2002; *Begheim and Trampert*, 2003) and has proven to be very effective in handling non-linear problems with small dimensions (*Sambridge*, 2001). In our case, for every wave considered we need 3 model parameters to describe its coda; hence, in the case of having only $P + PcP$ and $PKiKP$ we would have a total of 6 model parameters, while in the case of also observing PP we would have a total of 9 model parameters, all of them interacting non-linearly with the rest. Each one of these sets of model parameter should be included from the beginning of the observed time window for that particular wave (defined with the slowness analysis), to the end of the data. Our preliminary results (*Leyton and Koper*, 2004) showed a strong correlation between the model parameters, precluding a unique determination of them, especially between 2 different waves. For example, we found a strong correlation (always larger than 0.90) between the model parameters for $P + PcP$ and those for $PKiKP$. This correlation is due to the fact that we fit the data for every phase from the beginning of its time window (from the slowness analysis), to the end of the seismogram. This way the model for $P + PcP$ started at its particular body wave arrival to the end of the $PKiKP$ coda, strongly influencing the model parameters that described the $PKiKP$ coda. This led us to the strong correlation between the model parameters, precluding the reliable comparisons of the results between different events.

Therefore, we decided to take a different approach: fit a model to all the pre-existing phases (one for $P + PcP$ and one PP, if present) and subtract the value (in power, *Shearer et al.* (1998)) predicted at the times corresponding to $PKiKP$, isolating the effect of this phase. To find a better model to predict $P + PcP$ and/or PP at the corresponding times for $PKiKP$ coda, we decided to consider not only the time window defined from the slowness analysis, but also a small time window at the end of the $PKiKP$ coda; this consideration also successfully removed the effect of noise. This "stripping" technique enabled us to study just the effect of $PKiKP$ coda,

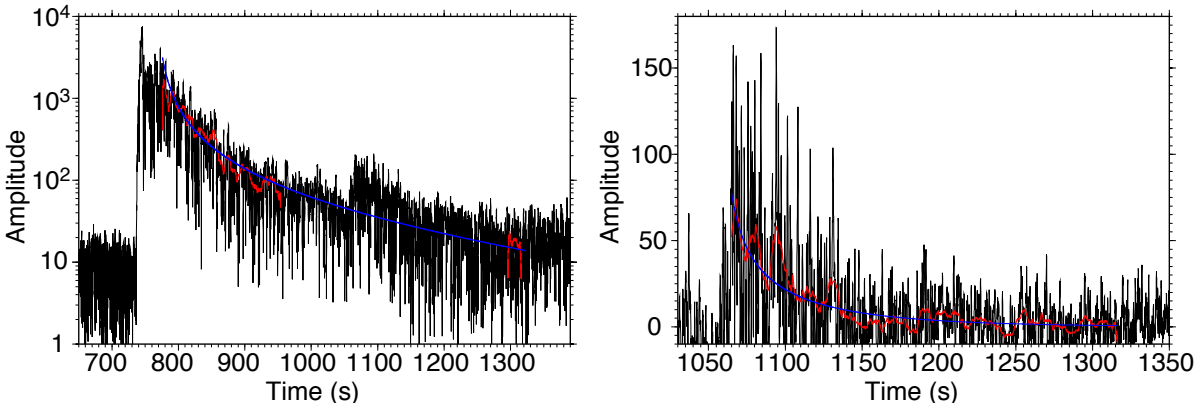

Figure 4.5: On the left, is presented the envelope of the event of May 13, 1998 (depth of 61.4 km, epicentral distance of 82.9°, and $M_W = 6.6$) recorded at ILAR, filtered around 5 Hz. Time is relative to the origin time and the amplitude is in arbitrary units, proportional to velocity. In black is shown the envelope, in red the results after applying the smoothing window, and in blue is the predicted envelope for $P + PcP$. On the right, is the same, but for $PKiKP$ time window, after subtracting the $P+PcP$ envelope.

removing the influence of pre-existing codas, as shown in Figure 4.5. Throughout this process, we smoothed the envelope using a moving window average of 3 s to remove the extreme points because we use least squares to do the fit, and this technique weights outliers heavily. Although the model obtained for the $PKiKP$ coda is still dependent in the model predicted by the $P + PcP$ and/or PP, this influence is mitigated by stacking different events with similar location into clusters.

An important consideration is that, for coda studies in the crust, the starting point to do the fitting is usually far from the direct wave arrival. For example, for S-waves in the crust, the coda is usually modeled starting after twice the travel time (*Rautian and Khalturin*, 1978). *Scherbaum et al.* (1991) found that the first part of the coda showed a slowness similar to the direct S-wave (interpreted as energy scattered near the source (*Dainty and Toksöz*, 1990)), and only after 1.5 - 2 times the S-wave travel time, the coda seemed to come from random directions, giving an average value of the heterogeneities in the medium (*Dainty and Toksöz*, 1990; *Dainty and Scultz*, 1995). In our case, $PKiKP$ coda has an amplitude very close to the noise level, giving a total duration of observable coda between 100 s and 200 s. Therefore, if we attempt to begin our fitting far from the $PKiKP$ direct arrival, we are left with

a very small time window to compute the model parameters. We decided to start the fit only 10 s after the $PKiKP$ arrival; hence, in all our single events fits, we probably have a significant influence of the direct phase.

It is worthwhile to point out that we also tried a simple model with two parameters, considering that $Q_C = 0$ in equation (4.1) (as done, for instance, by *Hedlin and Shearer* (2002)) with unsuccessful results: the fit obtained was mostly constrained by the initial part of the coda, not being able to adequately represent the tail. Furthermore, we experimented with fixing the geometrical spreading (n in equation (4.1)) to a theoretical value appropriate for body waves: $n = 0.5$, but the results remained unsatisfactory. In this case, the first part of the coda was usually misrepresented though the tail showed a much better fit. Finally, we decided to use a model with three free parameters, solving for the constant C, the geometrical spreading n, and the quality factor Q_C. By leaving n free to vary (especially the sign), we were able to obtain a better fit to the initial part of the coda, including the bias produced by the direct wave; meanwhile the attenuation factor Q_C is mostly sensitive to the later coda and, as mentioned before, this is the part of the coda that gives a better average of the medium properties (*Scherbaum et al.*, 1991).

4.4 Results

4.4.1 Average Values for $PKiKP$ Q_C

After removing the effect of pre-existing codas, we obtained two distinctive types of stripped $PKiKP$ codas: the first with a normal monotonically decaying behavior, while the second grows for the first 20-50 s up to a maximum value, before decaying to the noise level. An example of both types is shown in Figure 4.6 for two events recorded at ARCES. Note that, for the event on the right, the red curve (fit of $PKiKP$) increases in amplitude for almost 50 s to then decay; this type of behavior has been previously reported for $PKiKP$ coda and related to heterogeneities in the inner core (*Vidale and Earle*, 2000; *Koper et al.*, 2004). These types of coda show a

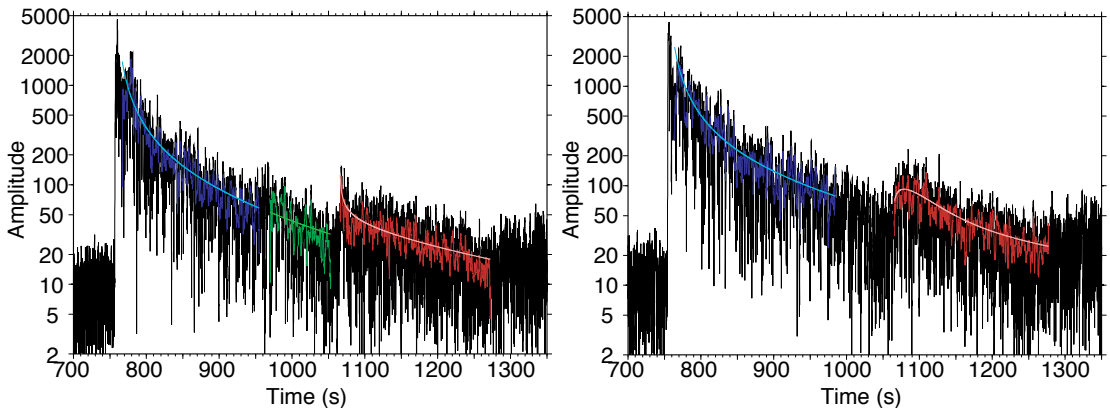

Figure 4.6: Examples of normally decaying coda ($n_{(+)}$ on the right) and growing coda ($n_{(-)}$ on the left) for 2 events recorded in ARCES. We first fit a model for $P + PcP$ and subtract it from the data to isolate $PKiKP$. If PP is present (as in the case of the right), we subtract the $P + PcP$ model at PP time, fit it and predict its value for the $PKiKP$ time. Time is relative to the origin time and amplitude is in arbitrary units, proportional to velocity.

value of the geometrical spreading less than 0 (i.e. $n < 0$), a completely unrealistic result. *Frankel and Clayton* (1986) pointed out that, in media with high level of heterogeneity, the single-scattering assumption might lead to wrong estimations in the geometrical spreading and to negative values of Q_C, probably the cause of our results. However, our purpose is to find acceptable values for the attenuation Q_C^{-1} which is mostly constrained by the tail of the coda; besides, the use of this particular model allow us the identification of two distinctive types of codas: normally decaying ($n_{(+)} > 0$) and growing codas ($n_{(-)} < 0$). After fitting all the stripped $PKiKP$ coda envelopes, we obtained $n_{(+)} = 0.362 \pm 0.0137$ and $n_{(-)} = -0.241 \pm 0.0279$, where the error bounds are 2σ in both cases. We emphasize that these numerical values are not meaningful in terms of Earth structure because they were obtained assuming single-scattering, which might not be valid, and they are strongly biased by the direct phase.

We computed the coda quality factor Q_C for each different frequency band, having very similar values of n in each case. The resulting Q_C are shown in Figure 4.7, as a function of distance, with the normally decaying codas ($n_{(+)} > 0$) in red and the growing codas ($n_{(-)} < 0$) in blue; each symbol represents a different array, as shown

in the upper right corner. The scatter in the results is very high, especially for larger epicentral distances; however, note that for the growing coda (in blue), Q_C ranges from only 100 to 1000, with an average very close to 500 for all epicentral distances. In a previous work (Chapter 3), considering only single-scattering, we showed that a growing $PKiKP$ coda can only be formed by heterogeneities inside the inner core; hence, we believe this value of $Q_C \sim 500$ should be representative of the inner core. Even more, the higher level of scatter for the normally decaying codas (in red) compared to those for the growing codas (in blue) is probably related to the fact that a normally decaying coda can be formed various places in the deep Earth, such as the lower mantle (Chapter 3); hence, the great variability of results simply reflect properties of different mantle regions. Also note that, in case of having the contribution of two completely different codas, one with normal decay ($n_{(+)}$) and one growing ($n_{(-)}$), the sum (in power) will look like a normally decaying coda, as schematically shown in Figure 4.8. Given the fact that at epicentral distances larger than 75° $PKiKP$ amplitudes tend to increase (*Koper et al.*, 2004), the probability of creating coda in the mantle and crust is augmented; therefore, the strong scatter seen in Figure 4.7 for the large epicentral distances ($\Delta = 75° - 90°$) just reflects combinations of values of the quality factor Q_C in the inner core and other places, such as the mantle and the crust. A similar result will come from the combination of an anomalously large $PKiKP$ phase at smaller distances (like those reported by *Koper and Dombrovskaya* (2005) and *Krasnoshcenkov et al.* (2005)) and a growing coda.

On the other hand, we can see from Figure 4.7 that in the distance range from 55° to 70° most of the observations have a $n_{(-)} < 0$ (growing coda). Similar results were obtained by *Koper et al.* (2004) and *Vidale and Earle* (2000) who found evidence of growing $PKiKP$ codas in the same distances. *Koper et al.* (2004) described this distance range as the most appropriate for studying the heterogeneities in the inner core because the main $PKiKP$ phase has a very small amplitude (due to the small reflection coefficient at the ICB); hence, the influence of scattering in the crust and and upper mantle should be very small.

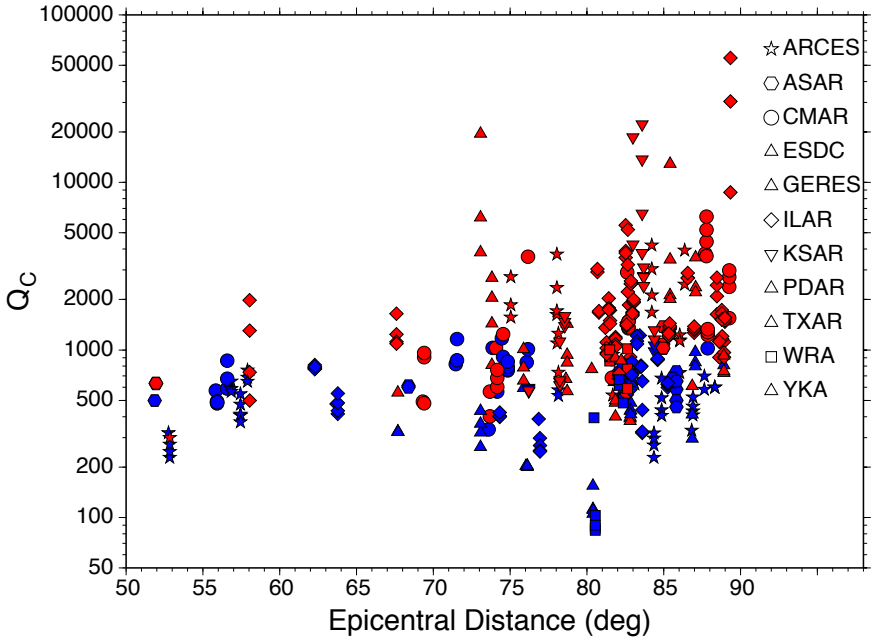

Figure 4.7: Results of Q_C for all frequencies bands as a function of the epicentral distance, in red for normally decaying coda ($n_{(+)} > 0$) and in blue for the growing codas ($n_{(-)} < 0$). Each symbol represents a different seismic array, as shown on the left. The vertical streaks are produced by the different results at different frequency, having all the same epicentral distance.

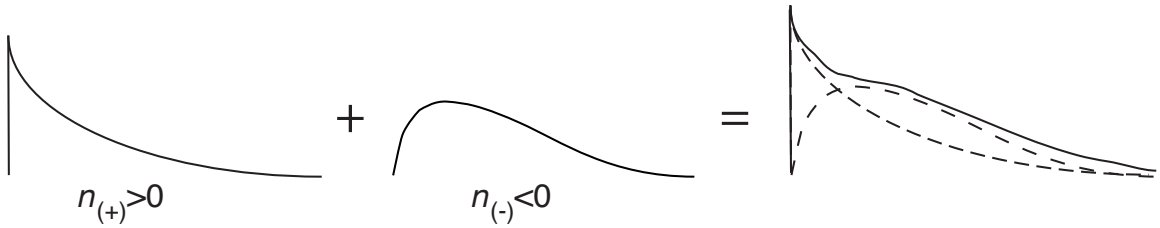

Figure 4.8: Schematic representation of the 2 types of codas (left and middle) and the sum, in power (right). On the left, normally decaying coda with $n_{(+)} > 0$, can be formed by scattering in the lower mantle, while in the middle, growing coda with $n_{(-)} < 0$ can only be produced by volumetric heterogeneities in the inner core (Chapter 3).

Figure 4.9 shows the geographical variation in Q_C values obtained for all the events studied here, for the frequency band centered at 5 Hz. On the left is shown Q_C for each event, as well as the location of the corresponding event (stars), the array stations (squares), and the projection on the surface of $PKiKP$ ray path (dashed lines). The circles show the $PKiKP$ bounce point at the inner core boundary, in red those events with normally decaying codas ($n_{(+)} > 0$) and in blue those with growing codas ($n_{(-)} < 0$); while the intensity is proportional to Q_C (see scale in Figure). On the right is shown the values of quality factor Q_C as a function of epicentral distance; each symbol represents a particular array, with the same color code. Results in Figure 4.9 still show a strong level of scatter; this variability cannot be explained in terms of source location, depth, magnitude, or focal mechanism. Again, the growing codas (in blue) present values between 100 and 1000 (with and average close to 500) for all epicentral distances, and, between 55° and 70°, most of the observations present a growing $PKiKP$ coda. We could not find a relation between the changes in Q_C and time, even when looking at a particular source region and array.

Given the strong scatter in the Q_C values, we attempted to further improve the signal by doing source stacking: stack different events with similar source location that are recorded by the same array. This process will reduce the scatter in the results by averaging out the differences between events while retaining the signal coming from the inner core: the unknown phenomenon that produces the scatter in the results should not add coherently in the source stack, but the signal from the inner core should. It will also help produce a more stable estimation (and prediction) of the $P + PcP$ and/or PP phase; hence, leading to a better prediction and subtraction at the $PKiKP$ time window, which in turn should lead to a more robust model for the $PKiKP$ coda. We defined 11 clusters at 7 different arrays, requiring that at least 4 events exist in any cluster array (see Table 4.2). In order to compute the source stacks, we first normalized each receiver stack by the average $PKiKP$ amplitude over a time window of 5 s. Then, we aligned all receiver stacks at the theoretical $PKiKP$ time and computed the average point by point. We also computed the standard deviation for each point in time and used these values to obtain errors in the model

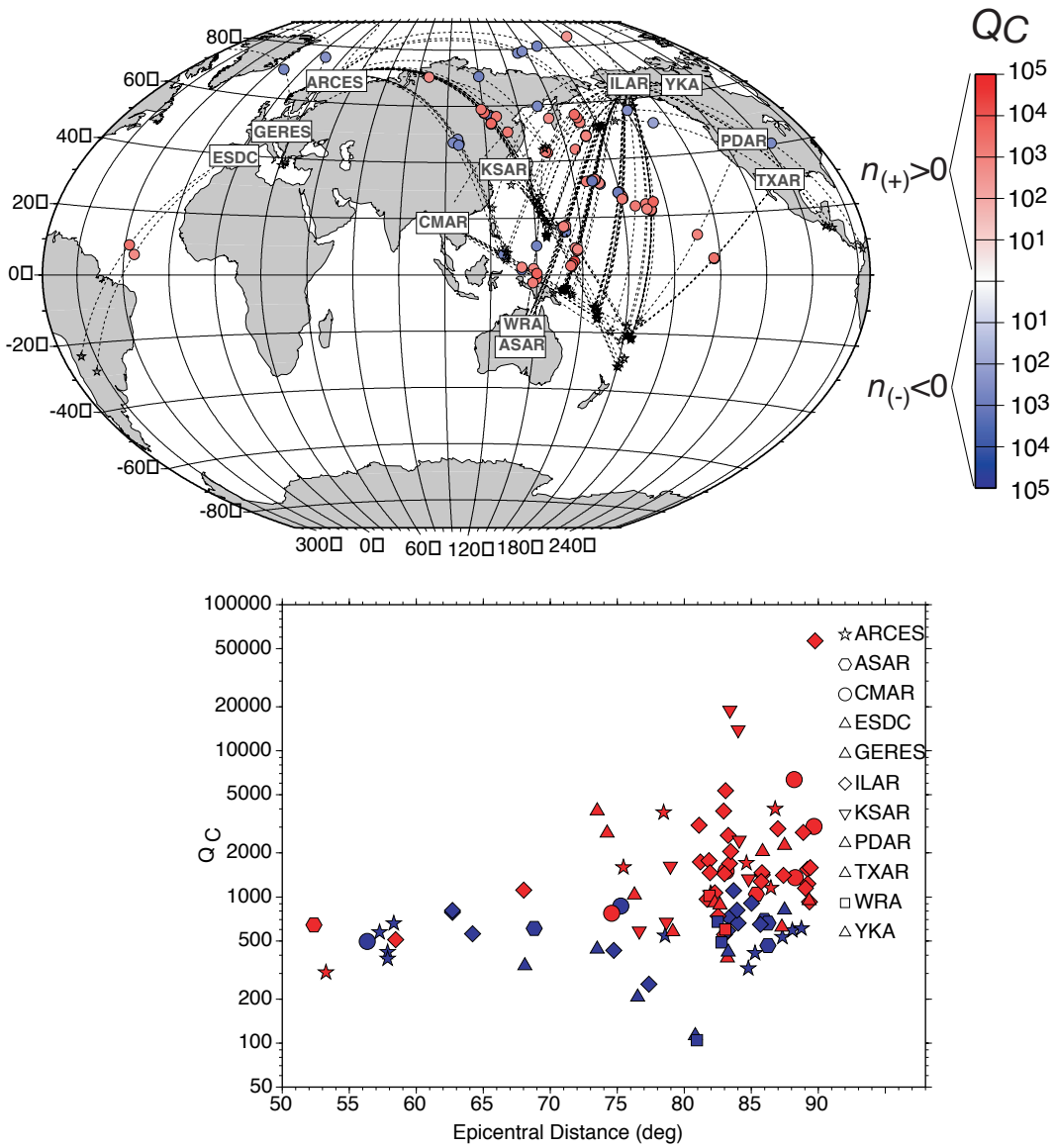

Figure 4.9: On the right is shown the geographical variation of Q_C, recorded at 5 Hz, for all the events in our data set; in red for normally decaying codas ($n_{(+)} > 0$) and in blue for growing codas ($n_{(-)} < 0$), with the intensity proportional to the coda quality factor (Q_C). On the left is presented the same data, but as a function of the epicentral distance, using the same color code. Each symbol represents a different array, as shown in the upper right corner.

parameters following known relations for the least squares technique (*Menke*, 1989).

Table 4.2: Results fo Q_C for the different clusters

Array	Cluster	Number of Events	$Q_C \pm \sigma^{\dagger}$
ARCES	A	4	1783 ± 2390
ARCES	B	10	974 ± 441
ARCES	D	4	504 ± 231
ASAR	B	4	589 ± 182
CMAR	D	11	315 ± 227
ILAR	E	13	598 ± 134
ILAR	F	9	565 ± 261
ILAR	G	9	324 ± 112
KSAR	A	7	819 ± 294
WRA	A	5	489 ± 177
YKA	C	7	711 ± 166

† Standard deviation.

In Figure 4.10, we present a map with the resulting geographical clusters (right), and Q_C as a function of epicentral distance (left); the vertical dashed lines show one standard deviation for each value. Note that the scatter has been strongly reduced, leading to a more robust estimation of Q_C and that those values farther from the mean (~ 500) present a larger error. Next, we computed a final, overall average value of Q_C by considering the standard deviation of each cluster (*Bevington*, 1969). Clusters with large differences between individual traces (receiver stacks) will have a larger error (σ in Table 4.2), which, under our averaging technique, will be down-weighted in the final average. We ultimately obtain an average of $Q_C = 517 \pm 57$ considering all normally decaying ($n_{(+)} > 0$) and growing ($n_{(-)} < 0$) codas.

Here we did not find a frequency dependence for Q_C, but given the limited range used (from 1 to 5 Hz) we cannot draw significant conclusions. However, we consistently found more observations of $PKiKP$ coda at higher frequencies, just as *Koper et al.* (2004) for the same epicentral distances ($50^{\circ} < \Delta < 90^{\circ}$). This could be due to the characteristics of the heterogeneities or the properties of the arrays: from Figure 4.3 we can see that, in general, the noise becomes less coherent as frequency increases; hence, the possibilities of observing the faint signal coming from the in-

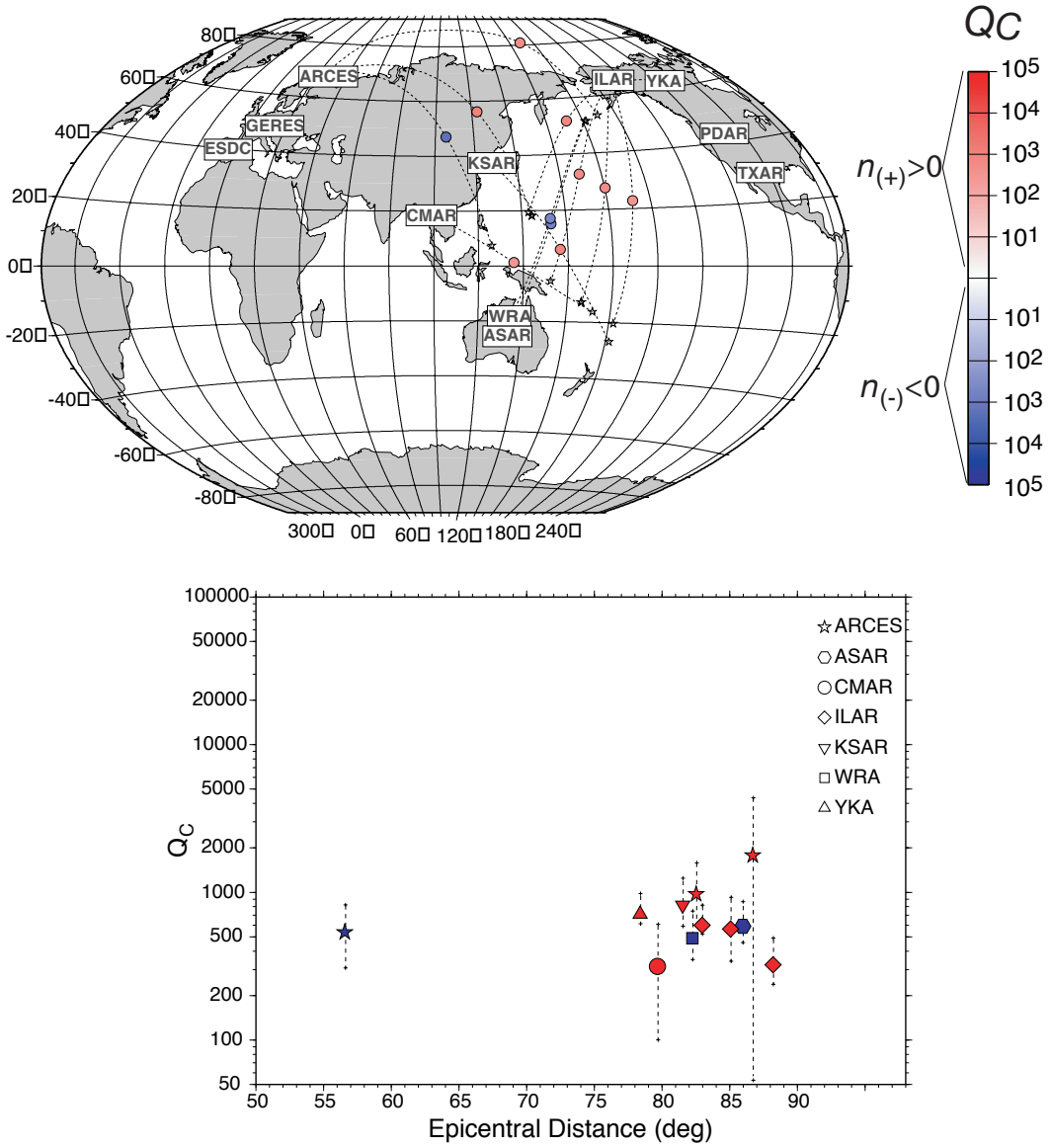

Figure 4.10: Geographical variation of Q_C, recorded at 5 Hz, for all the events in the defined source clusters; in red for normally decaying codas ($n_{(+)} > 0$) and in blue for growing codas ($n_{(-)} < 0$), with the intensity proportional to the coda quality factor (Q_C). On the left is presented the same data, but as a function of the epicentral distance, using the same color code, with the vertical dashed lines representing the standard deviation. Each symbol represents a different array, as shown in the upper right corner.

ner core are increased for higher frequencies. We are not able to resolve this issue with the present data set, but in Chapter 3 we showed that the total growth of the "spindle"-shaped codas depend upon the content of small wavelengths of volumetric heterogeneities within the inner core, perhaps giving some insights of the scale-length of the scatterers.

4.4.2 Geographical Variation in $PKiKP$ Coda

In previous studies, the observation of $PKiKP$, but not its coda, was correlated to the signal-to-noise ratio of $PKiKP$, although not all the examples could be explained this way (*Koper et al.*, 2004). Here we argue in favor of a geographical variation in $PKiKP$ coda generation that is related to the Earth' structure and not to the properties of the arrays used. Figure 4.3 present the coherency of seismic noise as a function of frequency for all IMS arrays used (see Figure caption for details). This measurement is useful when comparing observations from different arrays because we study seismic waves with very low signal-to-ratio; hence, the analysis of data from arrays with large noise-coherency will be very difficult, while those arrays with low noise-coherency will present more reliable observations. From this Figure we can see that ESDC (with only 2 positive $PKiKP$ coda observations) has a comparable noise-coherency to ILAR (with 40 positive observations); even more, from Table 4.1, we can see that both arrays have similar of numbers of elements, aperture, and aspect ratios (see Table caption for details), indicating that their capabilities of observing weak signals (such as $PKiKP$ and its corresponding coda) are comparable. ESDC positively detected $PKiKP$ waves coming from Mexico and South America's subduction zone, as well as some from the Aleutians, but only two of those presented $PKiKP$ coda. Furthermore, ARCES was able to record some $PKiKP$ codas coming from the Pacific Ocean and Asia, but none from the Atlantic Ocean (having positively identified $PKiKP$ arrivals from Mexico's subduction zone). Likewise, YKA (with a small noise coherency, rather large aperture, and large number of elements) has some positive observations of $PKiKP$ waves from the subduction zone in Central and South America, but most of its $PKiKP$ coda come from the

west of the Pacific Ocean. Therefore, we believe that the geographical pattern seen in the observation of the $PKiKP$ coda is related to structure in the deep Earth, rather than from properties of the arrays and events. Note that this pattern strongly resembles the previously described hemispherical variations, but we do not have the coverage necessary to support this type of pattern, especially given the fact that most of our data samples only the northern hemisphere. Nevertheless, we believe that the simplest explanation for our observations (strong scattering from the Pacific Ocean and Asia and few $PKiKP$ coda observations from the Atlantic Ocean) is given by the hemispherical differences in structure reported for the inner core, as discussed in section 4.5.2 of the Discussion.

Our observations also agree with previously reported $PKiKP$ codas: *Vidale and Earle* (2000) stacked earthquakes and nuclear explosions mostly from the western Pacific (Japan's subduction zone) and Asia (Novaya Zemlya); while only one event was located in the Atlantic Ocean. In the work by *Koper et al.* (2004) most of the observations come from the Pacific Ocean and Asia and *Poupinet and Kennett* (2004) only studied the array WRA (included in this study), located in Australia (southwest Pacific). Also note that our observations also coincide with the observation of a complicated uppermost inner core made by *Stroujkova and Cormier* (2004), suggesting that the source of our $PKiKP$ coda observations is in this region (upper layer of the inner core).

4.5 Discussion

4.5.1 Intrinsic vs. Scattering Attenuation

Previous work has suggested that the observed crustal attenuation (Q_{obs}^{-1}) is the combination of intrinsic (Q_I^{-1}) and scattering (Q_S^{-1}) attenuation (*Dainty and Toksöz*, 1981; *Cormier*, 1982):

$$Q_{obs}^{-1} = Q_I^{-1} + Q_S^{-1}. \tag{4.2}$$

Note that Q_{obs} is usually referred to the quality factor for body waves and, in other

studies (*Frankel and Clayton*, 1986), has been called *transmission Q*, as opposed to *coda Q*. Studies of P coda in the crust have reported $Q_C = 270$ at 1 Hz, neglecting the effect of the geometrical spreading (*Morozov and Smithson*, 2000). These values are comparable to those obtained from Lg coda (*Singh and Herrmann*, 1983; *Dainty*, 1990) suggesting that the source of P coda could be the scattering of Lg phases (*Dainty and Toksöz*, 1990; *Dainty and Scultz*, 1995). *Herrmann* (1980) and *Mitchell* (1980) inferred that Q_C from Lg coda waves reflect the intrinsic attenuation in the crust (Q_I); hence, values of P coda in the crust seem to reflect intrinsic attenuation. We cannot simply extend this result to the inner core, but, as a first approximation, if we assume $Q_C^{-1} \approx Q_I^{-1}$, then

$$Q_S^{-1} = Q_{obs}^{-1} - Q_C^{-1}. \tag{4.3}$$

Values of observed quality factor (Q_{obs}) in the inner core range from 120 to 600 (*Qamar and Eisenberg*, 1974; *Doornbos*, 1983; *Niazi and Johnson*, 1992; *Bhattacharyya et al.*, 1993; *Cormier et al.*, 1998) with a recent value of 300 (*Li and Cormier*, 2002), but has been reported to vary with depth (*Doornbos*, 1974; *Master and Shearer*, 1990; *Souriau and Roudil*, 1995; *Cao and Romanowicz*, 2004). Higher values of the quality factor ($Q_{obs} \sim 600$) has been reported for the quasi-western hemisphere (*Wen and Niu*, 2002). Since our coda samples primarily the outer shell of the quasi-eastern hemisphere, we assume $Q_{obs} = 300$, so

$$\begin{aligned} Q_S^{-1} &= 0.001395 \\ Q_S &\approx 715. \end{aligned} \tag{4.4}$$

Assuming the lower bound ($Q_{obs} = 175$) leads to $Q_S = 265$. We can see that in both cases the scattering attenuation is comparable to the intrinsic attenuation. Even more, based on the analysis of the effect of small inclusions in the wave propagation using finite difference simulations, *Frankel and Clayton* (1986) found that, if $Q_C > Q_{obs}$, then the attenuating process is mostly scattering, in our case $Q_C = 517 >$

$Q_{obs} = 300$. Similar results were obtained by *Richards and Menke* (1983) by studying the scattering effect of a set of thin layers with changes in velocity. This result contradicts our assumption of single-scattering and it is opposite to the situation in the crust, where the scattering attenuation can be neglected and the loss of energy is entirely attributed to intrinsic attenuation (*Mitchell*, 1995). Indeed, *Cormier and Li* (2002) have suggested that most of the attenuation seen in the inner core is a product of scattering, showing a rather weak intrinsic attenuation. We believe that the stronger scattering attenuation in the inner core compared to the crust could be caused by a leakage of energy out of the system (the inner core), which does not happen for regional distances in the crust. We speculate that a strong scattering process inside the inner core would shoot energy in directions where it cannot be reflected back to the receiver. In this way, the losses related to scattering in the inner core would be more significant than in the crust.

Another key observation is the "spindle"-shaped or growing coda, which has also been observed in the Moon, where a lack of water inhibits significant intrinsic attenuation (*Dainty and Toksöz*, 1981). *Dainty and Toksöz* (1981) successfully interpreted these codas (using a diffusion model and radiative transfer energy) as the result of a strongly scattering layer overlying a more homogenous medium; therefore, the observation of growing $PKiKP$ codas suggests strong scattering in the inner core. We think that in order to precisely separate the effect of scattering from intrinsic attenuation, we need to follow a similar approach (e.g. *Wu*, 1985; *Frankel and Wennerberg*, 1987; *Margerin and Nolet*, 2003a; *Lacombe et al.*, 2003; *Jemberie and Langston*, 2005). These computations are outside the scope of the present work but should be addressed in the future.

4.5.2 Hemispherical Pattern

Evidence of long-scale variations in the convection of the outer core come from long-scale anomalies of the observed magnetic field. For example: low secular variations over the Pacific Ocean (*Merrill et al.*, 1998; *Gubbins and Gibbons*, 2004), the hemispherical dichotomy of the outer core temperature inferred from geomagnetic sec-

ular variations (*Bloxham and Jackson*, 1990), and the different characteristics of the non-axial dipole components of the geomagnetic field pattern in the between the Pacific and Atlantic Oceans (*Walker and Backus*, 1996; *Johnson and Constable*, 1998). These anomalies in the geodynamo are clear evidence of variations in the strength of the convection of the outer core could be responsible for the observed differences in structure of the inner core (*Wen and Niu*, 2002; *Sumita and Yoshida*, 2003). At any rate, any mechanism able to produce the hemispherical pattern in the IC has to hold for a long period of time, because the solidification of the top 100 km of the inner core would probably take 100 Ma (*Yoshida et al.*, 1996).

Wen and Niu (2002) found clear differences between the two quasi-hemispheres in travel times and waveforms of PKP branches. They modeled these observations using a hybrid method, combining generalized ray theory and finite differences (*Wen and Helmberger*, 1998b), in terms of the presence of small-scale heterogeneities in the upper inner core, requiring a 5-9% rms velocity variation in the "eastern" hemisphere compared to less than 3% in the "western" hemisphere. This model agrees with our observations of strong scattering in the Pacific Ocean and Asia (quasi-eastern hemisphere) and few in the Atlantic Ocean (quasi-western hemisphere). Another key observation is that the previously described isotropic outer shell of the inner core (probably hosting the small-scale heterogeneities) appears to have different thickness on both hemispheres, being less that 100 km in the "western" hemisphere and 400 km in the "eastern" hemisphere (*Creager*, 1999; *Garcia and Souriau*, 2000). These heterogeneities, mostly present in the isotropic "eastern" hemisphere, could be from variations in orientation of strongly anisotropic Fe-hcp crystals (*Bergman*, 1997; *Creager*, 1999; *Cormier and Li*, 2002) (with scale-lengths of kilometers (*Bergman*, 1998)), presence of partial melt (*Singh et al.*, 2000), or layering within the IC (*Cormier et al.*, 1998), all of them capable of producing scattering. Hence, the differences between the two hemispheres appears to be the most plausible explanation to the geographical pattern seen in the observation of $PKiKP$ coda. Given that the structure developed in the inner core through its growth is essentially controlled by how the heat is transferred into the outer core (*Sumita and Yoshida*, 2003), *Wen and Niu* (2002)

proposed a different vigorousness of convection on top of the two hemispheres, leading to different geometric inclusions of melt and/or different alignment of the crystals as a possible explanation for the hemispherical pattern. This result was supported by the study of *Yu et al.* (2005) of the lowermost outer core, where they found a hemispherical difference in the P-wave velocity structure, and, assuming an inversely proportional relationship between P-wave velocity and density, they predicted a lower enrichment of light elements in the quasi-western hemisphere. This can be taken as direct evidence of a weaker convection on this side of the inner core, since compositional buoyancy of light elements is a key driving force for the geodynamo (*Lister and Buffett*, 1995; *Stacey and Stacey*, 1999).

Oreshin and Vinnik (2004) found hemispherical difference with the "western" hemisphere having elastic and anelastic anisotropy, with the fastest velocity in the same direction of the strongest attenuation (the Earth's rotation axis); while the "eastern" hemisphere showed weak or null anisotropy. They interpreted these results as a function of partial melt inclusions between large, aligned crystals of iron hcp (*Bergman*, 1997; *Cormier and Li*, 2002); changes in depth would be a function of the partial melt content. The inclusion of anisotropically oriented pockets of partial melt within an isotropically oriented matrix of Fe-hcp crystals can produce anisotropy (*Singh et al.*, 2000), as proposed by *Oreshin and Vinnik* (2004) for the "western" hemisphere. If this was the case, then we should see a strong scattering signal from this hemisphere, not shown in our data. On the other hand, the presence of isotropically oriented pockets of partial melt within an anisotropically oriented matrix of Fe-hcp crystals does not alter the anisotropy (*Singh et al.*, 2000); hence, the presence of pockets of partial melt is not required to explain the observed isotropy and strong scattering in the "eastern" hemisphere. We do not rule out the possibility that, in the quasi eastern hemisphere, some partial melt might get trapped between randomly oriented Fe-hcp crystals, contributing to the observed scattering, but the main signal comes from the orientation of the crystals. The presence of partial melt might be evaluated by comparing the intrinsic attenuation between the two quasi-hemispheres: if the intrinsic attenuation is stronger in the "eastern" hemisphere, it is probable that

the presence of partial melt might explain this difference. But, if both hemispheres have the same intrinsic attenuation, we could expect that the same mechanism that dissipates the energy is present on both hemispheres, and due to the lack of partial melt on the "western" hemisphere, we should not have it in the "eastern" hemisphere.

The other plausible explanation for the strong scattering is the misalignment of crystals in the outer shell of the inner core (*Bergman*, 1997; *Creager*, 1999; *Cormier and Li*, 2002). The observed anisotropy in the IC led to two models based on texturing of the anisotropic Fe-hcp crystals: *Yoshida et al.* (1996) suggested that the inner core will tend to grow in the radial direction (due to the efficiency in transporting heat in the direction perpendicular to the rotation axis) producing a stress large enough to induce a solid-state flow leading to recrystallization. On the other hand, *Bergman* (1997, 1999, 2003) favors a solidification texturing that will not be destroyed by recrystallization. The first model predicts the alignment of the c-axis in the direction perpendicular to the rotation axis, while the second predicts a random orientation of the c-axis in the plane transverse to the local cylindrical radial. *Bergman* (1997) argued for geometrical reasons of the ray paths of seismic waves that travel through the inner core as an explanation of the variation of anisotropy in depth; but this argument cannot explain the hemispherical changes in the thickness and/or strength of the anisotropy on top of the inner core. Hence, some kind of recrystallization process must take place in the inner core, able to explain the general observed anisotropy (*Yoshida et al.*, 1996). During this process, we believe that any inclusion of partial melt will be squeezed out of the inner core, due to the perfect alignment of the crystals. We suggest a combination of both: a solidification texturing in the quasi-eastern hemisphere would lead to the observed isotropic and strongly scattering layer, while a strong recrystallization process on the quasi-western hemisphere would lead to the observations of anisotropy (*Sumita and Yoshida*, 2003) and little to null scattering. The recrystallization process has to be weaker or take longer time on the "eastern" hemisphere to be able to produce the observed thick isotropic layer ($\sim$ 400 km).

The details in which these two process work depend upon the heat flux differences between the quasi-hemispheres, where a complete agreement has not been reached:

based on laboratory experiments of outer core convection with thermal coupling between the inner core and a heterogeneous mantle, *Sumita and Olson* (1999) predicted a 'colder' quasi-western hemisphere, with faster growth; while the findings of *Wen and Niu* (2002) (in the upper inner core) and *Yu et al.* (2005) (in the lower outer core) on the velocity of P-wave and attenuation indicate a more vigorous convection on the "eastern" hemisphere. A key point made by *Sumita and Olson* (1999) is that the phase shift between a colder-than-average lower mantle and the inner core (due to the Earth's rotation) is directly proportional to the heat flux in the CMB; hence, with a lower heat flow in the location of the cold slab at the CMB, we could match the position of the anomalously cold upper inner core predicted by *Sumita and Olson* (1999) and the region of vigorous convection in the lower outer core found by *Yu et al.* (2005). At any rate, here we discuss both possibilities and their consequences to the growth of the inner core.

4.5.3 Stronger Convection in the "Western" Hemisphere

Sumita and Olson (1999) explained the hemispherical differences in the inner core by a strain-driven recrystallization, caused by the large load produced by a faster growth of the inner core in the quasi-western hemisphere, leading to lattice preferred orientation (lpo) and anisotropy (*Sumita and Yoshida*, 2003). This recrystallization process should be relatively fast, not allowing the inclusion of partial melt that could cause scattering. Recently, *Van Orman* (2004) found a very low value for the viscosity in the IC, which under the proposed mechanism of Harper-Dorn creep, leads to almost instantaneous realignment of the crystals (from $\sim 3 - 300$ years for a shear stress between $10^2 - 10^4$ Pa (*Van Orman*, 2004)).

On the other hand, the "eastern" hemisphere will be characterized by a less vigorous convection, leading to a slower growth rate. Through this process, pockets of partial melt would have to be trapped between the randomly aligned crystals, generating a smaller load on the deeper inner core and a clear source of scattering. This lower load will produce a smaller stress, responsible for a thicker isotropic layer in this hemisphere (~ 400 km). This stress has to be time dependent, being a function of the

load deposited on top, otherwise, the slow growth rate assumed for the quasi-eastern hemisphere will give long time for recrystallization, leading to the formation of a thin isotropic layer.

Another possibility could be a different texturing on top of the inner core due to the flow in the fluid core (*Bergman et al.*, 2002). This group found that solidification driven convective flow in salt water (a proxy to Fe-hcp) causes a texture where the c-axes align at 90° to the direction of the flow, due to the influence of the platelet nature of hcp dendrites. Differences in the strength of the convection might cause a different flow near the top of the inner core, leading to a different texture solidification: a stronger convection on the "western" hemisphere would produce a preferred flow of liquid into the outer core, leading to the perfect alignment of the Fe-hcp crystals and into anisotropy. Meanwhile, in the "eastern" hemisphere, a less vigorous convection might not produce this particular flow, producing an anisotropic alignment of the crystals (with or without the inclusion of partial melt); later, a recrystallization process should take over and realign the crystals in order to create the observe anisotropy inside the bulk inner core.

4.5.4 Stronger Convection in the "Eastern" Hemisphere

Considering a more vigorous convection in the "eastern" hemisphere (*Wen and Niu*, 2002; *Yu et al.*, 2005) will lead to a faster growth of this side of the inner core, with the formation of primary dendrites in the direction of the heat flow (known as directionally solidified growth, seen in metallic alloys) forming columnar crystals (*Bergman*, 2003). *Bergman* (1997, 1999) experimentally found that c-axes of hcp crystals will randomly lie in the plane perpendicular to the heat flow, maybe creating isotropic inclusions of partial melt. *Stixrude and Cohen* (1995) found that Fe-hcp phase has 4% of anisotropy in the direction of the c-axes, at 0 K, but from experiments (*Mao et al.*, 1998) and first principle calculations (*Steinle-Neumann et al.*, 2001) was found that the influence of temperature was to increase the anisotropy to over 10% in the a-axes. If this is true, then we need to consider the inclusion of partial melt between the randomly oriented crystals in the "eastern" hemisphere to create

the observe scattering signal. However, recent results by *Gannarelli et al.* (2003, 2005), based on density function theory, have questioned the earlier interpretation of the anisotropy of Fe-hcp crystals at core conditions; hence, there is still a possibility that the scattering signal comes just from the misalignment of strongly anisotropic iron crystals. After the crystals have solidified, some type of stress will take over and produce the recrystallization responsible of the observed anisotropy and extrude any possible inclusions of partial melt. Possible sources of stress for a post-solidification realignment of crystals (recrystallization) are Maxwell stresses (*Karato*, 1999), differences between the gravitational equipotential and thermodynamical equilibrium of the inner core (*Yoshida et al.*, 1996), inner core thermal convection (*Jeanloz and Wenk*, 1988), and longitudinal flow due to Lorentz stresses (*Buffet and Wenk*, 2001).

The "western" hemisphere will not present any inclusion of partial melt, having the observed anisotropy (or thin isotropic layer) due to the alignment of the crystals formed at a slower growth ratio. From our observations and computations (Chapter 3), we cannot completely rule out the presence of a small layer with heterogeneities (either partial melt or misalignment of crystals) on top of the "western" hemisphere but it will have to be thinner than 100 km. Because this isotropic layer is relatively thin, we do not believe that can produce a stress large enough to form the observed anisotropy in this hemisphere following the process detailed by *Yoshida et al.* (1996). Hence, we think that the process of recrystallization would be caused by a uniform stress (such as those proposed by *Karato* (1999), *Jeanloz and Wenk* (1988), or *Buffet and Wenk* (2001)) leading to the anisotropic structure only related with time: this hemisphere appears to have a slower growth, giving enough time to produce the observed anisotropy.

4.6 Conclusions

Due to the interference between the coda of different seismic waves, the determination of the quality factor Q_C of deep Earth phases is very complicated; however, we were able to compute reasonable values for $PKiKP$ coda by using a "stripping"

technique and combining source and receiver stacks. There seems to be a mechanism that produces strong changes in the estimation of Q_C for individual events, that cannot be explained in terms of the focal mechanism, geographic location of the source, or epicentral distance. This mechanism might be due to the some temporal changes in the medium, in particular the inner core, although we cannot rule out the intrinsic difficulty of working with high frequency data. However, this bias can be successfully removed by stacking the signals of different events with similar locations recorded at the same array. Using this procedure, we obtained a quality factor for $PKiKP$ coda of $Q_C = 520 \pm 57$.

We found that scattering attenuation is important in the inner core, in contrast with the crust where it can even be neglected. This phenomenon could be due to the presence of more heterogeneities in the inner core with respect to the crust, or simply smaller intrinsic attenuation. We feel that it is necessary to compute the effect of intrinsic and scattering attenuation in the inner core, using multiple-scattering approaches. This could help resolve the issue of presence of partial melt in the whole inner core or only in one part.

Our results indicate a geographical pattern in the observation of $PKiKP$ coda could be related to the hemispherical variations previously reported in the inner core: despite the lack of global coverage in our data set, the simplest explanation to the presence or absence of $PKiKP$ coda comes from the hemispherical differences differences in structure reported for the inner core. Furthermore, the most probable mechanism for the observed signal from the inner core comes from misalignment of crystals, rather than presence of partial melt.

Appendix A

Copyright Permission

Request of Copyright Permission:

Hello,

My name is Felipe Leyton and I'm a PhD candidate at Saint Louis University. Last year I published a paper in your journal (details below) and I plan to make it part of my Thesis; hence, I need a copyright permission. I'll be reproducing the whole article.

The article is:

Title: 'On the lack of seismic discontinuities within the inner core'

Authors: F. Leyton, K.D. Koper, L. Zhu, and M. Dombrovskaya

Journal: Geophys. J. Int.

Volume: 162

Pages: 779-786

Doi: 10.1111/j.1365-246X.2005.02480.x

Year: 2005

Thesis:

Title: 'Study of the Inner Core Fine-Scale Structure Using Seismic Array'

Author: F. Leyton

University: Saint Louis University, Dept. Earth & Atmosph. Sciences

Thank you for your time. Sincerely,

Felipe Leyton, PhD Candidate

email: leytonfo@eas.slu.edu

Address: Dept. Earth & Atm. Scs. - Saint Louis University

3507 Laclede Ave.

Saint Louis, MO 63103, USA

Phone: (1-314) 977-3654

Fax: (1-314) 977-3117

Answer from the Editor:

Dear Mr Leyton

Thank you for your email request. Permission is granted for you to use the material below for your thesis subject to the usual acknowledgements and on the understanding that you will reapply for permission if you wish to distribute or publish your thesis commercially.

Good luck!

Best wishes,

Zoë Ellams (Miss)

Permissions Co-ordinator

Blackwell Publishing

9600 Garsington Road, Oxford, OX4 2DQ

Tel: 00 44 1865 476149

Fax: 00 44 1865 471149

Zoe.Ellams@oxon.blackwellpublishing.com

All future permission requests should be sent to

mailto:journalsrights@oxon.blackwellpublishing.com

Blackwell is committed to creating a culture of value and respect for all of our staff. We expect to work in an environment where there are high standards of behaviour and achievement. We maintain a culture which operates within accepted boundaries of professional behaviour and performance.

References

Aki, K. (1957), Space and time spectra of stationary stochastic waves, with special reference to microtremors, *Bull. Earth. Res. Inst.*, *35*, 415–457.

Aki, K. (1969), Analysis of coda of local earthquakes as scattered waves, *J. Geophys. Res.*, *74*, 615–631.

Aki, K. (1973), Scattering of P waves under the Montana LASA, *J. Geophys. Res.*, *78*, 1334–1346.

Aki, K., and B. Chouet (1975), Origin of coda waves: source, attenuation, and scattering effects, *J. Geophys. Res.*, *80*, 3322–3342.

Aki, K., and P. G. Richards (2002), *Quantitative Seismology*, University Science Books, Sausalito, California.

Alfè, D., J. M. Gillian, and G. D. Price (2000a), Constraints on the composition of the Earth's core from *ab-initio* calculations, *Nature*, *405*, 172–175.

Alfè, D., J. M. Gillian, and G. D. Price (2000b), Thermodynamic stability of Fe/O solid solution at inner-core conditions, *Geophys. Res. Lett.*, *27*, 2417–2420.

Alfè, D., J. M. Gillian, and G. D. Price (2002), Composition and temperature of Earth's core constrained by combining *ab-initio* calculations and seismic data, *Earth. Planet. Sci. Lett.*, *95*, 91–98.

Anderson, O. L. (2003), The three-dimensional phase diagram of iron, in *Earth's Core: Dynamics, Structure, Rotation*, edited by V. Dehant, K. C. Creager, S. Karato, and S. Zatman, pp. 83–104, AGU monograph.

Bannister, S. C., E. S. Husebye, and B. O. Ruud (1990), Teleseismic P coda analyzed by three-component and array techniques: deterministic location of topographic P-to-Rg scattering near the NORESS array, *Bull. Seismol. Soc. Am.*, *80*, 1969–1986.

Battaille, K., and S. M. Flatté (1988), Inhomogeneities near the core-mantle boundary inferred from short-period scattered PKP waves recorded at the global digital seismograph network, *J. Geophys. Res.*, *93*, 15,057–15,064.

Battaille, K., R. S. Wu, and S. M. Flatté (1990), Inhomogeneities near the core-mantle boundary evidence from scattered waves: A review, *Pure appl. geophys.*, *132*, 151–173.

Begheim, C., and J. Trampert (2003), Robust normal mode constraints on inner-core anisotropy from model space search, *Science*, *299*, 552–555.

Bergman, M. I. (1997), Measurements of elastic anisotropy due to solidification texturing and implications to the Earth's inner core, *Nature*, *339*, 60–63.

Bergman, M. I. (1998), Estimates of the Earth's inner core grain size, *Geophys. Res. Lett.*, *25*, 1593–1596.

Bergman, M. I. (1999), Experimental studies on the solidification of the Earth's inner core, *EOS Trans. AGU*.

Bergman, M. I. (2003), Solidification of Earth's core, in *Earth's Core: Dynamics, Structure, Rotation*, edited by V. Dehant, K. C. Creager, S. Karato, and S. Zatman, pp. 105–127, AGU monograph.

Bergman, M. I., D. M. Cole, and J. R. Jackson (2002), Preferred crystal orientations due to melt convection during solidification, *J. Geophys. Res.*, *107*, doi: 2001JB000601.

Berteussen, K. A., A. Christoffersson, E. S. Husebye, and A. Dahle (1975), Wave scattering theory in analysis of P-wave anomalies at NORSAR and LASA, *Geophys. J. R. Astron. Soc.*, *42*, 403–417.

Bevington, P. R. (1969), *Data Reduction and Error Analysis for the Physical Sciences*, McGraw-Hill, New York.

Bhattacharyya, J., P. M. Shearer, and G. Masters (1993), Inner core attenuation from short period $PKP(BC)$ versus $PKP(DF)$ waveforms, *Geophys. J. Int.*, *114*, 1–11.

Birch, F. (1964), Density and composition of the mantle and core, *J. Geophys. Res.*, *69*, 4377–4388.

Birch, F. (1972), The melting relations of iron , and temperatures in the Earth's core, *Geophys. J. R. Astron. Soc.*, *29*, 373–387.

Bloxham, J., and A. Jackson (1990), Lateral temperature variations at the core-mantle boundary deduced from the magnetic field, *Geophys. Res. Lett.*, *17*, 1997–2000.

Bolt, B. A. (1982), *Inside the Earth*, W. H. Freeman and Co, San Francisco.

Braña, L., and G. Helffrich (2004), A scattering region near the core-mantle boundary under the North Atlantic, *Geophys. J. Int.*, *158*, 625–636.

Braginsky, S. I. (1963), Structure of the F-layer and reasons for convection in the Earth's core, *Doklady Akad. Nauk SSSR*, *149*, 8–10.

Bréger, L., B. Romanowicz, and H. Tkalčić (1999), $PKP(BC-DF)$ travel time residuals and short scale heterogeneity in the deep Earth, *Geophys. Res. Lett.*, *26*, 3169–3172.

Brekhovskikh, L. M. (1960), *Waves in Layered Media*, Academic Press, London.

Brown, J. M., and R. G. McQueen (1986), Phase-transitions, gruneisen-parameter, and elasticity for shocked iron between 77 GPa and 400 GPa, *Geophys. J. R. Astron. Soc.*, *91*, 7485–7494.

Buffet, B. A., and H. R. Wenk (2001), Texturing of the Earth's inner core by Maxwell stresses, *Nature*, *413*, 60–63.

Bullen, K. E. (1946), A hypothesis on compressibility at pressures of the order of a million atmospheres, *Nature*, *157*, 405.

Cao, A., and B. Romanowicz (2004), Hemispherical transition of seismic attenuation at the top of the Earth's inner core, *Earth. Planet. Sci. Lett.*, *228*, 243–253.

Cao, A., and B. Romanowicz (2005), An observation of $PKJKP$; inferences on inner core shear properties, *Science*, *308*, 1453–1455.

Capon, J. (1969), High-resolution frequency-wavenumber spectrum analysis, *Proceedings of the IEEE*, *57*, 1408–1418.

Červený, V. (2001), *Seismic Ray Theory*, Cambridge University Press, Cambridge, New York.

Chernov, L. A. (1960), *Wave Propagation in a Random Medium*, McGraw-Hill, New York.

Cleary, J. R., and R. A. W. Haddon (1972), Seismic wave scattering near the core-mantle boundary: A new interpretation of precursors to $PKIKP$, *Nature*, *240*, 549–551.

Cormier, V. F. (1981), Short period PKP phases and the anelasticity mechanism of the inner core, *Phys. Earth. Planet. Inter.*, *24*, 291–301.

Cormier, V. F. (1982), The effect of attenuation on seismic body waves, *Bull. Seismol. Soc. Am.*, *72*, S169–S200.

Cormier, V. F., and X. Li (2002), Frequency-dependent seismic attenuation in the inner core. 2. A scattering and fabric interpretation, *J. Geophys. Res.*, *107(B12)*, 2362, doi:10.1029/2002JB1796.

Cormier, V. F., L. Xu, and G. L. Choy (1998), Seismic attenuation of the inner core: Viscoelastic or stratigraphic?, *Geophys. Res. Lett.*, *25*, 4019–4022.

Creager, K. C. (1992), Anisotropy of the inner core from differential travel times of the phases PKP and $PKIKP$, *Nature*, *356*, 309–314.

Creager, K. C. (1997), Inner core rotation rate from small-scale heterogeneity and time-varying travel times, *Science*, *278*, 1284–1288.

Creager, K. C. (1999), Large-scale variations in inner core anisotropy, *J. Geophys. Res.*, *104(B10)*, 23,127–23,139.

Creager, K. C. (2000), Inner core anisotropy and rotation, in *Earth's Deep Interior: Mineral, Physics and Tomography From the Atomic to the Global Scale*, edited by S. Karato, A. M. Forte, G. Liebermann, R. C. Masters, and L. Sixtrude, pp. 89–114, AGU monograph.

Dainty, A. M. (1990), Studies of coda using arrays and three-component processing, *Pure appl. geophys.*, *132*, 221–244.

Dainty, A. M., and C. A. Scultz (1995), Crustal reflections and the nature of regional *P* coda, *Bull. Seismol. Soc. Am.*, *85*, 851–858.

Dainty, A. M., and M. N. Toksöz (1981), Seismic codas on the Earth and the Moon: A comparison, *Phys. Earth. Planet. Inter.*, *26*, 250–260.

Dainty, A. M., and M. N. Toksöz (1990), Array analysis of seismic scattering, *Bull. Seismol. Soc. Am.*, *80*, 2242–2260.

Deuss, A., J. Woodhouse, H. Paulssen, and J. Trampert (1998), Observations of inner core shear waves, *EOS Trans. AGU*, *F79*.

Deuss, A., J. Woodhouse, H. Paulssen, and J. Trampert (2000), The observation of inner core shear waves, *Geophys. J. Int.*, *112*, 67–73.

Doornbos, D. J. (1974), The anelasticity of the inner core, *Geophys. J. R. Astron. Soc.*, *38*, 397–415.

Doornbos, D. J. (1976), Characteristics of lower mantle inhomogeneities from scattered waves, *Geophys. J. R. Astron. Soc.*, *44*, 447–470.

Doornbos, D. J. (1978), On seismic-wave scattering by a rough core-mantle boundary, *Geophys. J. R. Astron. Soc.*, *53*, 643–662.

Doornbos, D. J. (1983), Observable effects of the seismic absorption band in the Earth, *Geophys. J. R. Astron. Soc.*, *75*, 693–711.

Doornbos, D. J. (1988), Multiple scattering by topographic relief with application to the core-mantle boundary, *Geophysical Journal*, *92*, 465–478.

Doornbos, D. J., and E. S. Husebye (1972), Array analysis of PKP phases and their precursors, *Phys. Earth. Planet. Inter.*, *6*, 387–399.

Doornbos, D. J., and N. J. Vlaar (1973), Regions of seismic scattering near caustics: observations of $PKKP$ precursors, *Nature Phys. Sci.*, *243*, 58–61.

Douglas, A. (2002), Seismometer arrays–Their use in earthquake and test ban seismology, in *Handbook of Earthquake and Engineering Seismology*, edited by P. Jennings, H. Kanamori, and W. Lee, Academic Press, San Diego.

Douglas, D., D. Bowers, P. D. Marshall, J. B. Young, D. Porter, and N. J. Williams (1999), Putting nuclear-test monitoring to the test, *Nature*, *398*, 474–475.

Dziewonski, A. M., and D. L. Anderson (1981), Preliminary reference Earth model, *Phys. Earth. Planet. Inter.*, *25*, 297–356.

Dziewonski, A. M., and F. Gilbert (1971), Solidity of the inner core of the Earth inferred from normal mode observations, *Nature*, *234*, 465–466.

Earle, P. S., and P. M. Shearer (2001), Distribution of fine-scale mantle heterogeneity from observations of P_{diff} coda, *Bull. Seismol. Soc. Am.*, *91*, 1875–1881.

Fehler, M., P. Roberts, and T. Fairbanks (1988), A temporal change in coda waves attenuation observed during an eruption of Mount St. Helens, *J. Geophys. Res.*, *93*, 4367–4673.

Forte, A. M., and R. Peltier (1991), Viscous flow models of global geophysical observable, 1, Forward problems, *J. Geophys. Res.*, *92*, 20,131–20,159.

Frankel, A., and R. W. Clayton (1986), Finite difference simulations of seismic scattering: Implications for the propagation of short-period seismic waves in the crust and models of crustal heterogeneity, *J. Geophys. Res.*, *91*, 6465–6489.

Frankel, A., and L. Wennerberg (1987), Energy-flux model of seismic coda: Separation of scattering and intrinsic attenuation, *Bull. Seismol. Soc. Am.*, *85*, 1127–1143.

Frazer, L. N., and M. K. Sen (1985), Kirchhoff-Helmholtz reflection seismograms in a laterally inhomogeneous multi-layered elastic medium - I. Theory, *Geophys. J. R. Astron. Soc.*, *80*, 121–147.

Futterman, W. (1962), Dispersive body waves, *J. Geophys. Res.*, *67*, 5279–5291.

Ganapathy, R., and E. Anders (1976), Bulk compositions of he Moon, Earth estimated from meteorites, *Geochem. Cosmochim. Acta*, *5*, 1181–1206.

Gannarelli, C. M. S., D. Alfè, and M. J. Gillian (2003), The particle-in-cell model for ab initio thermodynamics: implications for the elastic anisotropy of the Earth's inner core, *Phys. Earth. Planet. Inter.*, *139*, 243–253.

Gannarelli, C. M. S., D. Alfè, and M. J. Gillian (2005), The axial ratio of hcp iron at the conditions of the Earth's inner core, *Phys. Earth. Planet. Inter.*, *152*, 67–77.

Garcia, R. (2002), Constraints on upper inner-core structure from waveform inversion of core phases, *Geophys. J. Int.*, *150*, 651–664.

Garcia, R., and A. Souriau (2000), Inner core anisotropy and heterogeneity level, *Geophys. Res. Lett.*, *27*, 3121–3124.

Gilbert, F., and L. Knopoff (1960), Seismic scattering from topographic irregularities, *J. Geophys. Res.*, *65*, 3437–3444.

Gubbins, D., and S. J. Gibbons (2004), Low Pacific secular variations, in *Timescales of the of the International Geomagnetic Field, Geophys. Monogr. Ser.*, edited by J. E. T. C. et al., pp. 279–286, AGU, Washington, D.C.

Haddon, R. A. W., and P. W. Buchen (1981), Use of Kirchhoff's formula for body wave calculations in the Earth, *Geophys. J. R. Astron. Soc.*, *67*, 587–598.

Haddon, R. A. W., and J. R. Cleary (1974), Evidence for scattering of seismic PKP waves near the mantle-core boundary, *Phys. Earth. Planet. Inter.*, *8*, 211–234.

Hedlin, M. A. H., and P. M. Shearer (2002), Probing mid-mantle heterogeneity using PKP coda waves, *Phys. Earth. Planet. Inter.*, *130*, 195–208.

Hedlin, M. A. H., P. M. Shearer, and P. S. Earle (1997), Seismic evidence for small-scale heterogeneity throughout the Earth's mantle, *Nature*, *387*, 145–150.

Helmberger, D. (1983), Theory and application of synthetic seismograms, in *Earthquakes: Observation, Theory and Interpretation, International School of Physics "Enrico Fermi" Course LXXXV*, edited by H. Kanamori, North-Holland, New York.

Herrmann, R. B. (1980), Q estimates using the coda of local earthquakes, *Bull. Seismol. Soc. Am.*, *70*, 447–468.

Husebye, E. S., and B. O. Ruud (1989), Array seismology–Past, present and future developments, in *Observatory Seismology*, edited by J. J. Litehiser, Univ. of California Press, Berkeley.

Ishii, M., A. M. Dziewonski, J. Tromp, and G. Ekström (2002a), Joint inversion of normal mode and body wave data for inner core anisotropy. 2. Possible complexities, *J. Geophys. Res.*, *107(B12)*, 2380, doi:10.1029/2001JB000713.

Ishii, M., J. Tromp, A. M. Dziewonski, and G. Ekström (2002b), Joint inversion of normal mode and body wave data for inner core anisotropy. 1. Laterally homogeneous media, *J. Geophys. Res.*, *107(B12)*, 2379, doi:10.1029/2001JB000712.

Jacobs, J. A. (1953), The Earth's inner core, *Nature*, *172*, 297–298.

Jeanloz, R. (1979), Properties of iron at high pressures and the state of the core, *J. Geophys. Res.*, *84*, 6059–6069.

Jeanloz, R., and H. R. Wenk (1988), Convection and anisotropy of the inner core, *Geophys. Res. Lett.*, *15*, 72–75.

Jemberie, A. L., and C. A. Langston (2005), Site amplification, scattering, and intrinsic attenuation in the Mississippi embayment from coda waves, *Bull. Seismol. Soc. Am.*, *95*, 1716–1730, doi:10.1785/0120040203.

Jephcoat, A., and P. Olson (1987), Is the inner core of the Earth pure iron?, *Nature*, *325*, 332– 335.

Jin, A., and K. Aki (1988), Spatial and temporal correlation between coda Q and seismicity in China, *Bull. Seismol. Soc. Am.*, *78*, 741–769.

Johnson, C. L., and C. G. Constable (1998), Persistently anomalous Pacific geomagnetic fields, *Geophys. Res. Lett.*, *25*, 1011–1014.

Julian, B. R., D. Davies, and R. Shepard (1972), $PKJKP$, *Nature*, *235*, 317–318.

Kampfmann, W., and G. Müller (1989), PcP amplitude calculations for a core-mantle boundary with topography, *Geophys. Res. Lett.*, *16*, 653–656.

Kanasewich, E. R., R. M. Ellis, C. H. Chapman, and P. Gutowski (1973), Seismic array evidence of a core boundary source for the Hawaiian linear volcanic chain, *J. Geophys. Res.*, *78*, 1361–1371.

Kaneshima, S. (1996), Mapping heterogeneity of the uppermost inner core using two pairs of core phases, *Geophys. Res. Lett.*, *23*, 3075–3078.

Kaneshima, S., and G. Helffrich (1998), Detection of lower mantle scatterers northeast of the Mariana subduction zone using short-period array data, *J. Geophys. Res.*, *103*, 4825–4838.

Karato, S. I. (1999), Seismic anisotropy of the Earth's inner core resulting from flow induced by Maxwell stresses, *Nature*, *403*, 871–873.

Kennett, B. L. N. (1972), Seismic wave scattering by obstacles on interfaces, *Geophys. J. R. Astron. Soc.*, *28*, 249–266.

Kennett, B. L. N. (2001), *The Seismic Wave Field. Volume I: Introduction and Theoretical Development*, Cambridge University Press, Cambridge, New York.

King, D. W., R. A. W. Haddon, and J. R. Cleary (1974), Array analysis of precursors to $PKIKP$ in the distance range 128° to 142°, *Geophys. J. R. Astron. Soc.*, *37*, 157–173.

Knopoff, L., and J. A. Hudson (1964), Scattering of elastic waves by small inhomogeneities, *J. Acoust. Soc. Am.*, *36*, 338–343.

Knopoff, L., and J. A. Hudson (1967), Frequency dependence of amplitudes of scattered elastic waves, *J. Acoust. Soc. Am.*, *42*, 18–20.

Koper, K. D., and M. Dombrovskaya (2005), Seismic properties of the inner core boundary from $PKiKP/P$ amplitude ratios, *Earth. Planet. Sci. Lett.*, *237*, 680–694.

Koper, K. D., and M. L. Pyle (2004), Observations of $PKiKP/PcP$ amplitude ratios and implications for Earth structure at the boundaries of the liquid core, *J. Geophys. Res.*, *107(B12)*, 2361, doi:10.1029/2002JB1795.

Koper, K. D., M. L. Pyle, and J. M. Franks (2003), Constraints on aspherical core structure from $PKiKP - PcP$ differential travel times, *J. Geophys. Res.*, *107(B12)*, 2368, doi:10.1029/2002JB1995.

Koper, K. D., J. M. Franks, and M. Dombrovskaya (2004), Evidence for small-scale heterogeneities in the Earth's inner core from a global study of $PKiKP$ coda waves, *Earth. Planet. Sci. Lett.*, *228*, 227–241.

Krasnoshcenkov, D. N., P. B. Kaazik, and V. M. Ovtchinnikov (2005), Seismological evidence for mosaic structure of the surface of the Earth's inner core, *Nature*, *436*, 483–487, doi:10.1038/nature03613.

Krüger, F., M. Baumann, D. Scherbaum, and M. Weber (2001), Mid-mantle scatterers near the Mariana slab detected with a double array method, *Geophys. Res. Lett.*, *28*, 667–670.

Lacombe, C., M. Campillo, A. Paul, and L. Margerin (2003), Separation of intrinsic absorption and scattering attenuation from *Lg* coda decay in central France using acoustic radiative transfer theory, *Geophys. J. Int.*, *154*, 417–425.

Lee, W., H. Sato, and H. Lee (2003), Estimation of *S*-wave scattering coefficient in the mantle from envelope characteristics before and after *ScS* arrival, *Geophys. Res. Lett.*, *30*, doi:10.1029/2003GL018413.

Lehmann, I. (1936), P', *Bureau Central Seismologique International*, *A14*, 3–31.

Leyton, F., and K. D. Koper (2004), Quantification of inner core heterogeneities using *PKiKP* coda, *Trans. AGU Fall Meeting*.

Leyton, F., K. D. Koper, L. Zhu, and M. Dombrovskaya (2005), On the lack of seismic discontinuities in the inner core, *Geophys. J. Int.*, *162*, doi:10.1111/j.1365-146X.2005.02480.x.

Li, X., and V. F. Cormier (2002), Frequency-dependent seismic attenuation in the inner core. 1. A viscoelastic interpretation, *J. Geophys. Res.*, *107(B12)*, 2361, doi: 10.1029/2002JB001795.

Ligorria, J. P., and C. J. Ammon (1999), Iterative deconvolution and receiver-function estimation, *Bull. Seismol. Soc. Am.*, *89*, 1395–1400.

Lin, J. F., D. L. Heinz, A. J. Campbell, J. M. Devine, and G. Shen (2002), Iron-silicon alloy in the Earth's core?, *Science*, *295*, 313.

Lister, J. R., and B. A. Buffett (1995), The strength and efficiency of thermal and compositional convection of the Earth's core, *Phys. Earth. Planet. Inter.*, *91*, 17–30.

Mao, H. K., J. F. Shu, and G. Y. Shen (1998), Elasticity and rheology of iron above 220 GPa and the nature of the Earth's inner core, *Nature*, *396*, 741–743.

Margerin, L., and G. Nolet (2003a), Multiple scattering of high-frequency seismic waves in the deep Earth: Modeling and numerical examples, *J. Geophys. Res.*, *108*, doi:10.1029/2002JB001794.

Margerin, L., and G. Nolet (2003b), Multiple scattering of high-frequency seismic waves in the deep Earth: PKP precursor analysis and inversion for mantle granularity, *J. Geophys. Res.*, *108*, doi:10.1029/2003JB002455.

Master, T. G., and P. M. Shearer (1990), Summary of seismological constraints on the structure of the Earth's core, *Nature*, *396*, 741–743.

Matsumoto, S., and A. Hasegawa (1989), Two-dimensional coda Q structure beneath Tohoku, NE Japan, *Geophys. J. Int.*, *99*, 101–108.

McSweeney, T. J., K. C. Creager, and R. T. Merril (1997), Depth extent of inner core seismic anisotropy and implications for geomagnetism, *Phys. Earth. Planet. Inter.*, *101*, 131–156.

Menke, W. (1989), *Geophysical Data Analysis: Discrete Inverse Theory*, Academic Press, International Geophysical series, New York.

Merrill, R. T., M. W. McElhinny, and P. L. McFadden (1998), *The Magnetic Field of the Earth (Paleomagnetism, the core, and the deep mantle)*, Academic Press, San Diego, California.

Mitchell, B. J. (1980), Frequency dependence of shear wave attenuation in North America, *J. Geophys. Res.*, *85*, 5212–5218.

Mitchell, B. J. (1995), Anelastic structure and evolution of the continental crust and upper mantle from seismic wave attenuation, *Rev. Geophys.*, *33*, 441–462.

Morelli, A., A. M. Dziewonski, and J. H. Woodhouse (1986), Anisotropy of the inner core inferred from $PKIKP$ travel times, *Geophys. Res. Lett.*, *13*, 1545–1548.

Morozov, I. B., and S. B. Smithson (2000), Coda of long-range arrivals from nuclear explosions, *Bull. Seismol. Soc. Am.*, *90*, 929–939.

Niazi, M., and L. R. Johnson (1992), Q in the inner core, *Phys. Earth. Planet. Inter.*, *74*, 55–62.

Nishigami, K. (1997), Spatial distribution of coda scatterers in the crust around two active volcanoes and one active fault system in central Japan: Inversion analysis of coda envelope, *Phys. Earth. Planet. Inter.*, *104*, 75–89.

Niu, F., and L. Wen (2001), Hemispherical variations in the seismic velocity at the top of the Earth's inner core, *Nature*, *410*, 1081–1084.

Niu, F., and L. Wen (2002), Seismic anisotropy in the top 400 km of the inner core beneath the "eastern" hemisphere, *Geophys. Res. Lett.*, *29*, doi: 10.1029/2001GL014118.

Ohori, M., A. Nobata, and K. Wakamatsu (2002), A comparison of ESAC and FK methods of estimating phase velocity using arbitrarily shaped microtremor arrays, *Bull. Seismol. Soc. Am.*, *96*, 2323–2332.

Okal, E. A., and Y. Cansi (1998), Detection of $PKJKP$ at intermediate periods by progressive multi-channel correlation, *Earth. Planet. Sci. Lett.*, *164*, 23–30.

Oldham, R. D. (1906), The constitution of the interior of the Earth, as revealed by earthquakes, *Quaterly Journal, Geological Society*, *62*, 456–475.

Oreshin, S. I., and L. P. Vinnik (2004), Heterogeneity and anisotropy of seismic attenuation in the inner core, *Geophys. Res. Lett.*, *31*, doi:10.1029/2003GL018591.

Ouzounis, A., and K. C. Creager (2001), Isotropy overlaying anisotropy at the top of the inner core, *Geophys. Res. Lett.*, *28*, 4331–4334.

Poupinet, G., and B. L. N. Kennett (2004), On the observation of high frequency $PKiKP$ and its coda in Australia, *Phys. Earth. Planet. Inter.*, *146*, 497–511.

Poupinet, G., R. Pillet, and A. Souriau (1983), Possible heterogeneity of the Earth's core deduced from $PKIKP$ travel times, *Nature*, *305*, 204–206.

Pourier, J. P. (1994), Light elements in the Earth's outer core - a critical review, *Phys. Earth. Planet. Inter.*, *85*, 319–337.

Qamar, A., and A. Eisenberg (1974), The damping of core waves, *J. Geophys. Res.*, *79*, 758–765.

Rautian, T. G., and V. G. Khalturin (1978), The use of the coda for the determination of the earthquake source spectrum, *Bull. Seismol. Soc. Am.*, *68*, 923–948.

Revenaugh, J. (1995), The contribution of topographic scattering to teleseismic coda in Southern California, *Geophys. Res. Lett.*, *22*, 543–546.

Richards, P. G. (1972), Seismic waves reflected from velocity gradients anomalies within the Earth's upper mantle, *Zeitschrift für Geophysik*, *38*, 517–527.

Richards, P. G., and W. Menke (1983), The apparent attenuation of a scattering medium, *Bull. Seismol. Soc. Am.*, *73*, 1005–1021.

Romanowicz, B. (2003), Global mantle tomography: Progress status in the past 10 years, *Annu. Rev. Earth Planet. Sci.*, *31*, 303–328, doi: 10.1146/annurev.earth.31.091602.113555.

Rondenay, S., and K. M. Fischer (2003), Constraints on localized core-mantle boundary structure from multichannel, broadband *SKS* coda analysis, *J. Geophys. Res.*, *108*, doi:10.1029/2003JB002518.

Rost, S., and J. Reveanugh (2001), Seismic detection of rigid zones at the top of the inner core, *Science*, *294*, 1911–1914.

Rost, S., and C. Thomas (2002), Array seismology: Methods and applications, *Rev. Geophys.*, *40*, 1008, doi:10.1029/2000RG000100.

Rost, S., E. J. Garnero, Q. Williams, and M. Manga (2005), Seismological constraints on a possible plume root at the core-mantle boundary, *Nature*, *435*, 666–669, doi: 10.1038/nature03620.

Sambridge, M. (1999a), Geophysical inversion with a neighbourhood algorithm - I. Searching a parameter space, *Geophys. J. Int.*, *138*, 479–494.

Sambridge, M. (1999b), Geophysical inversion with a neighbourhood algorithm - II. Appraising the ensemble, *Geophys. J. Int.*, *138*, 727–746.

Sambridge, M. (2001), Finding acceptable models in nonlinear inverse problems using a neighbourhood algorithm, *Inverse Problems*, *17*, 387–403.

Sato, H., and M. C. Fehler (1998), *Seismic Wave Propagation and Scattering in the Heterogeneous Earth*, AIP Press, New York.

Scherbaum, F., D. Gillard, and N. Diechmann (1991), Slowness power spectrum analysis of the coda composition of two micoearthquakes clusters in northern Switzerland, *Phys. Earth. Planet. Inter.*, *67*, 137–161.

Schimmel, M., and H. Paulssen (1997), Noise reduction and detection of weak, coherent signal through phase-weighted stacks, *Geophys. J. Int.*, *130*, 497–505.

Scott, P., and D. V. Helmberger (1983), Applications of the Kirchhoff-Helmholtz integral to problems in seismology, *Geophys. J. R. Astron. Soc.*, *72*, 237–254.

Secco, R. A. (1995), Viscosity of the outer core, in *A Handbook of Physical Constants: Mineral Physics and Crystallography*, edited by T. J. Ahrens, AGU Reference Shelf 2.

Shearer, P. M. (1994), Constraints on inner core anisotropy from $PKP(DF)$ differential travel times, *J. Geophys. Res.*, *99*, 19,647–19,659.

Shearer, P. M., and P. S. Earle (2005), The global short-period wavefield modelled with a Monte Carlo seismic phonon method, *Geophys. J. Int.*, *158*, 1103–1117, doi:10.1111/j.1365-246X.2004.02378.x.

Shearer, P. M., M. A. H. Hedlin, and P. S. Earle (1998), PKP and $PKKP$ precursor observations: Implications for the small-scale structure of the deep mantle and core, in *The Core-Mantle Boundary Region*, edited by M. Gurnis, M. E. Wysession, E. Knittle, and B. A. Buffet, pp. 37–56, AGU monograph.

Singh, S., and R. B. Herrmann (1983), Regionalization of crustal coda Q in the continental United States, *J. Geophys. Res.*, *88*, 527–538.

Singh, S. C., M. A. J. Taylor, and J. P. Montagner (2000), On the presence of liquid in the Earth's inner core, *Science*, *287*, 2471–2474.

Snieder, R., A. Grêt, H. Douma, and J. Scales (2002), Coda wave interferometry for estimating nonlinear behavior in seismic velocity, *Science*, *295*, 2253–2255.

Song, X. D. (1996), Anisotropy in central part of inner core, *J. Geophys. Res.*, *101*, 16,089–16,097.

Song, X. D. (2000), Joint inversion for inner core rotation, inner core anisotropy, and mantle heterogeneity, *J. Geophys. Res.*, *105*, 7931–7943.

Song, X. D. (2003), 3D structure and differential rotation of the inner core, in *Earth's Core: Dynamics, Structure, Rotation*, edited by V. Dehant, K. C. Creager, S. Karato, and S. Zatman, pp. 45–64, AGU monograph.

Song, X. D., and D. V. Helmberger (1993), Anisotropy of Earth's inner core, *Geophys. Res. Lett.*, *20*, 2591–2594.

Song, X. D., and D. V. Helmberger (1995), Depth dependence anisotropy of Earth's inner core, *J. Geophys. Res.*, *100*, 9805–9816.

Song, X. D., and D. V. Helmberger (1998), Seismic evidence of an inner core transition zone, *Science*, *282*, 924–924.

Song, X. D., and X. X. Xu (2002), Inner core transition zone and anomalous $PKP(DF)$ waveforms from polar paths, *Geophys. Res. Lett.*, *29*, doi: 10.1029/2001GL013822.

Souriau, A., and P. Roudil (1995), Attenuation in the uppermost inner core from broad-band GEOSCOPE PKP data, *Geophys. J. Int.*, *123*, 572–587.

Souriau, A., and M. Souriau (1989), Ellipticity and density at the inner core boundary from subcrititcal $PKiKP$ and PcP data, *Geophys. J. Int.*, *98*, 39–54.

Stacey, F. D., and C. H. B. Stacey (1999), Gravitational energy of the core evolution: implications for thermal history and geodynamo power, *Phys. Earth. Planet. Inter.*, *110*, 83–93.

Steile-Neumann, G., L. Stixrude, and R. E. Cohen (2003), Physical properties of iron in the inner core, in *Earth's Core: Dynamics, Structure, Rotation*, edited by V. Dehant, K. C. Creager, S. Karato, and S. Zatman, pp. 137–162, AGU monograph.

Steinle-Neumann, G., L. Stixrude, R. E. Cohen, and O. Gulseren (2001), Elasticity of iron at the temperature of the Earth's inner core, *Nature*, *413*, 57–60.

Stixrude, L., and R. E. Cohen (1995), High-pressure elasticity of iron and anisotropy of Earth's inner core, *Science*, *267*, 1972–1975.

Stroujkova, A., and V. F. Cormier (2004), Regional variations in the uppermost 100 km of the Earth's inner core, *J. Geophys. Res.*, *109(B10307)*, doi: 10.1029/2004JB002976.

Su, W., and A. M. Dziewonski (1995), Inner core anisotropy in three dimensions, *J. Geophys. Res.*, *100(B7)*, 9831–9852.

Sumita, I., and P. Olson (1999), A laboratory model for convection in the Earth's core driven by a thermally heterogeneous mantle, *Science*, *286*, 1547–1549.

Sumita, I., and S. Yoshida (2003), Thermal interactions between the mantle, outer an inner core, and the resulting structural evolution of the core, in *Earth's Core: Dynamics, Structure, Rotation*, edited by V. Dehant, K. C. Creager, S. Karato, and S. Zatman, pp. 213–232, AGU monograph.

Sumita, I., S. Yoshida, M. Kumazawa, and Y. Hamano (1996), A model for sedimentary compaction of a viscous medium and its application to the inner-core growth, *Geophys. J. Int.*, *124*, 502–524.

Tanaka, S. (2005), Characteristics of PKP-$Cdiff$ coda revealed by small-aperture seismic arrays: Implications for the study of the inner core boundary, *Phys. Earth. Planet. Inter.*, *153*, 49–60.

Tanaka, S., and H. Hamaguchi (1997), Degree one heterogeneity and hemispherical variation of anisotropy in the inner core from $PKP(BC) - PKP(DF)$ times, *J. Geophys. Res.*, *102(B2)*, 2925–2938.

Telford, W. M., L. P. Geldart, R. E. Sheriff, and D. A. Keys (1976), *Applied Geophysics*, Cambridge University Press, Cambridge.

Tromp, J. (1993), Support of anisotropy of the Earth's inner core from free oscillations, *Nature*, *366*, 678–681.

Tromp, J. (2001), Inner-core anisotropy and rotation, *Annu. Rev. Earth Planet.*, *29*, 47–69.

Tsujiura, M. (1978), Spectral analysis of the coda waves from local earthquakes, *Bul. Earthq. Inst. Univ. Tokyo*, *53*, 1–48.

Van Orman, J. A. (2004), On the viscosity and creep mechanism on the Earth's inner core, *Geophys. Res. Lett.*, *31*, doi:10.1029/2004GL021209.

Verhoogen, J. (1961), Heat balance of the Earth's core, *Geophys. J. R. Astron. Soc.*, *4*, 276–281.

Vidale, J. E., and P. S. Earle (2000), Fine-scale heterogeneity in the Earth's inner core, *Nature*, *404*, 273–275.

Vidale, J. E., and P. S. Earle (2005), Evidence for inner-core rotation from possible changes with time in the PKP coda, *Geophys. Res. Lett.*, *32*, doi: 10.1029/2004GL021240.

Vidale, J. E., D. A. Dodge, and P. S. Earle (2000), Slow differential rotation of the Earth's inner core indicated by temporal changes in scattering, *Nature*, *405*, 445–448.

Vinnik, L., B. Romanowicz, and L. Breger (1994), Anisotropy in the center of the inner core, *Geophys. Res. Lett.*, *21*, 1671–1674.

Vocadlo, L., J. Brodholt, D. Alfè, G. D. Price, and M. J. Gillian (1999), The structure of iron under the conditions of the Earth's inner core, *Geophys. Res. Lett.*, *26*, 1231–1234.

Walker, A. D., and G. E. Backus (1996), On the difference between the average values of B_r^2 in the Atlantic and the Pacific hemispheres, *Geophys. Res. Lett.*, *23*, 1965–1968.

Wasson, J. (1985), *Meteorites: Their Record of Early Solar-System History*, W. H. Freeman and Co., New York.

Weber, M., J. P. Davis, C. Thomas, F. Krüger, F. Scherbaum, J. Schlittenhardt, and M. Körnig (1996), The structure of the lowermost mantle as determined from using seismic arrays, in *Seismic Modeling of Earth Structure*, edited by E. Boschi, G. Ekström, and A. Morelli, Editrice Compositori.

Wen, L., and D. V. Helmberger (1998a), Ultra-low velocity zones near the core-mantle boundary from broadband PKP precursors, *Science*, *279*, 1701–1703.

Wen, L., and D. V. Helmberger (1998b), A two-dimensional $P - SV$ hybrid method and its application to modeling localized structures near the core-mantle boundary, *J. Geophys. Res.*, *103*, 17,901–17,918.

Wen, L., and F. Niu (2002), Seismic velocity and attenuation structures in the top of the Earth's inner core, *J. Geophys. Res.*, *107*, doi:10.1029/2001JB000170.

Woodhouse, J. H., D. Giardini, and X. D. Li (1986), Evidence for inner core anisotropy from free oscillations, *Geophys. Res. Lett.*, *13*, 1549–1552.

Wu, R. S. (1985), Multiple scattering and energy transfer of seismic waves - separation of the intrinsic absorption and scattering attenuation in Northeastern Venezuela (Southeastern Caribbean) using coda waves, *Geophys. J. R. Astron. Soc.*, *82*, 57–80.

Wu, R. S., and K. Aki (1985a), Elastic wave scattering by a random medium and the small-scale inhomogeneities in the lithosphere, *J. Geophys. Res.*, *90*, 10,261–10,273.

Wu, R. S., and K. Aki (1985b), Scattering characteristics of elastic waves by an elastic heterogeneity, *Geophysics*, *50*, 582–595.

Yoo, C. S., J. Akella, A. J. Campbell, H. K. Mao, and R. J. Menley (1995), Phase diagram of iron in in situ X-ray diffraction: implications for Earth's core, *Science*, *270*, 1473–1475.

Yoshida, S., I. Sumita, and M. Kumazawa (1996), Growth model of the inner core coupled with the outer core dynamics and the resulting elastic anisotropy, *J. Geophys. Res.*, *101*, 28,085–28,103.

Yoshizawa, K., and B. L. N. Kennett (2002), Non-linear waveform inversion for surface waves with a neighbourhood algorithm - application to multimode dispersion measurements, *Geophys. J. Int.*, *149*, 118–133.

Yu, W., L. Wen, and F. Niu (2005), Seismic velocity structure in the Earth's outer core, *J. Geophys. Res.*, *110*, B02,302, doi:10.1029/2003JB002928.

Zhang, J., X. Song, Y. Li, P. G. Richards, X. Sun, and F. Waldhauser (2005), Inner core differential motion confirmed by earthquake waveform doublets, *Science*, *309*, 1357–1360.

Vita Autoris

Felipe Orlando Leyton Flórez was born in Valdivia, in the beautiful southern part of Chile. At a young age, his family moved north, to Talca, where they lived for a few years. Later, his parents, seeking a better education for their children, decided to move to Santiago, Chile's capital.

Felipe attended school at Saint Gabriel's English School, where he graduated from high school. Then, he decided to pursue a degree in Civil Engineering, in the prestigious Universidad de Chile. Upon finishing his bachelor degree, and stimulated to learn about the secrets of earthquakes, Felipe decided to get a Masters in Sciences, mention Geophysics, in the same University. He graduated with maximum honors and, after a long decision, decided to follow his career as a seismologist and joined Saint Louis University's PhD. program in 2002. Felipe expects to receive the Doctor of Philosophy in Geophysics in May 2006.

In 2004, Felipe married Carolina after 6 years of dating and hopes to build a family and grow old back in Chile.